Modelling of CHF and Post-CHF Heat Transfer for Trans-critical Transients

Zur Erlangung des akademischen Grades einer
DOKTORIN DER INGENIEURWISSENSCHAFTEN (Dr.-Ing.)

von der KIT-Fakultät für Maschinenbau des
Karlsruher Instituts für Technologie (KIT)
angenommene

DISSERTATION

von

B.Sc. Meiqi Song

Tag der mündlichen Prüfung: 26. Oktober 2021

Hauptreferent: Prof. Dr.-Ing. Xu Cheng

Korreferent: Prof. Xiaojing Liu

Declaration

I declare that I have developed and written the enclosed thesis completely by myself, and have not used sources or means without declaration in the text.

Shanghai, China 05.08.2021

(Meiqi Song)

Acknowledgements

I would first like to express my sincere gratitude to my supervisor Prof. Xu Cheng, for his academic support and care for students beyond obligations. I would like to thank him for providing the innovative and effective research environment. Without his guidance and invaluable advice, it is impossible to finish this dissertation.

I am deeply grateful to Prof. Xiaojing Liu who is my second supervisor. I would like to appreciate his great support, kind review, and insightful comments.

My current and former colleagues in IATF, I would like to thank them for their company and help. I am thankful to Dr. Aurelian Florin Badea and Dr. Hong Xu, for discussing the use of ATHLET code. I would like to thank Mr. Moritz Schenk, Mr. Ludwig Köckert, Dr. Dali Yu, Dr. Meng Zhao, Dr. Fangnian Wang, Dr. Xi Wang, Dr. Florian Feuerstein, Mr. Stelios Michaelides, Dr. Ivan Otic, Mr. Zhongkai Mei, and etc., for their fruitful academic discussion and kind help in daily life. I would be grateful to our technical staff Mr. Denis Klingel, and our secretaries, Ms. Isolde Stamm and Ms. Marina Djordjevic.

I would also like to thank GRS for providing ATHLET code and related documents.

My parents and my younger brother, I would like to give them my special thanks for their encouragement and patience.

In such a special pandemic situation, I wish all my dear colleagues and friends good health. I look forward to the day when we could take off masks and get reunion.

Shanghai, China, 27.07.2021

Meiqi Song

Abstract

Supercritical power cycle systems are widely applied to utilize various energy sources, e.g., nuclear energy, solar energy, geothermal energy, and bioenergy. Designed to be working at supercritical conditions, the occurrence of two-phase boiling crisis is eliminated since supercritical fluids are single-phase. However, during some transient procedures such as startup, shutdown, and accident conditions, the supercritical system may experience trans-critical transient and work at high-pressure subcritical conditions. Since critical heat flux (CHF) reduces with the increase of pressure at the high-pressure region, the occurrence of boiling crisis becomes much easier and could lead to burnout of the heated wall. Therefore, the heat transfer analysis of the trans-critical transient is crucial to supercritical power cycles. Though some system thermal-hydraulic (STH) codes have been extended to the supercritical condition, reliable heat transfer models for the high-pressure subcritical region are still required since these STH codes are only validated for conventional light water reactors, i.e., Pressurized Water Reactor (PWR) and Boiling Water Reactor (BWR), with the pressure normally lower than 15.5 MPa. Thus, the present work mainly aims to update CHF model and post-CHF heat transfer model for the high-pressure subcritical condition (with reduced pressure above 0.7, $P/P_c > 0.7$).

A high-pressure CHF databank has been established with CHF experiments in uniformly heated round tubes. Previous CHF models in open literatures are assessed against the databank but could not provide satisfying prediction accuracy. Hence, a new dimensionless CHF correlation is proposed based on high-pressure water CHF test data. The new CHF correlation is validated by the high-pressure CHF experiments for R12 and CO_2, respectively, and shows a better prediction than previous methods.

Concerning post-CHF heat transfer, as high-pressure post-DNB experiment is unavailable so far, the present work established only a post-dryout (PDO) heat transfer databank. Accordingly, previous heat transfer correlations are compared with high-pressure water PDO experiments and show insufficient predictive capability. A new PDO heat transfer correlation is developed and gives good prediction accuracy to high-pressure water PDO test data. Additionally, the predictive capability of the new PDO heat transfer correlation is confirmed by test data obtained in high-pressure CO_2 experiments, R134a experiments, and water experiments with non-uniform heat flux.

The new CHF correlation and new PDO heat transfer correlation are implemented to modify the STH code ATHLET-SC. Trans-critical heat transfer experiments of a 4-rod bundle are simulated by the modified ATHLET-SC. Compared to the original code, the modified ATHLET-SC code gives better agreement with experimental results. During the depressurization trans-critical process, the sudden wall heat-up as the pressure crosses the critical point and the rise of the wall temperature with the decrease of pressure in subcritical condition is well predicted by the modified ATHLET-SC code.

In summary, to guarantee the prediction of trans-critical transients, a new CHF prediction model and a new PDO heat transfer model have been developed and used to upgrade the STH code ATHLET-SC, which makes up the deficiency of high-pressure heat transfer models and is of great significance for safety analysis of supercritical power cycles.

Kurzfassung

Kreisläufe mit überkritischem Wasser finden in vielen verschiedenen Kraftwerken Anwendung, zum Bsp. Kohlekraftwerke, Solarenergie, Geothermie oder Bioenergie. Auch für die Nutzung der Kernenergie sollen in naher Zukunft überkritische Kreisläufe verwendet werden. Diese Anlagen wurden für überkritische Bedingen entwickelt, aus diesem Grund ist das Auftreten einer zweiphasigen Siedekrise nicht vorgesehen - überkritische Fluide weisen keinen Phasenübergang auf. Jedoch könnten bei einigen Betriebszuständen, wie Anfahren oder Abschalten der Anlage, sowie unter Unfallbedingungen transkritische Zustände auftreten, d.h. die Anlage müsste bei hohem Druck und unterkritischen Bedingungen arbeiten. Da die kritische Heizflächenbelastung (Critical Heat Flux (CHF)) mit zunehmendem Druck abnimmt, wird ein Auftreten einer Siedekrise wahrscheinlicher und es kann zu einem Burnout der beheizenden Wand führen. Daher ist die Analyse des Wärmeübergangs im transkritischen Bereich in überkritischen Anlagen von entscheidender Bedeutung. Obwohl einige thermohydraulische (STH) Systemcodes dahingehend erweitert wurden, dass sie überkritische Bedingungen berücksichtigen können, werden weiterhin zuverlässige Wärmeübergangsmodelle im unterkritischen Hochdruck-Bereich benötigt. Die bestehenden STH-Codes sind nur für konventionelle Leichtwasserraktoren, d.h. für Druck- und Siedewasserreaktoren, validiert, deren Betriebsdruck normalerweise unter 15,5 MPa liegt. Daher zielt die vorliegende Arbeit hauptsächlich darauf ab, das CHF-Modell und das Wärmübergangsmodell nach dem CHF für diesen Bereich zu aktualisieren. Das unterkritische Druckverhältnis soll dabei höher als $P/P_c = 0{,}7$ sein.

Eine Hochdruck-CHF-Datenbank wurde mit gleichmäßig beheizten Rundrohr-CHF-Experimenten erstellt. Frühere CHF-Modelle aus der Literatur werden anhand dieser Datenbank bewertet, konnten jedoch keine zufriedenstellende Vorhersagegenauigkeit liefern. Daher wird in dieser Arbeit eine neue dimensionslose CHF-Korrelation basierend auf Hochdruckwasser-CHF-Testdaten vorgeschlagen Die neue CHF-Korrelation wird durch Hochdruck-CHF-Experimente für R12 sowie CO2 validiert und zeigt eine bessere Vorhersage als bisherige Methoden.

Für Post-CHF Bedingungen wurde in der hier vorliegenden Arbeit nur eine Post-Dryout-(PDO)-Wärmeübertragungsdatenbank erstellt, da bei hohen Drücken keine sogenannte Departure of Nucleate Boilin (DNB)-Versuche vorliegen. Dementsprechend werden vorhandene Wärmeübergangskorrelationen mit den Hochdruckwasser-PDO-Experimenten verglichen, diese Korrelationen zeigen jedoch eine nur unzureichende Vorhersagefähigkeit. Die in dieser Arbeit neu entwickelte PDO-Wärmeübertragungskorrelation weist dagegen eine gute Vorhersagegenauigkeit für die PDO-Testdaten für Hochdruckwasser auf. Zusätzlich wird die Vorhersagefähigkeit der neuen PDO-Wärmeübertragungskorrelation durch Testdaten bestätigt, die durch Hochdruck-CO2-Experimente, R134A-Experimente und Wasser-Experimente mit

ungleichmäßig verteilter Wärmestromdichte erhalten wurden.

Die neue CHF-Korrelation und die neue PDO-Wärmeübertragungskorrelation wurden in den modifizierten STH-Code ATHLET-SC implementiert. Mit diesem modifizierten Programm wurden transkritische Wärmeübertragungsexperimente eines Vier-Stab-Bündels simuliert. Im Vergleich zum Originalcode stimmt der modifizierte ATHLET-SC-Code besser mit experimentellen Ergebnissen überein. Die plötzliche Wanderwärmung beim Unterschreiten des kritischen Punktes und der Anstieg der Wandtemperatur bei weiterem Druckabfall im unterkritischen Zustand werden durch den modifizierten ATHLET-SC-Code gut vorhergesagt.

Zusammenfassend wurde ein neues CHF-Vorhersagemodel und ein neues PDO Wärmeübertragungsmodell entwickelt und in den STH-Code ATHLET-SC implementiert, um sicherzugehen, dass die transkritischen Transienten vorhergesagt werden können. Damit wird die Lücke bei Hochdruck-Wärmeübertragungsmodellen geschlossen. Dies ist von großer Bedeutung für die Sicherheitsanalyse von überkritischen Kreisläufen.

Contents

List of Figures

List of Tables

Nomenclature

General

Symbol	Description
Bo	Boiling number, -
c_p	Specific heat, J/(kg·℃)
C_{D}	Drag force coefficient, -
D_{h}	Tube diameter, m
f	Friction factor, -
Fr	Froude number, -
g	Gravitational accelaration, m/s^2
G	Mass flux, kg/(m^2·s)
G_{LF}	Liquid film mass flux, kg/(m^2·s)
h	Heat transfer coefficient, W/(m^2·℃)
H	Enthalpy, J/kg
H_{LS}	Enthalpy of saturated liquid, J/kg
H_{VL}	Evaporation heat, J/kg
$H_{\mathrm{V,a}}$	Calcualted actucal vapor enthalpy, J/kg
$H_{\mathrm{V,e}}$	Equilibrium vapor enthalpy, J/kg
L	Length, m
ME	Mean value, -
N	Number of data point, -
Nu	Nusselt number, -
P	Pressure, Pa
P_r	Reduced pressure, -
Pr	Prandtl number, -
q	Heat flux, W/m^2
q_{c}	Critical heat flux, W/m^2
Re	Reynolds number, -
RMS	Root-mean-square value, -
SD	Standard deviation, -
T	Temperature, ℃

$T_{\mathrm{V,a}}$	Actual vapor temperature, ℃
$T(k+1)$	Chauvenet's criterion, -
T_{MFB}	Minimum film boiling temperature, ℃
U	Velocity, m/s
U_{sV}	Superficial vapor velocity, m/s
w	Weighting factor, -
We	Weber number, -
x_{m}	Mass quality ($0 \leq x_{\mathrm{m}} \leq 1$), -
x_{a}	Actual quality, -
x_{e}	Equilibrium quality, -
z	Elevation, m

Greek

Symbol	Description
λ	Thermal conductivity, W/(m·℃)
μ	Dynamic viscosity, Pa·s
ρ	Density, kg/m^3
σ	Surface tension, N/m
β	Thermal expansion coefficient, 1/℃
δ	Thickness, m
α	Void fraction, -
τ	Standardized deviation, -
ε	Error parameter, -
π_{μ}	Viscosity ratio, -
π_{D}	Dimensionless diameter, -
π_{ρ}	Density ratio, -

Subscripts

Symbol	Description
b	Bulk
B	Vapor blanket
c	Critical

cal	Calculated
d	Droplet
eq	Equilibrium
exp	Experiment
EV	Evaporation
f	Film
w	Wall
i, j	Index
in	Inlet
L	Liquid phase
m	Measured
ref	Reference value
s	Saturated
pc	Pseudo-critical
TP	Two-phase
V	Vapor phase

Abbreviations

Symbol	Description
BWR	Boiling Water Reactor
CEA	French Alternative Energies and Atomic Energy Commission
CHF	Critical heat flux
CSP	Concentrating solar power
DNB	Departure from nucleate boiling
DO	dryout
FB	Film boiling
FPP	Fossil power plant
GFR	Gas Cooled Fast Reactor
GIF	Generation IV International Forum
GRS	Gesellschaft für Anlagen- und Reaktorsicherheit
HPLWR	High Performance Light Water Reactor
HTC	Heat transfer coefficient

HTD	Heat transfer deterioration
IATF	Institute for Applied Thermofluidics
INEEL	Idaho National Engineering and Environmental Laboratory
LOCA	Loss-of-coolant accident
LUT	look-up table
NB	Nucleate boiling
NVG	Net vapor generation
ORC	Organic Rankine cycle
PDO	Post-dryout
PWR	Pressurized Water Reactor
SCF	Supercritical fluid
sCO_2	Supercritical carbon dioxide
SCW	Supercritical water
SCWR	Supercritical Water-Cooled Reactor
SCWR-M	Mixed neutron spectrum SCWR
SFR	Sodium-Cooled Fast Reactor
STH	System Thermal-Hydraulic
TB	Transition boiling
TDV	Time dependent volume

1. Introduction

Substance above its critical temperature T_c and critical pressure P_c is referred as supercritical fluids (SCFs). As can be seen from Figure 1.1, the vapor-liquid phase change in the supercritical region disappears, and the fluid is always single-phase. With its unique properties, SCFs have been widely used in a variety of fields such as chemical engineering, power generation, refrigeration, and food engineering[1].

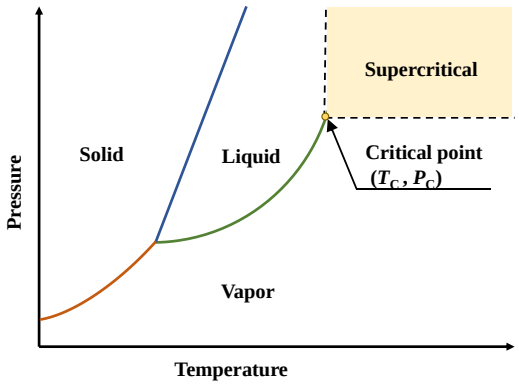

Figure 1.1.: Phase diagram (Pressure-Temperature) of substance[2]

1.1. Supercritical Power Cycles

With respect to the power generation, supercritical power cycles working with SCFs are of great interest for its higher thermal efficiency. Currently, supercritical water (SCW) and supercritical carbon dioxide (sCO_2) are actively considered as a coolant for power cycles throughout the world. For instance, compared to the conventional subcritical fossil power plants (FPP), the current commercial supercritical FPP and ultra-supercritical FPP improve the net efficiency from lower than 35% to 35-40% and 40-45%, respectively[3]. Besides, as reported by Marion et al.[4], the STEP 10 MWe SCO_2 Pilot Plant Demonstration would achieve a net efficiency over 50%. Particularly, supercritical power cycles have a great potential in waste heat recovery and clean energy application, such as nuclear energy, solar energy, geothermal energy, and bioenergy[5-7].

- Waste heat

The application market of the industrial waste is extraordinarily large, such as waste heat from metal mines, chemical plants, cement plants, gas turbines, and reciprocating engines. However, the development of the utilization of low temperature waste heat is still limited. The critical temperature of CO_2 is about 30.98 ℃, which allows the sCO_2 power cycles to be applied for various temperature ranges and therefore for low-temperature heat sources[7, 8]. Currently, organic Rankine cycle (ORC), with the flammable hydrocarbon-based organic as working fluid, is applied to use the low-temperature heat sources. For safety measures, an intermediate loop is used to transfer heat from the heat source to the organic fluid. Obviously, when applying sCO_2 power cycle to waste heat recovery, the safety measures are not required further, since CO_2 is nontoxic and nonflammable. Moreover, compared to ORC plants, the equipment size of sCO_2 power cycles would be smaller and it could work with even lower heat source temperature[9, 10].

- Nuclear energy

Supercritical Water-Cooled Reactor (SCWR), as the only reactor concept with supercritical water as working fluid, was recommended as one of the six most promising Generation IV reactor systems by the Generation IV International Forum (GIF)[11], based on advances made in the supercritical FPPs and the conventional Pressurized Water Reactors (PWRs). Designed to be operated at 25 MPa and outlet temperature over 500 ℃, the net efficiency of SCWR can reach up to 45%. In addition, due to a direct-cycle design with single-phase coolant, expensive plant components utilized in conventional nuclear power plants such as steam generators in PWR, or moisture separator and steam dryer in BWR are eliminated in SCWR. Hence, it results in a considerable reduction in capital costs[12-16].

Concepts of cooling system with sCO_2 power cycles have been proposed for various kinds of Generation IV reactors, as direct cycle and indirect cycle[17]. Compared to the most often considered gas cycles for Gas Cooled Fast Reactor (GFR), i.e., Helium cycles, the sCO_2 cycles eliminate the leakage problem practically, for CO_2 is a triatomic gas with a much higher molecular weight[18, 19]. The high density sCO_2 enables the cycle layout to be more compact and provides an acceptable size of heat exchangers. Taking place of the traditional Rankine superheated steam cycle, the application of sCO_2 Brayton cycle to the Sodium-Cooled Fast Reactor (SFR) could achieve higher efficiency and avoid considering the sodium-water reaction, since sCO_2 is stable and relative inert in the working range[20].

For Fusion reactors, a simple but high-efficiency sCO_2 Brayton cycle could realize the integration of all three main heat sources (i.e., blanket, divertor, and vacuum vessel) taking the advantage of the wide working range of sCO_2 Brayton cycle[21-23].

- Solar energy, geothermal energy, and bioenergy

sCO_2 power cycle is appealing to be utilized in renewable energy systems, not only taking the advantage of its higher efficiency, good power scalability (~10–150 MWe), smaller size, and simpler layout, but also for CO_2 is environment-friendly. Moreover, it allows concentrating solar power (CSP) plants to be applied in the desert places where water is scarce while solar energy is abundant[24-26]. Similar for dry geothermal reservoirs, in which water is inadequate, the energy resource could be captured by injecting cold sCO_2 through wells into the thermal plume[27, 28]. As indicated, another benefit is that 2% of the CO_2 flowing through the geothermal heat source would be captured in the well[8].

Moreover, regarding the heat transfer in a supercritical power cycle, since supercritical fluid is single-phase, the two-phase boiling crisis phenomena, which is a crucial criterion to conventional subcritical systems, is eliminated and becomes another advantage of the supercritical power cycle.

However, the supercritical system may experience trans-critical processes, in which the system pressure transfers between supercritical conditions and subcritical conditions, during startup, shutdown, and abnormal transients such as the loss-of-coolant accidents (LOCA). Obviously, the boiling crisis problem cannot be avoided when taking these trans-critical transients into consideration.

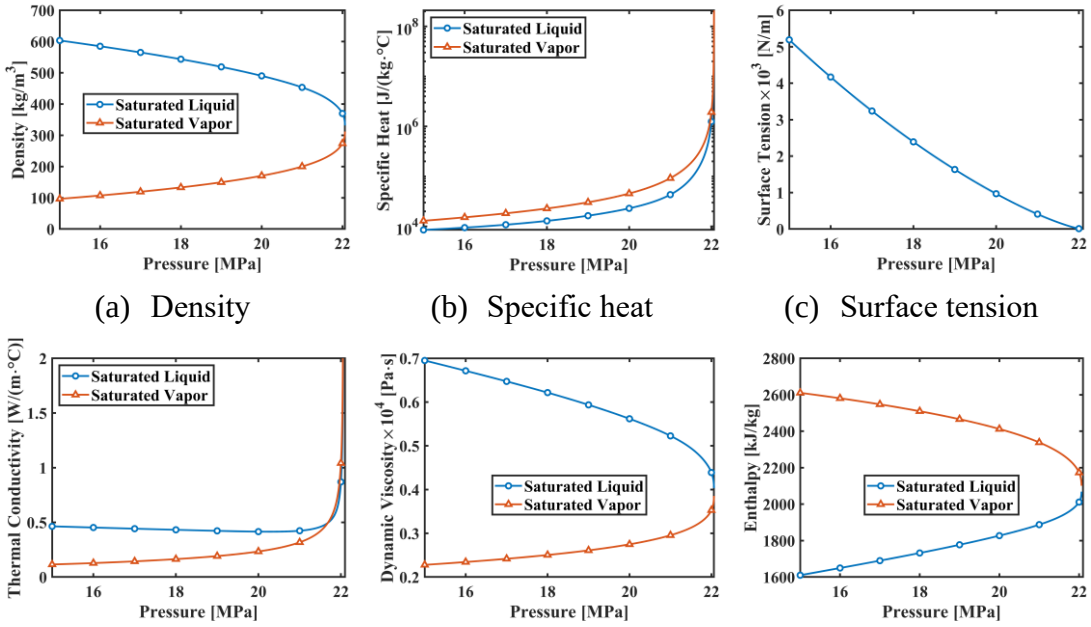

(a) Density (b) Specific heat (c) Surface tension

(d) Thermal conductivity (e) Dynamic viscosity (f) Enthalpy

Figure 1.2.: Variation of saturation properties in the high-pressure region for water[29]

As can be seen from Figure 1.2, thermal-property differences between the saturated vapor and saturated liquid will be smaller when the pressure increases, and in the high-pressure region, thermal properties change drastically. It is noted that the evaporation heat decreases to zero at the critical point, which may enhance the vaporization process.

Accordingly, it causes the occurrence of boiling crisis easier and may result in burnout of the heated wall. Furthermore, as experimentally observed by Hong et al.[30], the critical heat flux (CHF) converges to zero as the pressure raises up to the critical point. Thus, in the high-pressure region, even with a low heat flux, the boiling crisis could occur. Hence, to guarantee the system safety, heat transfer analysis of the trans-critical transient is of great significance for the supercritical systems.

1.2. Trans-critical Transient Heat Transfer Experiments

In the past twenty years, owing to the R&D of supercritical power cycles, heat transfer experiments during a trans-critical transient have been conducted.

Hong et al.[30] carried out trans-critical depressurization experiments with R134a (P_c = 4.059 MPa, T_c = 101.06 ℃) as coolant in a upward flow internally heated annulus. The system pressure began to decrease from supercritical pressure (4.14 MPa) to subcritical pressure, whereas the flow rate, inlet subcooling, and the supplied power were kept constant. As indicated, a sudden wall temperature heat up was observed as the system pressure crosses the critical point. As Hong et al.[30] stated, the boiling crisis occurred as soon as the pressure decreased to subcritical condition, and the post-CHF heat transfer region was thereby encountered, which resulted in the increase of the heated wall temperature.

Kang and Chang[31] performed trans-critical heat transfer experiments in a uniformly heated vertical tube cooled by R134a with pressure decreased from 4.5 MPa to 3.8 MPa. Likewise, for some locations, the heated wall started to increase abruptly at the critical point. Moreover, as experimentally investigated when the pressure transient rate varied from 1.1 to 13.6 kPa/s, the influence of the pressure gradient on the heat transfer could be neglected.

Trans-critical heat transfer experiments of 5×5 heated rod bundles with R134a was conducted by Watanabe et al.[32]. They performed both depressurization and pressurization trans-critical experiments, with system pressure changing between 3.4 MPa to 4.2 MPa. As the measurements indicated, boiling crisis was induced, and the post-CHF heat transfer mode was kept in the near critical region. The wall temperature profile versus the system pressure in the depressurization transients were almost the same as that in the pressurizing process. In the depressurization transients, the wall temperature started to increase rapidly when the pressure approaches the critical point, and the wall temperature drop was observed since the post-CHF stage was ended at lower pressure. It was demonstrated that the pressure corresponding to the end of the boiling crisis in the depressurizing process was lower than the pressure for the begin of boiling crisis in the pressurization transient.

Zhang[33] investigated the heat transfer behaviors during depressurizing trans-critical transients of R134a flowing in a vertical round tube. The system pressure decreased

from 4.3 MPa to 3.7 MPa with pressure gradient around 20 kPa/s. In the supercritical condition, the wall temperature reduced systematically as the pressure decreased. When the system pressure crossed the critical point, the wall temperature increased in some cases due to the two-phase boiling crisis. At the end of the pressure transient, the wall temperature could exceed the initial value in the supercritical condition. While for cases without boiling crisis, the wall temperature decreased with the pressure descending.

Trans-critical heat transfer experiments with water as a working fluid have been performed by Hu[34] in 2×2 rod bundle with wrapped wire. With the pressure transient rate at 16.7 kPa/s, the system pressure descended from 25 MPa to 17 MPa. Similarly, for cases with the occurrence of boiling crisis, an abrupt wall heat up was observed at the critical point. However, the wall temperature did not keep increase during the depressurizing process. It dropped suddenly at a lower pressure condition, owing to recovery from post-CHF to nucleate boiling heat transfer.

In general, as confirmed by experiments, when the pressure drops from supercritical to subcritical condition, the wall temperature is possible to rise suddenly after crossing the critical point in case that boiling crisis occurs and post-CHF regime is encountered. As experimentally investigated by Watanabe et al.[32] and Hu[34], the heated wall may get rewetted at a lower pressure condition. Besides, referring to heat transfer experiments under supercritical pressure carried out by Shitsman et al.[35], the occurrence of heat transfer deterioration may lead to drastic heat-up of the heated wall. Therefore, to capture the wall temperature profile during the trans-critical transient, the heat transfer model not only at supercritical condition but also at subcritical condition should be considered.

1.3. Thermal-Hydraulic Codes for Supercritical System

Various well validated System Thermal-Hydraulic (STH) codes for design and safety analyses, e.g., RELAP5, CATHARE, ATHLET, have been upgraded to the supercritical condition. As mentioned above, the vapor-liquid phase change disappears at the critical point and supercritical fluids are single-phase. If simply assign the void fraction to one or zero for the supercritical condition, once the critical pressure is approached during a trans-critical transient, the sudden void fraction transition may cause divergence in simulation. For this reason, conventional STH codes with two-fluid model would fail to run trans-critical transients for safety analysis of supercritical systems. Thereby, special modifications are implemented[36-38].

- RELAP5

RELAP5 codes was developed by the Idaho National Engineering and Environmental Laboratory (INEEL) for U.S. Nuclear Regulatory Commission, originally aiming to simulate transients of PWR. It has been extended to various thermohydraulic transient for both nuclear and nonnuclear systems. With respect to applying RELAP5 to

supercritical condition, it was found that only a few supercritical cases and trans-critical blowdown transients could be executed even though properties of supercritical water were implemented. Therefore, several additional modifications were carried out to make it executable, including changes in the water-steam property tables and interfacial heat transfer coefficient for vapor. For instance, at the critical point, property derivatives for specific heat, volume expansivity, and isothermal compressibility were assigned to consistent values. Furthermore, heat transfer models and fluid-wall friction models were upgraded to supercritical pressures. The modified RELAP5 successfully performed the transient simulation of a small break LOCA for the SCWR proposed by INEEL[36].

- CATHARE

The French STH code CATHARE was originally developed for safety analyses of PWR by French Alternative Energies and Atomic Energy Commission (CEA) cooperated with EDF, FRAMATOME and IRSN[39]. In the framework of the High Performance Light Water Reactor European project (HPLWR Phase 2), CATHARE was extended to the application for supercritical water[40]. The IAPWS-97 thermodynamic properties package[41] was utilized with high-order splines at boundaries between different IAPWS-97 formulation regions, to ensure the accuracy and continuity of the physical properties. Heat transfer correlations and pressure drop correlations for supercritical flows were added according to the review works of Pioro et al.[42, 43]. Besides, supercritical fluids were modeled with a pseudo two-phase model according to the fluid temperature. In case the fluid temperature is lower than the pseudo-critical temperature, it is treated as pseudo-liquid with void fraction at zero, otherwise, regarded as pseudo-vapor with void fraction at 1.0. The modified CATHARE successfully performed the preliminary simulation of LOCA transients for the HPLWR.

- ATHLET-SC

ATHLET is an advanced STH simulation code developed by Gesellschaft für Anlagen- und Reaktorsicherheit (GRS) in Germany[44]. Based on a highly modular code structure, the STH code ATHLET provides simulations with the one-dimensional, two-phase fluid dynamic models[44]. To satisfy the requirement of the safety analysis of supercritical power systems, the modified version, ATHLET-SC, was developed based on ATHLET Mod 2.1 Cycle A[37, 45]. ATHLET-SC implemented the IAWPS-IF97 formulations to extend the water-steam properties package to supercritical pressure. The heat transfer correlation, wall friction model, interfacial mass transfer model, and the critical flow model were also upgraded to supercritical condition. In addition, as Figure 1.3 shows, in the supercritical condition, a narrow two-phase region was proposed and applied with a pseudo evaporation enthalpy. Selecting the pseudo critical temperature as pseudo saturation temperature, the saturated vapor line and saturated liquid line is determined by the pseudo saturation line and pseudo evaporation enthalpy. Fluids at supercritical pressure are thereby separated to three regions, i.e., pseudo-vapor, pseudo-liquid, and pseudo two-phase, which is as well as in the subcritical condition. As a result, the abrupt

transition at the critical point is smoothed and the code numerical robust could get guaranteed when applied for trans-critical transients. Preliminary simulation and safety system design of the mixed neutron spectrum SCWR (SCWR-M) were carried out with ATHLET-SC, for the loss of flow accident[46] and loss of coolant accident[47].

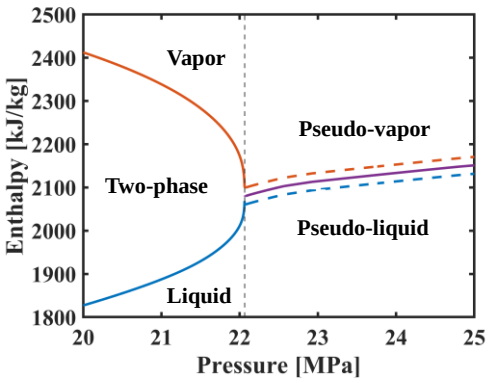

Figure 1.3.: Schematic of the pseudo two-phase model

Overall, based on conventional safety analysis code, some STH codes have been extended to supercritical pressures. Except the strategy to guarantee the numerical stability at both near critical and supercritical conditions, the modifications were mainly focusing on upgrading thermal-dynamic models for supercritical condition, e.g., models for heat transfer, friction, interfacial mass transfer, and critical flow. As a result, the modified STH codes can perform thermal-hydraulic analysis of supercritical systems at steady-state supercritical conditions and trans-critical transients.

However, these STH codes were originally validated and qualified for PWR or BWR, of which the working pressure is only up to 15.5 MPa for water. Since heat transfer models utilized in STH codes usually cannot be extended to the range out of validity, when applied for SCWR safety analysis, there remains a vacancy in the high-pressure subcritical region between 15.5 MPa, of which the reduced pressure (P/P_c) is about 0.7, and the critical pressure (P_c) is at 22.064 MPa. Especially, as indicated by trans-critical heat transfer experiments, owing to the low value of CHF in the high-pressure region, the heated wall may experience a sudden temperature rise in the near critical region. Therefore, reliable models of CHF and post-CHF heat transfer for the high-pressure region are required to improve the prediction accuracy of STH codes for the simulation of trans-critical transients.

1.4. Research Objectives

As discussed above, there has been a considerable interest of supercritical power cycles in recent years, mainly for its advantage of high efficiency and reduction in capital costs.

Though designed to be operated above critical pressure, under some transient conditions, the supercritical power cycle system may experience trans-critical transients

with pressure transferring between supercritical to subcritical condition. As observed in trans-critical heat transfer experiments, the heated wall would possibly have a sudden heat up as the pressure crosses the critical point when boiling crisis occurs in the subcritical condition. Besides, high-pressure CHF experiments indicate that in the high-pressure condition, the increase in pressure leads to a lower CHF. Therefore, when working at high-pressure conditions, the supercritical power system may meet the burnout problem even though the supplied heat flux is in a low level. Hence, the heat transfer analysis of these trans-critical procedures is necessary.

Although some STH codes have been extended to supercritical condition and could perform the simulation of trans-critical transient successfully, heat transfer models have not been upgraded yet in the high-pressure subcritical region from 15.5 MPa to the critical pressure. Thus, it requires well validated heat transfer models for the high-pressure condition, especially the CHF model which determines whether the heat-up occurs, and the post-CHF heat transfer model to predict the wall temperature.

Thereby, for supercritical power cycles, to make sure the prediction of trans-critical transients, heat transfer at supercritical condition and high-pressure subcritical condition should be paid attention to. The main objective of the present work contains the following aspects.

- Review and update research status about the heat transfer characteristics for supercritical fluids. Summarize and compare different prediction methods of heat transfer at supercritical pressure.
- Review the mechanism of boiling crisis and post-CHF heat transfer; summarize and assess different prediction approaches. Establish new experiment databanks and examine previous prediction methods for the high-pressure condition. If necessary, develop new prediction method of CHF and post-CHF heat transfer for the high-pressure condition.
- Modify the STH code ATHLET-SC, with selected high-pressure heat transfer models (i.e., CHF model and post-CHF heat transfer model) and heat transfer model for the supercritical pressures. Evaluate the performance of the modified ATHLET-SC code with the aid of trans-critical transient experiments.

2. Fundamentals and Literature Reviews

This chapter describes basic knowledge about heat transfer in the supercritical condition, boiling crisis, and heat transfer in the post-CHF region. Different prediction methods are summarized and discussed.

2.1. Heat Transfer to Fluids at Supercritical Pressure

2.1.1. Properties of Fluids at Supercritical Pressure

As indicated in Figure 2.1, the temperature at which the specific heat reaches a sharp peak is termed as pseudo-critical temperature (T_{pc}). The properties vary drastically in a narrow band near T_{pc}. The variation of properties with temperature is continuous. In the supercritical region, the phase change of substances disappears. Therefore, supercritical fluids are single-phase.

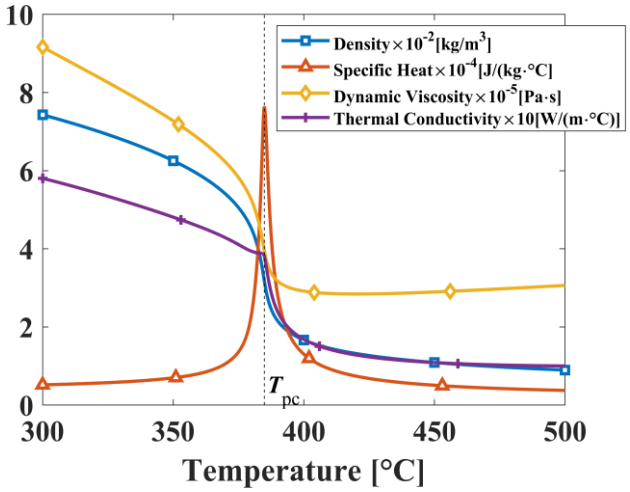

Figure 2.1.: Variation of properties with temperature for water at 25 MPa[29]

For water at 25 MPa, as illustrated in Figure 2.1, the density, dynamic viscosity, and thermal conductivity fall with the increase of temperature, while the dramatic peak like the specific heat peak is not observed. However, there is a small increase of the thermal conductivity at T_{pc}. Further, the variation of properties at different supercritical pressures is compared in Figure 2.2. As the pressure increases, the T_{pc} rises and the

magnitude of the specific heat peak drops. As Figure 2.2 (d) shows, at the pressures of 22.1 MPa and 23.0 MPa, the thermal conductivity reaches extreme peaks and gets recovered immediately near T_{pc}. Besides, the change of the density and the dynamic viscosity around the pseudo-critical temperature also becomes less severe as the pressure increases further.

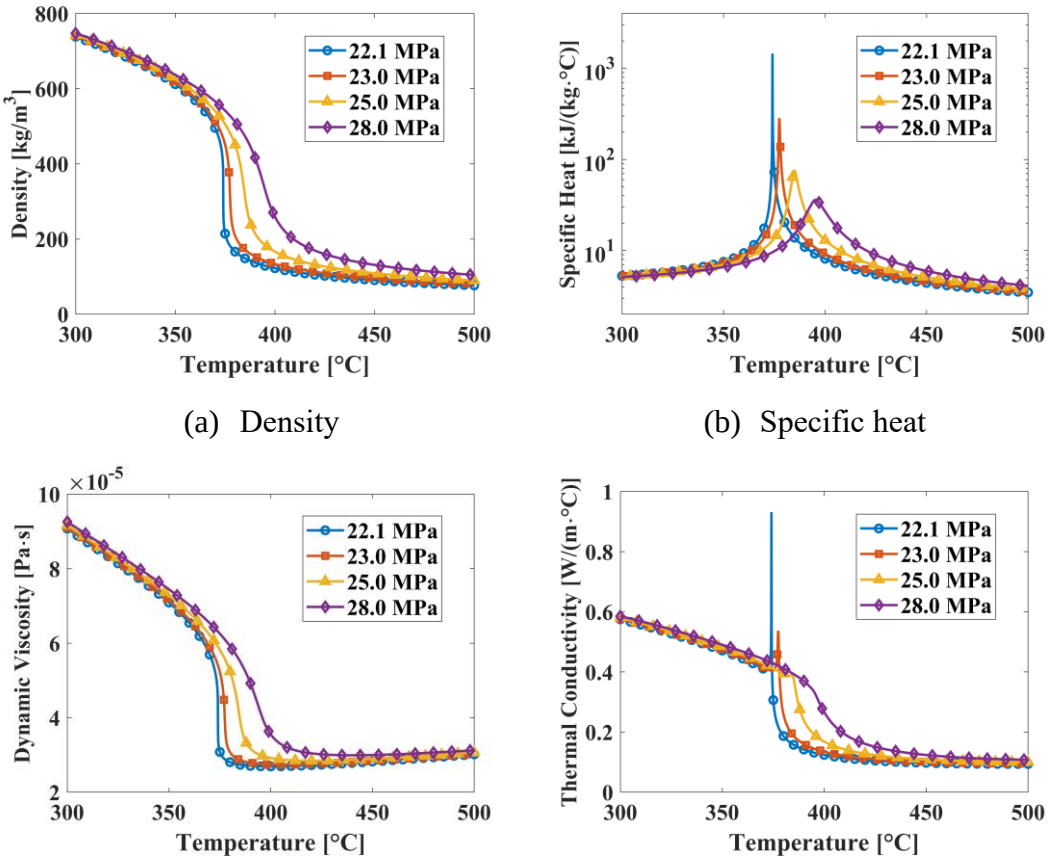

(a) Density (b) Specific heat

(c) Dynamic viscosity (d) Thermal conductivity

Figure 2.2.: Variation of properties with the temperature and pressure for water[29]

2.1.2. Heat Transfer Characteristics of Supercritical Fluid

Due to its large variation of properties for supercritical fluids especially near the pseudo-critical region, the heat transfer behavior with the supercritical fluids is different to conventional fluids. Previous systematical reviews have been provided by Jackson et al. [35, 48], Jaeger et al.[49], Pioro[50], Licht[51], Cheng et al.[13, 52], etc.

Figure 2.3 shows the results of the experiments conducted by Shitsman et al.[35] with supercritical water in 1963. The experiments were carried out with upward flow in a heated circular tube of 8 mm diameter, at a pressure of 23.3 MPa, mass flux of 430 kg/(m^2·s), and inlet enthalpy of 1465 kJ/kg. As can be seen, the wall temperature increases systematically at low heat fluxes of 221 kW/m^2 and 281 kW/m^2. However, at higher heat fluxes i.e., 300 kW/m^2, 337 kW/m^2, and 386 kW/m^2, the wall temperature

exhibits apparent peaks, which implies that the local heat transfer capability has a drastic reduction. The phenomenon of the heat transfer reduction at supercritical pressures is referred as 'heat transfer deterioration (HTD)'. Obviously, the occurrence of HTD could cause the damage of the heating wall in the supercritical condition. Hence, it has to be taken into consideration in heat transfer analyses.

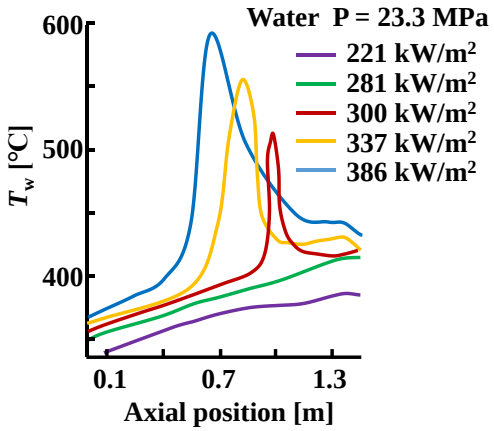

Figure 2.3.: Heat flux effect on heat transfer for water at 23.3 MPa with upward flow in a heated tube[35]

According to early review and assessment work by Schatte et al.[53] and Feuerstein[54], the prediction method of the onset of the HTD has been provided by several authors in the past six decades, though it is still a controversial topic.

Koshizuka et al.[55] defined a heat transfer coefficient ratio as the criterion of the HTD, given in Eq.(2.1). h is the heat transfer coefficient (HTC, see Eq.(2.2)) calculated from results of heat transfer experiments, in which q, T_w, and T_b are the heat flux, wall temperature, and bulk fluid temperature, respectively. h_DB is the HTC calculated by the Dittus-Boelter correlation, shown in Eq.(2.3). λ_b, μ_b, and $c_{p,\mathrm{b}}$ are thermal conductivity, dynamic viscosity, and the specific heat of the bulk fluid, respectively. D_h stands for the hydraulic diameter of the tube, G for the mass flux. The conditions under which the heat transfer coefficient ratio lower than 0.3 is identified as HTD conditions.

$$h/h_\mathrm{DB} < 0.3 \tag{2.1}$$

$$h = \frac{q}{T_\mathrm{w} - T_\mathrm{b}} \tag{2.2}$$

$$h_\mathrm{DB} = 0.023 \cdot \left(\frac{G D_\mathrm{h}}{\mu_\mathrm{b}}\right)^{0.8} \cdot \left(\frac{\mu_\mathrm{b} c_{p,\mathrm{b}}}{\lambda_\mathrm{b}}\right)^{0.4} \cdot \frac{\lambda_\mathrm{b}}{D_\mathrm{h}} \tag{2.3}$$

Yamagata et al.[56] developed a correlation of the onset of HTD , as seen in the Eq.(2.4). Additionally, as demonstrated by Koshizuka et al.[55], experimental conditions judged as HTD by Eq.(2.4) agree with Eq.(2.3).

$$q = 200 \cdot G^{1.2} \tag{2.4}$$

Cheng et al.[57] proposed a criterion with considering the effect of the mass flux and pressure, as Eq.(2.5) shows. $c_{p,\mathrm{pc}}$ and β_{pc} denote the specific heat and the thermal expansion coefficient at the pseudo-critical point, respectively. It is illustrated by the Eq.(2.5) that the heat flux corresponding to the onset of HTD rises when the pressure increases.

$$q = 1.354 \times 10^{-3} \cdot G \cdot \frac{c_{p,\mathrm{pc}}}{\beta_{\mathrm{pc}}} \tag{2.5}$$

Although the HTD phenomenon in the supercritical condition has been observed for sixty years, there is still no clear explanation for it. Currently, the effect of buoyancy and thermally-induced bulk flow acceleration on the heat transfer at supercritical conditions has been highlighted by the International Atomic Energy Agency (IAEA), while it is still undergoing[58].

2.1.3. Prediction Methods for Heat Transfer at Supercritical Condition

Due to the dramatic variation of properties and the occurrence of HTD, conventional approaches to predict heat transfer at subcritical condition cannot be applied to supercritical condition directly. So far, large numbers of heat transfer prediction approaches for supercritical conditions have already been proposed. Extensive overview and assessment of prediction methods for the heat transfer at supercritical condition have been prepared by Pioro[50], Kurganov[59], Zahlan[60], Zhao[61], Cheng et al[62], etc.

2.1.3.1. Heat Transfer Correlation for Supercritical Pressure

Numerous heat transfer correlations for supercritical pressures have been proposed. As concluded by Zhao[61], most correlations were developed from experimental results by modifying the Dittus-Boelter correlation with the structure in,

$$Nu = C \cdot Re_{\mathrm{X1}}^{\mathrm{N}} \cdot Pr_{\mathrm{X2}}^{\mathrm{M}} \cdot F \tag{2.6}$$

where Nu, Re, and Pr stands for the Nusselt number, Reynolds number, and Prandtl number, respectively. The subscript X1 and X2 denote the temperature used to evaluate the properties in Re and Pr. C, M, and N are constant coefficients. F is the correction factor.

As indicated by Eq.(2.7), for the Bishop correlation[63], the coefficients C, M, and N equal to 0.006, 0.9, and 0.66, respectively. The Reynolds number (see Eq.(2.8)) and Prandtl number (see Eq.(2.9)) are both calculated with the properties at the bulk temperature, where μ_{b} and λ_{b} are devoted for the dynamic viscosity and thermal conductivity at the bulk temperature. Especially, the average specific heat $\bar{c}_{p,\mathrm{b}}$ is defined in Eq.(2.10) due to its drastic variation near the pseudo-critical point. H_{w} and

H_b are the enthalpy at the wall temperature T_w and the bulk temperature T_b, respectively. The correction factor is introduced by considering the wall temperature effect with the density ratio $\rho_\mathrm{w}/\rho_\mathrm{b}$. More correlations in the structure of the Dittus-Boelter correlation were summarized by Zhao[61].

$$Nu = 0.0069 \cdot Re_\mathrm{b}^{0.9} \cdot \overline{Pr}_\mathrm{b}^{0.66} \cdot \left(\frac{\rho_\mathrm{w}}{\rho_\mathrm{b}}\right)^{0.43} \tag{2.7}$$

$$Re_\mathrm{b} = \frac{GD_\mathrm{h}}{\mu_\mathrm{b}} \tag{2.8}$$

$$\overline{Pr}_\mathrm{b} = \frac{\mu_\mathrm{b}\bar{c}_{p,\mathrm{b}}}{\lambda_\mathrm{b}} \tag{2.9}$$

$$\bar{c}_{p,\mathrm{b}} = \frac{H_\mathrm{w} - H_\mathrm{b}}{T_\mathrm{w} - T_\mathrm{b}} \tag{2.10}$$

Krasnoshchekov et al.[64] together with Petukhov et al.[65] proposed a correlation independent to the Dittus-Boelter correlation (see Eq.(2.11)). The friction factor f is included to calculate the Nu_0. Property ratios of the dynamic viscosity, thermal conductivity, and the specific heat are introduced to give a correction to Nu_0.

$$Nu = Nu_0 \cdot \left(\frac{\mu_\mathrm{b}}{\mu_\mathrm{w}}\right)^{0.11} \cdot \left(\frac{\lambda_\mathrm{b}}{\lambda_\mathrm{w}}\right)^{-0.33} \cdot \left(\frac{\bar{c}_{p,\mathrm{b}}}{c_{p,\mathrm{b}}}\right)^{0.35} \tag{2.11}$$

$$Nu_0 = \frac{\left(\frac{f}{8}\right) Re_\mathrm{b}\overline{Pr}_\mathrm{b}}{12.7\sqrt{\frac{f}{8}}\left(\overline{Pr}_\mathrm{b}^{\frac{2}{3}} - 1\right) + 1.07} \tag{2.12}$$

$$f = \frac{1}{(1.82\log_{10} Re_\mathrm{b} - 1.64)^2} \tag{2.13}$$

Cheng et al.[57] derived a new dimensionless parameter π_A (acceleration number), to

$$\pi_\mathrm{A} = \frac{\beta}{c_p}\frac{q}{G} \tag{2.14}$$

consider the acceleration effect, where β is the thermal expansion coefficient, c_p the specific heat at the bulk temperature. q stands for the heat flux, G for the mass flux. Recently, in 2019, Cheng et al.[62] extended their heat transfer databank to more than 90,000 data points, in which more than 50% data points are possibly under HTD condition. However, as reviewed by Cheng and Shulenberg[66], most of previous heat transfer correlations fails to predict HTD conditions. Thereby, a part of SCW water data is applied to develop heat transfer correlations which are also suitable for HTD conditions. Two correlations are proposed with given heat flux,

$$Nu = 0.023 \cdot Re_{\mathrm{b}}^{0.8} \cdot Pr_{\mathrm{b}}^{1/3} \cdot F_{\mathrm{q1}} \cdot F_{\mathrm{q2}} \tag{2.15}$$

$$F_{\mathrm{q1}} = \begin{cases} 0.98, \pi_A \times 10^4 < 1.75 \\ 0.85 + 0.056(\pi_{\mathrm{A}} \times 10^4)^{1.5}, 1.75 \leq \pi_{\mathrm{A}} \times 10^4 \leq 3.75 \\ \dfrac{13.1}{4.5 + (\pi_{\mathrm{A}} \times 10^4)^{1.35}}, \pi_{\mathrm{A}} \times 10^4 > 3.75 \end{cases} \tag{2.16}$$

$$F_{\mathrm{q2}} = \begin{cases} 0.93 Pr_{\mathrm{b}}^{0.265}, \ Pr_{\mathrm{b}} \leq 2.5 \\ 1.66 Pr_{\mathrm{b}}^{-0.333}, Pr_b > 2.5 \end{cases} \tag{2.17}$$

and given wall temperature,

$$Nu = 0.023 \cdot Re_{\mathrm{b}}^{0.8} \cdot Pr_{\mathrm{b}}^{\frac{1}{3}} \cdot F_{\mathrm{Tw1}} \cdot F_{\mathrm{Tw2}} \cdot F_{\mathrm{Tw3}} \tag{2.18}$$

$$F_{\mathrm{Tw1}} = \frac{2.10}{1.40 + \left(\dfrac{\bar{c}_{p,\mathrm{b}}}{c_{p,\mathrm{b}}}\right)^{0.92}} \tag{2.19}$$

$$F_{\mathrm{Tw2}} = \begin{cases} 1.0, \ Pr_{\mathrm{b}} \leq 6 \\ 0.764 Pr_{\mathrm{b}}^{0.167}, Pr_{\mathrm{b}} > 6 \end{cases} \tag{2.20}$$

$$F_{\mathrm{Tw3}} = \begin{cases} 1.44 \times \left(\rho_{\mathrm{b}}/\rho_{\mathrm{w}}\right) - 0.48, \rho_{\mathrm{b}}/\rho_{\mathrm{w}} \leq 1.3 \\ 1.584 \times \left(\rho_{\mathrm{b}}/\rho_{\mathrm{w}}\right)^{-0.49}, \ \rho_{\mathrm{b}}/\rho_{\mathrm{w}} > 1.3 \end{cases} \tag{2.21}$$

In the Eqs.(2.15)–(2.21), F_{q1}, F_{q2}, F_{Tw1}, F_{Tw2}, and F_{Tw3} denote the correction factors. $Pr_{\mathrm{b}} = \mu_{\mathrm{b}} c_{p,\mathrm{b}}/\lambda_{\mathrm{b}}$ is the Prandtl number under the bulk temperature. π_{A} stands for the acceleration number given by Eq.(2.14). $\bar{c}_{p,\mathrm{b}}$ is devoted for the averaged specific heat calculated by Eq.(2.10), $c_{p,\mathrm{b}}$ for the specific heat at the bulk temperature. ρ_{b} and ρ_{w} are density at the bulk temperature and the wall temperature, respectively.

As demonstrated by Cheng et al.[62], the prediction ability of these two correlations, i.e., Eq.(2.15) and Eq.(2.18), achieve good agreement with validation experiments including supercritical water data, the supercritical R134a data, and supercritical CO_2 data. Compared to previous correlations, Cheng's correlations[62] provide a better predictive capability. Moreover, it is illustrated by Zhao et al.[67] that when implemented into STH code, the heat transfer correlation with given heat flux, i.e., Eq.(2.15), could give a better prediction accuracy. Considering the above aspects, Cheng correlation with given heat flux is recommended.

2.1.3.2. Look-up Table for Heat Transfer at Supercritical Condition (SC LUT)

The look-up table (LUT) is usually established by 'localized best fitting' procedures based on experimental results near the proposed grid points. Normally, a great number

of experimental data points are required to fill the table skeleton. To date, three look-up tables have been developed for the heat transfer of supercritical water with vertical flow in uniformly heated circular tubes.

Loewenberg et al.[68] established a SC LUT, which is a five-dimensional table providing the wall temperatures as a function of the mass flux, heat flux, pressure, tube diameter, and bulk enthalpy. In the look-up table, the mass flux range is 700–3500 kg/(m^2·s), heat flux 300–1600 kW/m^2, pressure 22.5–25 MPa, tube diameter 8–20 mm and bulk enthalpy 1200–2700 kJ/kg.

Liu developed a SC LUT with their own databank[69]. However, considering the large deviation in the amount of data points for different tube diameters, the tube diameter is excluded from the basic dimensional parameters. Thus, nine tables for nine different diameters i.e., 7 mm, 8 mm, 9 mm, 10 mm, 12 mm, 18 mm, 20 mm, 24 mm, and 26 mm, are established separately. However, except the tables for 10 mm, 12 mm, and 20 mm, the other six remain a lot of vacancy owing to the shortage of experimental data points. Liu's LUT contains pressures in the range from 22.5 to 31.3 MPa, mass flux from 407 to 3500 kg/(m^2·s), heat flux from 158 to 2000 kW/m^2, and the bulk enthalpy from 300 to 3000 kJ/kg.

Zahlan's LUT[70] provides the HTC rather than the wall temperature as Loewenberg et al.[68] or Liu[69] did. HTC is given as a function of the pressure, mass flux, wall superheat, and the bulk enthalpy. The tube diameter was fixed to 8 mm i.e., d_{ref}, hence, to construct the LUT, the experimental HTC with different diameter from 8 mm was scaled to it with,

$$h_{\mathrm{ref}} = h_{\mathrm{m}} \left(\frac{D_{\mathrm{h}}}{D_{\mathrm{ref}}} \right)^{n} \tag{2.22}$$

Here, h_{ref} is the HTC in 8 mm (D_{ref}) tubes after scaling. h_{m} and D_{h} denote the measured HTC and tube diameter in experiments. Corresponding to tube diameter in 5 mm, 6 mm, 9 mm, 10 mm, 14 mm, 15 mm, and 16 mm, the exponent n is given the values 0.075, 0.09, 0.10, 0.12, 0.15, 0.20, and 0.25, respectively. The LUT covers the pressure range of 19–30 MPa, mass flux of 100–500 kg/(m^2·s), the bulk enthalpy of 1000–3000 kJ/kg, and the wall superheat of 10–500 ℃.

Except Loewenberg's LUT[68], the SC LUT established by Liu[69] or Zahlan[70] is capable of predicting the HTC under HTD conditions. It should be noted that, these SC LUTs are developed from water experiments and therefore could not be applied to other coolants directly.

2.1.3.3. Phenomenological Model for Heat Transfer at Supercritical Condition

As mentioned in Section 2.1.1, at the supercritical condition, although fluids remain single-phase, the variation of properties with the temperature is nonlinear especially

near the pseudo-critical point, which makes it difficult to develop a mathematical model for the heat transfer at supercritical condition[71].

Referring to the publication of IAEA Coordinated Research Project (CRP) about heat transfer behavior related to SCWRs[58], phenomenological model developed by Jackson[72] is highlighted. As Jackson[72] stated, for supercritical fluids flowing in uniformly heated vertical tubes, the radial distribution of shear stress is modified under the influence of buoyancy or thermally-induced bulk flow acceleration. It changes the amount of turbulence production and thereby affects the heat transfer by turbulent diffusion. Accordingly, taking into account the non-uniformity of properties of supercritical fluids, Jackson[72] obtained Nusselt number ratios between buoyancy influenced and buoyancy-free flow, and between thermally-induced bulk flow acceleration effected and acceleration-free flow, respectively. However, Jackson's model[73] can only provide qualitative prediction but is still incapable of determining the HTC values directly so far. Further research is still undergoing[73].

2.2. Boiling Crisis & Critical Heat Flux

2.2.1. General

The boiling crisis occurs when the heat flux raises up to a high level that the heated surface can no longer support the continuous liquid contact[74]. The heat flux at the boiling crisis point is usually referred as critical heat flux (CHF). Since the poor heat transfer capability of vapor, the boiling crisis could lead to failure of the heated surface. Therefore, it is a significant safety limitation to heat transfer.

Regarding to flow boiling in a pressure duct, two boiling crisis mechanisms are supposed to be considered[75].

The first is referred as 'departure from nucleate boiling (DNB)', as shown in Figure 2.4(a), occurring in a subcooled or low-quality condition. The upstream of the DNB point is the so-called 'nucleate boiling' (bubbly flow). After the DNB point, the flow pattern transfer to inverted annular flow, where the liquid phase forms as a continuous core with dispersed vapor bubbles, while the vapor phase flows along the wall. Since vapor flows faster, it causes instabilities in the liquid core and leads to break up of the liquid core. The flow will transfer to dispersed droplet flow in which the liquid droplets dispersed in the vapor phase[75].

Figure 2.4(b) exhibits another kind of boiling crisis, 'dryout (DO)'. The upstream of the DO point is an annular flow, where the liquid film flows along the heated wall. Then, the dryout of the liquid film leads to dispersed droplet flow where the liquid droplets dispersed in vapor phase, and the heated wall lost the cooling through continuous liquid phase. Normally, the dryout type boiling crisis occurs under higher quality[75].

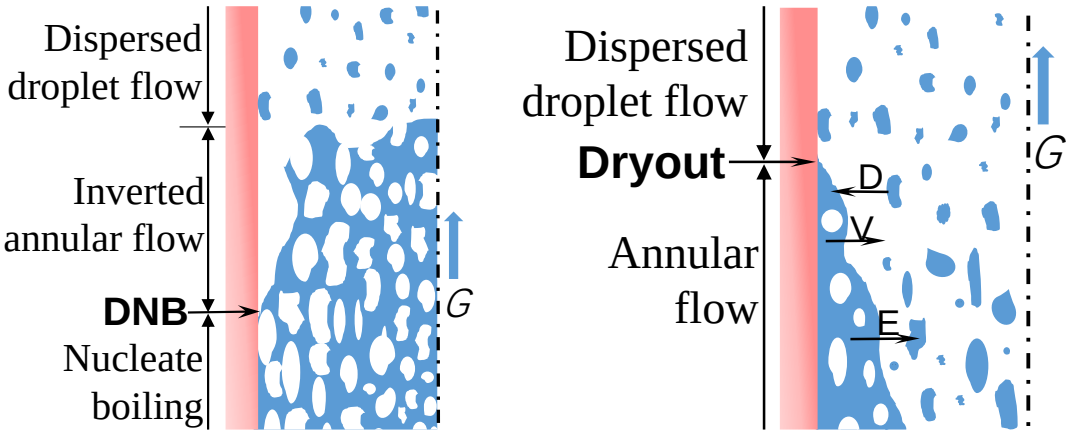

(a) DNB (b) Dryout

Figure 2.4.: Flow patterns near the CHF point for flow boiling[75]

2.2.2. Boiling Crisis Mechanism

As mentioned above, since there is significant difference in heat transfer characteristic for various flow patterns, the boiling crisis must be explained by different mechanisms. This section describes the mechanisms of DNB and dryout, respectively.

DNB

As reviewed by Bruder[76], the mechanism for DNB is still to be understood. Currently, the sublayer dryout model and the bubble crowding model are the focus of attention.

- Sublayer Dryout Model[77]: As can be seen in Figure 2.5, near the heated wall, vapor blankets are generated due to the coalescence of small bubbles. Between the vapor blanket and the heated wall, there remains a thin liquid sublayer. The boiling crisis occurs when the liquid sublayer is completely dryout.
- Bubble Crowding Model[78]: The bubbly layer builds up near the heated wall (see Figure 2.6). Boiling crisis occurs when bubble layer fills the near wall region and the bulk cold liquid to reaching the heated wall is prevented by bubble crowding near the heated wall.

Dryout

In annular flow, as shown in Figure 2.4 (b), the thickness of the liquid film is determined by the deposition ('D') of the droplets to the liquid film, and the entrainment ('E') and vaporization ('V') of the liquid film to the core region. The liquid film loses liquid from the entrainment and vaporization procedures, while it receives liquid caused by deposition. Boiling crisis will occur when the liquid film of the annular flow disappears.

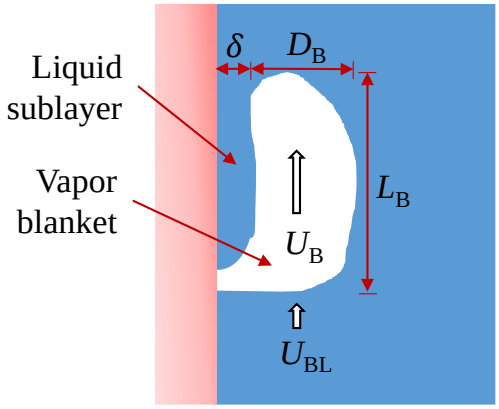

Figure 2.5.: Schematic of sublayer dryout model

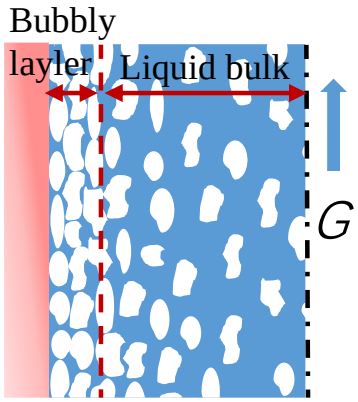

Figure 2.6.: Schematic of bubble crowding model

2.2.3. CHF Prediction Methods

To date, numerous of prediction methods for CHF have been proposed, especially as a result of the R&D for nuclear power plants.

2.2.3.1. CHF Correlation

Hundreds of CHF correlations have been proposed for various flow conditions[79]. In this section, two commonly used CHF correlations for conventional light water reactors (PWR and BWR) are introduced hereunder.

- W-3 correlation[80]

$$\begin{aligned} q_c = {} & 3.154 \times 10^6 \cdot \{(2.022 - 6.238 \times 10^{-8} P) \\ & + (0.1722 - 1.43 \times 10^{-8} P) \\ & \times \exp[(18.177 - 5.987 \times 10^{-7} P) x_e]\} \\ & \times [(0.1484 - 1.596 x_e + 0.1729 x_e |x_e|) \\ & \times 7.373 \times 10^{-4} G + 1.037](1.157 - 0.869 x_e) \\ & \times [0.2664 + 0.8357 \exp(-124.055 D_h)] \\ & \times [0.8258 + 0.341 \times 10^{-6} (H_{LS} - H_{in})] \end{aligned} \tag{2.23}$$

Developed by Tong[80] for uniformly heated round tubes, the well-known W-3 correlation is one of the most widely applied CHF correlations for PWR. q_c denotes the CHF in W/m^2. P is for the pressure in Pa, x_e for equilibrium quality, G for mass flux in kg/(m^{2}s), D_h for hydraulic diameter. H_{LS} and H_{in} are devoted for the saturated liquid enthalpy and the inlet enthalpy with unit in J/kg, respectively. As stated, the range of validity is for pressure between 6.8957–15.86 MPa, mass flux from 1360 to 6800

kg/(m^2·s), equilibrium quality for -0.2–0.15, hydraulic diameter for 5–17.8 mm, and the inlet enthalpy above 930 kJ/kg.

- Israel-Casterline-Matzner correlation[81]

$$q_{\mathrm{c}} = 3.154 \times 10^{6}[(0.688 + 1.144 \times (7.37 \times 10^{-4} G)^{1.4}) - (0.831 + 0.211 G'^{2.72})] \cdot x_{\mathrm{e}} \tag{2.24}$$

This correlation was developed for Boiling Water Reactor (BWR), based on experimental results in a 16-rods test section. q_{c} stands for CHF, G for mass flux, and x_{e} for the equilibrium quality. The correlation is for pressure at 6.89 MPa, rod diameter 14.28 mm, rod pitch 3.33 mm, mass flux 678–2441 kg/(m^2·s), and quality 0.073–0.398.

2.2.3.2. CHF Look-up Table

The first CHF LUT was constructed by Doroshchuk[82] in 1975, with 5000 CHF data points. The recent CHF LUT was completed in 2006, developed by Groeneveld et al.[83].

The 2006 CHF LUT is based on more than 30000 data points from experiments for water-cooled uniformly heated circular tubes with upward flow. The CHF q_{c} is provided as a function of pressure, mass flux, and quality. The skeleton of the table covers the pressure range from 0.1 to 21 MPa, mass flux from 0 to 8000 kg/(m^2·s), and quality from -0.5 to 0.9. The 2006 CHF LUT only provides CHF values for tube diameter in 8 mm. Hence, Eq. (2.25) is suggested by Groeneveld et al.[83] to convert from the CHF $q_{\mathrm{c,LUT}}$ in the LUT to the CHF q_{c} in the required tube diameter. Moreover, without reliable scaling method, it fails to apply for non-aqueous fluids.

$$q_{\mathrm{c}} = q_{\mathrm{c,LUT}} \left(\frac{D_{\mathrm{h}}}{0.008} \right)^{-1/2} \tag{2.25}$$

2.2.3.3. Phenomenological Model for CHF

Sublayer Dryout Model for DNB

For subcooled or low-quality condition, theoretical models based on sublayer dryout mechanism are discussed as follows.

(a) Lee and Mudawar model[77]

Lee and Mudawar[77] first proposed the sublayer dryout model for subcooled upward flow boiling based on local condition. Their model assumed that boiling crisis occurs when the loss rate of the liquid sublayer due to evaporation cannot be compensated by gaining liquid from the core region. Thereby, the formula of the critical heat flux q_{c} is shown in Eq.(2.26). U_{B} stands for the velocity of the vapor blanket, ρ_{L} for the liquid density. δ and L_{B} denotes the sublayer thickness and the vapor blanket length. H_{VL} is the evaporation heat, $c_{p,\mathrm{L}}$ the specific heat of liquid sublayer, T_{w} the wall temperature, T_{L} the temperature of the liquid entering the sublayer. Then, the equations of unknown

parameters U_B, δ, L_B, and the liquid subcooling $(T_s - T_L)$ are established by introducing further assumptions.

- The length of the vapor blanket L_B is given by the critical wavelength of Helmholtz instability of the liquid-vapor interface as can be seen from Eq.(2.27), where σ, ρ_V, ρ_L are the surface tension, the density of saturated vapor, and the density of saturated liquid, respectively.
- U_B is determined by considering the force balance in the axial direction, which is a balance determined between the buoyancy force and the drag force.
- The sublayer thickness δ is obtained based on the force balance in the radial direction, between the evaporation force and the lateral force on the vapor blanket.
- Suppposing T_L in the local bulk liquid temperature T_b, the liquid subcooling $(T_s - T_L)$ is therefore approximated as $a_1(T_s - T_b)$, where a_1 is an empirical constant and is recommended to be 0.35.

Additionally, some other empirical correlations, e.g., the vapor diameter D_B, the drag force coefficient C_D, the Karman three-layer velocity distribution formulas[84], and the Dittus-Boelter heat transfer correlation, are also included to enclose the system of equations. In the sublayer dryout model proposed by Lee and Mudawar[77], three constant factors are introduced and determined based on experimental results. Finally, the value of CHF can be obtained through an iterative calculation.

$$q_c = \frac{\rho_L \delta \left[H_{VL} + c_{p,L}(T_s - T_L)\right]}{L_B / U_B} \tag{2.26}$$

$$L_B = \frac{2\pi\sigma(\rho_V + \rho_L)}{\rho_V \rho_L U_B^2} \tag{2.27}$$

(b) Katto model[85]

Katto[85] proposed another sublayer dryout criterion, in which the boiling crisis is presumed to occur when the liquid sublayer is extinguished by evaporation during the passage time of the vapor blanket, written as Eq.(2.28). The sublayer thickness δ is determined by the empirical model for pool boiling CHF. The calculation of vapor blanket length L_B is the same to that of Lee and Mudawar's model[77], which is equal to the critical Helmholtz wavelength (see Eq.(2.27)). The vapor blanket velocity U_B is obtained by introducing an empirical correction coefficient k to the local velocity of the homogeneous two-phase flow. As stated, Katto's model[85] can only be applied for conditions where the local void fraction lower than 70%.

$$q_c = \frac{\rho_L \delta H_{VL}}{L_B / U_B} \tag{2.28}$$

(c) Celata model[86]

Celata et al.[86] developed sublayer dryout model mainly based on Lee and Mudawar's

model[77] and Katto's model[85]. The Eq.(2.28) is applied to give the critical heat flux. The vapor blanket length L_B is also equal to the critical Helmholtz wavelength calculated by Eq.(2.27). The vapor blanket velocity U_B is derived out by considering the force balance in the axial direction between the buoyancy force and the drag force, which is the same as Lee and Mudawar[77], while with different empirical correlations for the vapor diameter D_B and the drag force coefficient C_D. However, Celata et al.[86] assumed that the vapor blanket can only develop and exist in the superheated near-wall region where the local liquid temperature exceeds the saturation temperature. Therefore, the liquid sublayer thickness δ is calculated as the difference between the superheated liquid layer y* and the vapor diameter D_B. As validated by Liu et al.[87], the Celata model shows deficiency in the high-pressure condition.

(d) Liu model[87]

The important update of the sublayer dryout model is proposed by Liu et al.[87] They accepted the Eq.(2.28) as the criterion for the occurrence of the boiling crisis. The Helmholtz instability wavelengths both at the interface between the liquid sublayer and the vapor blanket and the interface between the vapor blanket and the core region are considered. These two Helmholtz wavelengths are supposed to be equal when boiling crisis occurs. Under this assumption, the vapor blanket velocity U_B is obtained with the net vapor generation (NVG) model. The liquid sublayer thickness δ is given with the axial force balance, i.e. the buoyancy and the drag force. As stated by Liu et al.[87], the calculation of the NVG point has an significant effect on the prediction of CHF. The model tends to overestimate the critical heat flux as the pressure is above 17.5 MPa[87].

Dryout Model

As mentioned in Section 2.2.2, for the high-quality condition, boiling crisis occurs when the liquid film in the annular flow is dryout.

Whalley et al.[88] first proposed an annular flow model to predict the dryout point. Then, related researches are continued, by Hewitt and Govan[89], Govan[90], Ahmad [91], etc. A brief review will be given hereunder. The mass balance of the liquid film can be written in Eq.(2.29), where G_{LF} is the liquid film mass flux, z the axial position, D_h the hydraulic diameter of the tube, D the deposition rate, E the entrainment rate, q the heat flux, H_{VL} the evaporation heat. A variety of empirical correlations of the deposition rate D and the droplet entrainment rate E have been proposed by Hewitt and Govan[89], Kataoka et al.[92], Okawa et al.[93], and etc. The term q/H_{VL} denotes the vaporization rate under the assumption that the all supplied heat is used to evaporate the liquid film. Dryout is assumed to occur when G_{LF} reduces to zero. Boundary conditions at the onset of the annular flow are required by the integration of the balance equations, including the location, the initial liquid film mass flux, and fraction of the entrained liquid.

$$\frac{\mathrm{d}G_{\mathrm{LF}}}{\mathrm{d}z} = \frac{4}{D_{\mathrm{h}}}\left(D - E - \frac{q}{H_{\mathrm{VL}}}\right) \tag{2.29}$$

2.2.4. Previous CHF Prediction Methods for High-Pressure Region

Although numerous of CHF prediction methods have been proposed so far, there are rare of them regarding to the high-pressure region, especially for pressure above the working range of PWR (15.5 MPa, reduced pressure at 0.7). Table 2.1 summarizes some CHF prediction methods, of which the validated range covers the range with reduced pressure (P/P_{c}) at least over 0.8. A detailed description of each prediction methods is provided in Appendix A. Particularly, in case the utilization of the CHF correlation requires upstream information, such as inlet subcooling, the distance from the boiling crisis position to the inlet, the correlation will be referred as Upstream Condition Correlation (UCC).

Most correlations in Table 2.1 are developed for water with upward flow in uniformly heated round tubes. Whereas, Kariya correlation[94] is for reduced pressure above 0.961 and developed from experiments of three fluids, including R22, R134a, and water. Vijayarangan[95] developed a CHF correlation from their R134a measurements. Shah[96] correlation includes 23 fluids (water, halocarbon refrigerants, chemicals, liquid metals, helium and other cryogens).

Chen correlation[97], Becker correlation[98], Lombardi correlation[99], Vijayarangan correlation[95], and Shah correlation[96] require known upstream conditions. Particularly, although there is a so-called "local condition correlation" of Shah[96], the distance from the boiling crisis position to the inlet has to be provided. The Becker correlation[98] and Lombardi correlation[99] can only be utilized when the inlet is in subcooled condition. The Hall correlation[79] and Katto's model[100] are for subcooled flow, which implies the critical quality must be negative.

The prediction with these dimensional correlations, such as Levitan correlation[101], Chernobai correlation[102], may bring considerable deviation when be applied to non-aqueous fluids. As described in Section 2.3.2.2, the 2006 CHF LUT[83] is only available for water. Without scaling, it fails to predict the CHF for non-aqueous fluids.

Katto[100] developed a phenomenological model based on sublayer dryout mechanism. It was developed from 647 CHF measurements of subcooled water for pressure range from 0.1 MPa to 20 MPa

Table 2.1.: Previous CHF prediction methods for the High-Pressure region

Model[a]	Reduced pressure	Mass flux, kg/(m^2·s)	Diameter, mm	Critical quality[b]	Remarks
Miropol'skii[103]	0.155	400	4.0	-0.5	Dimensionless
	0.889	10000	8.0	0.8	
Levitan[101]	0.133	750	4.0	0.0	
	0.889	5000	16.0	0.5	
Chernobai[102]	0.227	400	0.4	-1.75	
	0.888	30000	37.0	0.7	
Chen[97]	0.389	1157	8.2	-0.97	UCC
	0.943	3776		0.53	
Becker[98]	0.45	156	10.0	-0.3	UCC,
	0.906	7560		0.6	Subcooled inlet
Hall[79]	0.004	340	0.25	-1.0	Dimensionless,
	0.906	30000	15.0	0.0	Subcooled
Lombardi[99]	0.005	100	0.3	13.0	Dimensionless,
	0.974	9000	37.5	338.0[c]	UCC
2006 CHF LUT[83]	0.004	0	8.0	-0.5	
	0.952	8000		0.9	
Katto[100]	0.004	350	2.5	0.0	Sublayer dryout model
	0.906	40600	11.07	117.5[c]	
Kariya[94],[d]	0.961	400	4.4	N/A	Dimensionless
	0.992	1000			
Vijayarangan[95], [e]	0.24	200	12.7	017	UCC
	0.99	2000		0.94	
Shah[96], [f]	0.0014	3.9	0.315	-2.6	Dimensionless,
	0.96	29051	37.5	1.0	UCC

Notes:

[a] Prediction methods without specific statement are developed for water with upflow in uniformly heated round tubes.

[b] This column is devoted for the range of the critical quality, in case there is no specific statement.

[c] Inlet subcooled temperature.

[d] It contains three fluids, i.e., R22, R134a, and water.

[e] It is for R134.

[f] It includes 23 fluids (water, halocarbon refrigerants, chemicals, liquid metals, helium and other cryogens). Here, the local condition correlation is considered..

2.3. Post-CHF Heat Transfer

2.3.1. General

After the boiling crisis takes place, the post-CHF heat transfer is initiated subsequently. It is also termed as film boiling heat transfer. As mentioned in Section 2.2, the DNB type boiling crisis, associated with subcooled and low-quality condition, leads to the inverted annular flow in the downstream. While for the dryout type boiling crisis related to higher quality, the dispersed droplet flow is encountered after the dryout of the liquid film. Since different flow patterns would result in different heat transfer characteristics, in addition, post-DNB and post-dryout (PDO) are termed and heat transfer of them will be discussed, respectively.

Post-DNB Heat Transfer

Concerning post-DNB, the heat transfer in the inverted annular flow regime is of interest. Since the heated wall is covered by continuous vapor blanket and the liquid core is in the tube center with dispersed vapor bubbles, the following three significant heat transfer processes are taken into account:

(a) Convective heat transfer from the wall to the vapor blanket;

(b) Radiation heat transfer from the wall to the liquid core; and

(c) Heat transfer from vapor blanket to the liquid core at the vapor-liquid interface.

Post-Dryout (PDO) Heat Transfer

As Figure 2.4 (b) shows, after the disappearance of the annular liquid film, in the post-dryout regime, the saturated droplets disperse in the vapor bulk. Among the droplets, the vapor phase and the heating wall, main heat transfer mechanisms are as follows:

(a) Convective heat transfer from the wall to the vapor $q_{\mathrm{c,w-V}}$;

(b) Convective heat transfer from the wall to the droplets $q_{\mathrm{c,w-d}}$;

(c) Heat transfer from the vapor to the droplets at the vapor-liquid interface $q_{\mathrm{c,V-d}}$; and

(d) Radiation heat transfer from the wall to vapor $q_{\mathrm{r,w-V}}$, from the wall to droplets $q_{\mathrm{r,w-d}}$, and from vapor to droplet $q_{\mathrm{r,V-d}}$.

Regarding the portion of the convective heat transfer from the wall to the droplets, it

can only take place immediately after the dryout point. In this region, the wall temperature is not too high, and the droplets could provide relatively effective cooling to the heated wall through direct droplet-wall contact. Accordingly, it is defined as "unstable PDO region" in this thesis. However, as the development of the droplet flow along the flow channel, the direct droplet-wall heat transfer will be neglected due to the higher wall temperature. This region is thereby referred as "stable PDO region".

As has been demonstrated by Parker's experiments[104], under dispersed droplet flow conditions, the vapor superheat could be considerable. In this region, the vapor absorbs heat from the heated surface as well as releasing heat to the droplets through the interfacial heat and mass transfer. The interfacial area and friction depend on droplet size, droplet concentration, distribution of the droplets, droplet velocity, etc. Thus, for PDO heat transfer, one challenge is to determine the thermal non-equilibrium or the vapor superheat in the vapor-droplet system.

2.3.2. Prediction Methods of Post-CHF Heat Transfer

2.3.2.1. Heat Transfer Correlation for Post-CHF Region

Post-DNB Heat Transfer Correlation

To date, the most widely applied prediction methods for inverted annular flow heat transfer in STH codes (e.g., ATHLET[44], RELAP5[105]) are the Bromley correlation[106] and the Berenson correlation[107].

Bromley[106] derived a prediction correlation by considering the balance of buoyancy force and viscous force for the vapor blanket,

$$h = 0.62\left[\frac{\lambda_{\mathrm{V}}^3 g\rho_{\mathrm{V}}(\rho_{\mathrm{L}}-\rho_{\mathrm{V}})\Delta H_{\mathrm{VL}}^*}{\mu_{\mathrm{V}}(T_{\mathrm{W}}-T_{\mathrm{V}})D_{\mathrm{h}}}\right]^{0.25} \tag{2.30}$$

with,

$$\Delta H_{\mathrm{VL}}^* = H_{\mathrm{VL}}\left[1+\frac{0.4c_{p,\mathrm{V}}(T_{\mathrm{W}}-T_{\mathrm{V}})}{\Delta H_{\mathrm{VL}}}\right]^2 \tag{2.31}$$

With respect to the Berenson correlation[107], the Taylor instability at the interface of the vapor blanket is introduced to capture the heat transfer characteristic,

$$h = 0.425\left[\frac{\lambda_{\mathrm{V}}^3 g\rho_{\mathrm{V}}(\rho_{\mathrm{L}}-\rho_{\mathrm{V}})H_{\mathrm{VL}}}{\mu_{\mathrm{V}}(T_{\mathrm{W}}-T_{\mathrm{V}})a}\right]^{0.25} \tag{2.32}$$

where,

$$a = \left[\frac{\sigma}{g(\rho_{\mathrm{L}} - \rho_{\mathrm{V}})}\right]^{0.5} \tag{2.33}$$

In Eqs.(2.30)–(2.33), h denotes the heat transfer coefficient, λ_{V} the vapor thermal conductivety, g the gravitational accelaration, ρ_{V} the vapor density, ρ_{L} the liquid density, μ_{V} the vapor viscosity, T_{W} the wall remperature, T_{V} the vapor temperature, D_{h} the hydraulic diameter, H_{VL} the evaporation heat, $c_{p,\mathrm{V}}$ the vapor specific heat, σ the surface tension.

PDO Heat Transfer Correlation

As mentioned in the previous section, it is hard to capture the vapor superheat in the PDO region. Therefore, a great number of PDO heat transfer correlations using saturation temperature as vapor temperature has been proposed[74, 108, 109]. The most common ones are the Modified Dougall-Rohsenow correlation[110], the Groeneveld correlation[111], and the Condie-Bengston IV correlation[112].

Modified Dougall-Rohsenow correlation[110] comprises the Dittus-Boelter equation and a temperature ratio,

$$h = 0.023\frac{\lambda_{\mathrm{V}}}{D_{\mathrm{h}}}Re_{\mathrm{V}}^{0.8}Pr_{\mathrm{V}}^{0.4}\left(\frac{T_{\mathrm{V}}}{T_{\mathrm{W}}}\right)^{0.5} \tag{2.34}$$

in which the vapor temperature T_{V} and the wall temperature T_{W} are in the unit of Kelvin.

Groeneveld[111] derived a correlation from experiments in heated tube and annuli based on the Y factor utilized by Miropol'skii[113],

$$h = 0.00327\frac{\lambda_{\mathrm{V}}}{D_{\mathrm{h}}}\left[\frac{GD_{\mathrm{h}}}{\mu_{\mathrm{V}}}\left(x_{\mathrm{e}} + \frac{\rho_{\mathrm{V}}}{\rho_{\mathrm{L}}}(1 - x_{\mathrm{e}})\right)\right]^{0.901} Pr_{\mathrm{w}}^{1.32}Y \tag{2.35}$$

with,

$$Y = \left[1 - 0.1\left(\frac{\rho_{\mathrm{L}}}{\rho_{\mathrm{V}}} - 1\right)^{0.4}(1 - x_{\mathrm{e}})^{0.4}\right]^{-1.5} \tag{2.36}$$

Condie-Bengston IV correlation[112] is developed from rod bundles experiments,

$$h = 0.05345\lambda_V^a \cdot Pr_{\mathrm{w}}^b \cdot Re_{\mathrm{V}}^{\mathrm{c}} \cdot D^d \cdot (x_{\mathrm{e}} + 1)^f \tag{2.37}$$

with $a = 0.4593$, $b = 2.2598$, $c = 0.6249 + 0.2043\ln(x_{\mathrm{e}} + 1)$, $d = -0.8095$, $f = -2.0514$.

In Eqs.(2.34)–(2.37), $Re_{\mathrm{V}} = GD_{\mathrm{h}}/\mu_{\mathrm{V}}$ denotes the Reynolds number. $Pr_{\mathrm{V}} = \mu_{\mathrm{V}}c_{p,\mathrm{V}}/\lambda_{\mathrm{V}}$ and $Pr_{\mathrm{w}} = \mu_{\mathrm{w}}c_{p,\mathrm{w}}/\lambda_{\mathrm{w}}$ are devoted for the Prandtl number with vapor properties at saturation temperature and wall temperature, respectively. h is the heat transfer

coefficient. λ_V, μ_V, $c_{p,V}$, and ρ_V are the thermal conductivity, the dynamic viscosity, the specific heat, and the density of saturated vapor, respectively. Properties subscripted with 'w' are evaluated at wall temperature. ρ_L is for the saturated liquid density, x_e for the equilibrium quality.

There are also correlations with a calculated actual vapor temperature. Referring to review work by Yu[114], the most widely discussed correlations are from Groeneveld et al.[115] (GRO), Chen et al.[116] (CSO), and Varone and Rohsenow[117] (LCS). For the LCS model, the droplet diameter and the quality at the dryout point are required and empirical correlations for these parameters are therefore supposed to be introduced, which makes the LCS model dependent on dryout parameters and more complicated. Therefore, hereunder, GRO and CSO model will be introduced.

(a) Groeneveld et al.[115] (GRO) correlation

According to the research of Groeneveld et al.[115], the axial variation of the wall temperature, vapor temperature, and the actual quality x_a is illustrated in Figure 2.7. It is assumed that at the dryout point (x_{DO}) the vapor phase is in saturation temperature and the quality of the vapor-droplet system equals to the equilibrium quality x_e, while in the downstream the vapor becomes superheated and x_a is lower than x_e.

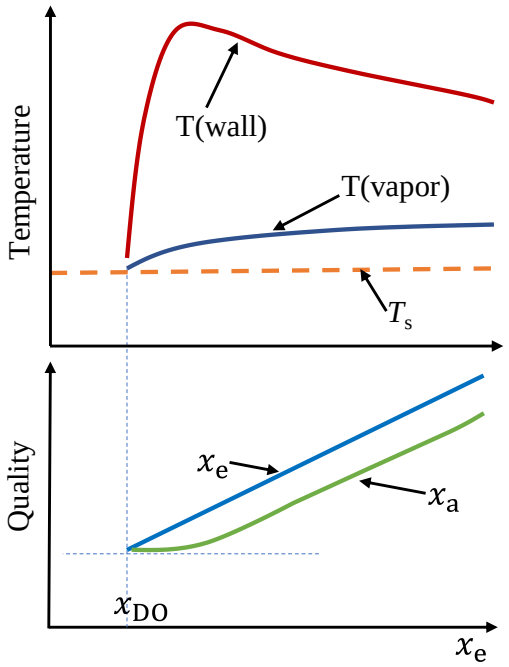

Figure 2.7.: Schematic of temperature and quality in the PDO region[115]

Groeneveld's PDO heat transfer correlation[115] is proposed from 1402 PDO experimental data points for water over a range of pressure 0.69–21.5 MPa, mass flux 130–5200 kg/(m^2·s), heat flux 30–2100 kW/m^2, tube diameter 2.54–12.8 mm, and quality -0.12–3.09. The calcualted actucal vapor enthalpy $H_{V,a}$ is expressed by an empirical correlation as,

$$\frac{H_{\mathrm{V,a}} - H_{\mathrm{V,e}}}{H_{\mathrm{VL}}} = \exp(-\tan\psi)\exp[-(3\alpha)^{-4}] \tag{2.38}$$

Here, $H_{\mathrm{V,e}}$ the equilibrium vapor enthalpy, H_{VL} the evaporation heat. ψ is the non-equlibrium parameter ($0 \le \psi < \pi/2$), evaluated by,

$$\psi = 0.13864 Pr_{\mathrm{V}}^{0.2031} \left(\frac{G D_{\mathrm{h}} x_{\mathrm{m}}}{\mu_{\mathrm{V}} \alpha}\right)^{0.20006} \left(\frac{q D_{\mathrm{h}} c_{p,\mathrm{V}}}{\lambda_{\mathrm{V}} H_{\mathrm{VL}}}\right)^{-0.09232} \cdot (1.3072 - 1.0833 x_{\mathrm{e}} + 0.8455 x_{\mathrm{e}}^2) \tag{2.39}$$

where, Pr_{V} denotes the Prandtl number at equlibrium temperature, G the mass flux, D_{h} the tube diameter, q the heat flux, x_{e} the equilibrium quality. μ_{V}, $c_{p,\mathrm{V}}$, and λ_{V} are devoted for the dynamic viscosity, the specific heat, and the thermal conductivity of vapor at equilibruim temperature, respectively. x_{m} is devoted for the mass quality, computed by,

$$\begin{cases} x_{\mathrm{m}} = 0, x_{\mathrm{e}} < 0 \\ x_{\mathrm{m}} = x_{\mathrm{e}}, 0 \le x_{\mathrm{e}} \le 1 \\ x_{\mathrm{m}} = 1, x_{\mathrm{e}} > 1 \end{cases} \tag{2.40}$$

α is the void fraction, defined by,

$$\alpha = \frac{x_{\mathrm{m}}}{x_{\mathrm{m}} + \frac{\rho_{\mathrm{V}}}{\rho_{\mathrm{L}}}(1 - x_{\mathrm{m}})} \tag{2.41}$$

where, ρ_{V} and ρ_{L} stand for saturated vapor density and saturated liquid density, respectively.

Accordingly, deriving from the heat balance, the actual quality x_{a} is given by,

$$x_{\mathrm{a}} = \frac{H_{\mathrm{VL}}}{H_{\mathrm{V,a}} - H_{\mathrm{L}}} x_{\mathrm{e}} \tag{2.42}$$

Consequently, as suggested, the Hadaller correlation[115] is applied to calculate the heat transfer coefficient with the calculated actual quality x_{a},

$$h = 0.008348 \frac{\lambda_{\mathrm{f}}}{D_{\mathrm{h}}} \left[\frac{G D_{\mathrm{h}}}{\mu_{\mathrm{f}}} \left(x_{\mathrm{a}} + \frac{\rho_{\mathrm{V}}}{\rho_{\mathrm{L}}}(1 - x_{\mathrm{a}})\right)\right]^{0.8774} Pr_{\mathrm{f}}^{0.6112} \tag{2.43}$$

In Eq.(2.43), h is the heat trasnfer coefficient. λ_{f}, μ_{f}, and Pr_{f} denote the thermal conductively, the dynamic viscosity, and the Prandtl number at the vapor film tempearture $T_{\mathrm{f}} = (T_{\mathrm{w}} + T_{\mathrm{s}})/2$, respectively.

(b) Chen et al.[116] (CSO) correlation

The quality ratio $x_{\mathrm{a}}/x_{\mathrm{e}}$ is expressed as a function of the dimensionless tempearuete and the reduced pressure,

$$\frac{x_\mathrm{a}}{x_\mathrm{e}} = 1 - B(P) \cdot \frac{T_\mathrm{V,a} - T_\mathrm{s}}{T_\mathrm{w} - T_\mathrm{V,a}} \tag{2.44}$$

where x_a is for the actual quality, x_e for the equilibrium quality, $T_\mathrm{V,a}$ for the actual vapor temperature, T_s for the saturation temperature, T_w for the wall temperature with $T_\mathrm{s} \leq T_\mathrm{V,a} \leq T_\mathrm{w}$ and $0 \leq x_\mathrm{a}/x_\mathrm{e} \leq 1$. $B(P)$ is an emperical correlation,

$$B(P) = \frac{0.26}{1.15 - (P/P_\mathrm{c})^{0.65}} \tag{2.45}$$

here P and P_c are the system pressure and the critical pressure, respectively.

By solving the heat balance correlation Eq.(2.42) and the Eq.(2.44), the $T_\mathrm{V,a}$ is obtained. Then, the heat transfer coefficient h will be given by modified Colburn modification of Reynolds analogy, with an appropriate two-phase friction factor f.

$$h = G x_\mathrm{a} c_{p,\mathrm{f}} Pr_\mathrm{f}^{-2/3} \frac{f}{2} \tag{2.46}$$

Concerning the friction factor f, the Beattie's implicit friction correlation, which is developed for the dispersed droplet flow, is recommend,

$$f = 0.037 \left[\frac{G D_\mathrm{h}}{\mu_\mathrm{V,a}} \left(x_\mathrm{a} + \frac{\rho_\mathrm{V}}{\rho_\mathrm{L}} (1 - x_\mathrm{a}) \right) \right]^{-0.17} \tag{2.47}$$

with G the mass flux, D_h the tube diameter. $c_{p,\mathrm{f}}$ and Pr_f denote the specific heat and the Prandtl number at the vapor film tempearture $T_\mathrm{f} = (T_\mathrm{w} + T_\mathrm{s})/2$, respectively. ρ_V and ρ_L are devoted for the saturated vapor density and saturated liquid density.

The CSO model is derivated from 2854 data points of water experriemtns at the range of pressure 0.4–19.5 MPa, mass flux 16.5–3031.8 kg/(m^2·s), heat flux 33.7–1651.7 kW/m^2, and quality 0.502–1.728. Particularly, it has to be noted that the CSO model is invalid for reduced pressure lower than 0.883, corresponding to 19.5 MPa for water, since it may produce an unreasonable $T_\mathrm{V,a}$.

As seen, these correlations with calucalated actual vapor temperature are usually more complicated, whereas still emperical corrlations.

2.3.2.2. Post-CHF Heat Transfer Look-up Table

The latest Post-CHF LUT proposed by Groeneveld et al.[118] in 2003 (2003 Post-CHF LUT) on the basic of the PDO-LW-96 look-up table[119], is developed from 20785 experimental data points for water flow in uniformly heated vertical tubes. The heat transfer coefficient $h_\mathrm{c,LUT}$ is given as a function of the pressure P, mass flux G, quality x_e, and the wall superheat $\Delta T_\mathrm{w} = T_\mathrm{w} - T_\mathrm{s}$. The 2003 Post-CHF LUT could be applied to calculate the heat transfer coefficient of both the inverted annular region and the

dispersed droplet flow region. As mentioned, it contains both the post-DNB and PDO heat transfer measurements. The table skeleton covers the pressure range 0.1–20 MPa, mass flux 0–7000 kg/ (m^2·s), quality -0.2–2.0, and wall superheat 50–1200 ℃. Since the 2003 Post-CHF LUT is normalized to tube diameter at 8 mm, the predicted heat transfer coefficient h_c will be given by,

$$h_c = h_{c,LUT}\left(\frac{D_h}{0.008}\right)^{-0.2} \tag{2.48}$$

Additionally, the same to SC LUT and CHF LUT, it is incapable of giving prediction for non-aqueous coolant without reasonable scaling approaches.

2.3.2.3. Phenomenological Model for Post-CHF Heat Transfer

Phenomenological Model for Post-DNB Heat Transfer

Some thermal hydraulic models using two-fluid model have been proposed to simulate the inverted annular flow heat transfer, e.g., Cachard[120], Seok and Chang[121], Hammouda et al.[122], Nakla[123], Liu[124]. These theoretical models, generally, contain the following relations,

- Mass, momentum, and energy conservation equations for the liquid core and vapor blanket;
- Constitutive equations, normally including wall heat transfer, interfacial heat transfer, wall friction, interfacial friction, etc.; and
- Initial and boundary conditions, such as the temperature and mass flow rate of the liquid core and vapor at the DNB point.

These models usually have the same conservation equations but different combination of constitutive equations. Owing to deficiency in knowledge about the vapor blanket thickness, velocity distribution, etc., these models are normally based on simplifying assumptions and empirical correlations. Thereby, a lot of adjustable parameters are introduced. As demonstrated by Hammouda et al.[122], predictive capability of semi-empirical theoretical models are often worse than empirical correlations, since constitutive equations with empirical parameters are valid only for a limited range of flow conditions.

Phenomenological Model for Post-Dryout Heat Transfer

PDO heat transfer models are based on two-fluid models as well. Guo and Mishima[125] considered six possible heat transfer processes among the heated wall, vapor, and droplets in detail, i.e., $q_{c,w-v}$, $q_{c,w-d}$, $q_{c,v-d}$, $q_{r,w-v}$, $q_{r,w-d}$, and $q_{r,v-d}$. Related parameters are assumed as a function of the axial position. The interfacial vapor-droplet heat transfer is calculated by the Lee-Ryley correlation[126],

$$Nu_{c,v-d} = 2 + 0.74 Re_d^{0.5} Pr_v^{0.333} \tag{2.49}$$

Where, $Re_{\mathrm{d}} = (U_{\mathrm{V}} - U_{\mathrm{d}})\rho_{\mathrm{V}} D_{\mathrm{d}}/\mu_{\mathrm{V}}$ is the droplet Reynolds number, with U_{V} the vapor phase velocity, U_{d} the droplet velocity, ρ_{V} the saturated vapor density, D_{d} the droplet diameter, μ_{V} the saturated vapor viscosity. As stated, the phenomenological model from Guo and Mishima[125] was successfully applied to predict the wall temperature and vapor superheat for the pressure range of 0.2–0.6 MPa.

Saha[127] proposed a one-dimensional heat transfer model for the PDO regime by solving the mixture energy equation with the mass rate correlation of vapor generation. In Saha's simulation, the direct wall-droplet heat transfer $q_{\mathrm{c,w-d}}$ and radiation heat transfer are neglected. The effectiveness of vapor-droplet heat trasnfer is correlated by,

$$K_1 = 6300\left(1 - \frac{P}{P_{\mathrm{c}}}\right)^2 \left[\left(\frac{G x_{\mathrm{a}}}{\alpha}\right)^2 \frac{D_{\mathrm{h}}}{\rho_{\mathrm{V}}\sigma}\right]^{0.5} \tag{2.50}$$

with P for system pressure, P_{c} for critical pressure, G for mass flux, x_{a} for the calculated quality, α for the void fraction, D_{h} for tube diameter, ρ_{V} for saturated vapor density, and σ for surface tension, respectively. Accordingly, mass rate of vapor generation could be computed as,

$$\Gamma_{\mathrm{V}} = K_1 \frac{\lambda_{\mathrm{V}}(1-\alpha)(T_{\mathrm{V}} - T_{\mathrm{s}})}{D_{\mathrm{h}}^2 H_{\mathrm{VL}}} \tag{2.51}$$

here T_{V} and T_{s} denote vapor temperature and saturation temperature, respectively. λ_{V} is the thermal conductivity of vapor. H_{VL} is the evaporation heat. It has been demonstrated by Saha[127] that the validity of his PDO heat tranfer model covers the pressure range from 2.9 MPa to 12 MPa.

Recently, Cheng et al.[128] developed a mechanistic prediction model for PDO heat transfer, with considertation of three convective heat trasnfer, i.e., $q_{\mathrm{c,w-V}}$, $q_{\mathrm{c,w-d}}$, $q_{\mathrm{c,V-d}}$. The mass flux of droplets evaporated in the heated wall is associated to a normal distribution function of the wall temperature and the Leidenfrost temperature. It is indicated that the prediction results get well agreement with the PDO heat transfer experiment of Becker[129].

2.3.3. Previous Post-CHF Heat Transfer Prediction Methods for High-Pressure Region

As reviewed by Hammouda[130], Nakla et al.[131], Groeneveld[132], and etc., due to the high CHF value, the large temperature rise in the inverted annular regime would lead to the burnout of the heated surface easily. Thereby, it is nearly impossible to perform related heat transfer experiments with a heat-flux controlled water-steam system. The invention of the "hot-patch" technique makes it feasible to obtain inverted annular flow heat transfer measurements. However, as a result of the complicated experiment design, the range of available experiments is very limited so far[132]. Hence, research about post-DNB heat transfer in inverted annular flow regime is not as common as PDO. As a

result, research in this region has focused more on avoiding the occurrence of boiling crisis. As reviewed by Nakla et al.[131] and Liu et al.[133],existing measurement with water for inverted annular heat transfer is only up to 9 MPa (reduced pressure at 0.4), from experiment performed by Stewart and Groeneveld[134]. Even though taking scaling fluids (e.g. R12, R134a) into consideration, the maximum pressure is 2.39 MPa with R134a (13 MPa for water at the same reduced pressure 0.59) from experiment carried out by Nakla[131]. Due to short of experiments, a prediction approach for the high-pressure post-DNB heat transfer is missing. Thereby, further discussion about post-DNB heat transfer in the high-pressure region could not be carried out.

Concerning post-dryout heat transfer, some prediction approaches with reduced pressure above 0.8 for water in uniformly heated tubes are collected and summarized in Table 2.2. Except prediction methods mentioned above, details of these correlations can be found in the Appendix D. As seen, the valid pressure of the Miropol'skii correlation[113] is the highest, up to 22 MPa. In the following sections, the predictive capability of these post-dryout heat transfer approaches will be assessed.

Table 2.2.: Previous PDO heat transfer prediction methods for the High-Pressure region

Model	Pressure, MPa	Mass flux, kg/(m^2·s)	Diameter, mm	Critical quality
2003 Post-CHF LUT[118]	0.1	0	0.8	-0.2
	20	7000	0.8	2.0
Miropol'skii[113]	4	700	4.0	0.4
	22	2000	8.0	1.0
Slaughterbeck[135]	6.8	1050	13.4	0.0
	20	5300	17.0	1.0
Groeneveld[111]	3.4	700	1.5	0.1
	21.5	5300	25.0	0.9
Swenson[136]	20.68	949.4	10.4	0.080
	20.68	1356.2	10.4	0.980

2.4. Summary

In this chapter, heat transfer characteristics at supercritical and subcritical pressures are discussed.

- Heat transfer at supercritical condition

Supercritical fluids are single-phase. However, drastic property variation near the pseudo-critical region may lead to different heat transfer characteristics compared to conventional conditions. Especially, at supercritical pressures, the heat transfer deterioration (HTD) phenomenon has to be considered. As concluded, it fails to compute the heat transfer coefficient with a phenomenological model so far. The SC

LUTs is limited within the range of the table skeleton and can only be applied for water without scaling. According to recent literatures, the Cheng correlation, i.e., Eq.(2.15), which is a dimensionless one derived from a large databank and covers also HTD conditions, is recommended.

- Critical heat flux and post-CHF heat transfer

The mechanism about DNB and dryout is introduced, respectively. For subcooled or low-quality conditions, the sublayer dryout model is commonly applied to explain the DNB. While for high-quality conditions, dryout occurs as the liquid film of the annular flow disappears. After that, post-CHF heat transfer region is encountered. Numerous of prediction methods for CHF and post-CHF heat transfer have been established for various working conditions, including correlations, look-up tables, and phenomenological models. Prediction methods with reduced pressure over 0.8 are collected from open literatures. It is found that only a few of existing prediction methods are suitable for the high-pressure region. It is noted that for post-DNB heat transfer, previous experiments with water as coolant covers reduced pressure up to 0.4. Although considering non-aqueous fluids, the maximum reduced pressure is 0.59 for experiments with R134a. Hence, to date, post-DNB heat transfer experiments with reduced pressure above 0.7 do not exist. The present work therefore will pay attention to CHF and post-dryout heat transfer.

In the following chapters, new experiment databank for the high-pressure region will be established, for CHF and post-CHF heat transfer, respectively. Predictive capability of these previous prediction methods will be examined. If necessary, new prediction models will be developed. In the end, the most suitable prediction method for the high-pressure region will be determined.

3. Modelling of Critical Heat Flux

This chapter will discuss the modelling of critical heat flux. A high-pressure CHF experiment databank with reduced pressure above 0.7 is compiled and established firstly. Thereby, existing CHF prediction models could get assessed on the basic of high-pressure CHF experiments.

3.1. CHF Databank

CHF test data from different experiments with upward flow in uniformly heated circular tubes is collected from open literatures and experiments carried out in the Institute for Applied Thermofluidics (IATF)[137]. Currently, experiments with water, R12, or CO_2 as coolant are obtained. For each data points, it contains the information of system pressure P, mass flux G, tube diameter D_h, critical quality x_c (equilibrium quality at the CHF location), critical heat flux q_c, inlet quality x_in, and the distance from the start of heated section to the boiling crisis point L_c. Among them, P, G, D_h, x_c, and q_c are always available, while x_in or L_c might be missing. Further, to guarantee the reliability of the databank, assessment work is carried out, including heat balance verification, duplication screening, and reproducibility check. Detail about the reliability check and parameter distribution of the new CHF databank will be described in the following.

3.1.1.1. Heat Balance Verification

Concerning CHF experiments, the test is usually carried out with fixed inlet subcooling, while the supplied power is increased step by step until boiling crisis occurs. For every recorded data point, heat balance verification would be carried out by calculating the enthalpy rise based on Eq.(3.1), in which x_in denotes the inlet quality, q_c the heat flux, L_c the distance between the start of the heated section and the location of the boiling crisis, G the mass flux, D_h the tube diameter, and H_VL the evaporation heat. In Eq.(3.1), the LHS denotes the enthalpy rise given by the data bank, while the RHS is the calculated enthalpy rise. When x_in or L_c in Eq.(3.1) is unknown, it fails to evaluate the heat balance and such data points will be accepted directly. In case the deviation of the given value and the calculated value of the enthalpy rise exceeds 10%, it implies

that the recorded data point cannot satisfy the heat balance check and it will be removed from the data bank. In the end, 2734 data points are reserved.

$$(x_{\mathrm{c}} - x_{\mathrm{in}}) \cdot H_{\mathrm{VL}} = \frac{4 q_{\mathrm{c}} L_{\mathrm{c}}}{G D_{\mathrm{h}}} \tag{3.1}$$

3.1.1.2. Duplication Screening

Since the experimental data points are collected from different literatures and the same experimental results might be reported repeatedly, the duplication problem could not be avoided. Thereby, the criterion given by Eq.(3.2) is applied to discard duplicated data points. Compared to the reference data point $\boldsymbol{i}(P_i, G_i, D_{\mathrm{h},i}, x_{\mathrm{c},i}, q_{\mathrm{c},i})$, if there is another data point $\boldsymbol{j}(P_j, G_j, D_{\mathrm{h},j}, x_{\mathrm{c},j}, q_{\mathrm{c},j})$, which has the same working fluids but from different data sources to the point $\boldsymbol{i}$, fulfills all the five inequations in Eq.(3.2), the tested data point $\boldsymbol{j}$ will be identified as a redundant record and will be removed. After duplication check, 45 data points are screened out.

$$\begin{cases} \left|P_i - P_j\right| < 0.01 \text{ bar} \\ \left|G_i - G_j\right| < 0.01 \text{ kg/(m}^2 \cdot \text{s)} \\ \left|D_{\mathrm{h},i} - D_{\mathrm{h},j}\right| < 0.01 \text{ mm} \\ \left|x_{\mathrm{c},i} - x_{\mathrm{c},j}\right| < 0.01 \\ \left|q_{\mathrm{c},i} - q_{\mathrm{c},j}\right| < 0.01 \text{ kW/m}^2 \end{cases} \tag{3.2}$$

3.1.1.3. Reproducibility Check

Due to unstable flow conditions (mass flux or system pressure fluctuation), the entrance effect, or other experiment uncertainties, there may exist deviation among different test records[52]. Thereby, it is necessary to assess the reproducibility of each data point and exclude unreliable data points.

Firstly, adjacent data points for each data point are identified. The distance r_{ij} between the reference data point $\boldsymbol{i}$ ($P_i, G_i, D_{\mathrm{h},i}, x_{\mathrm{c},i}, q_{\mathrm{c},i}$) and the tested data point $\boldsymbol{j}(P_j, G_j, D_{\mathrm{h},j}, x_{\mathrm{c},j}, q_{\mathrm{c},j})$ is defined by,

$$r_{ij}^2 = \Delta P_{ij}^2 + \Delta G_{ij}^2 + \Delta D_{\mathrm{h},ij}^2 + \Delta x_{\mathrm{c},ij}^2 \tag{3.3}$$

where, the $\Delta P_{ij} = \left|\frac{P_i - P_j}{P_i}\right|$, $\Delta G_{ij} = \left|\frac{G_i - G_j}{G_i}\right|$, $\Delta D_{\mathrm{h},ij} = \left|\frac{D_{\mathrm{h},i} - D_{\mathrm{h},j}}{D_{\mathrm{h},i}}\right|$, and $\Delta x_{\mathrm{c},ij} = \left|\frac{x_{\mathrm{c},i} - x_{\mathrm{c},j}}{x_{\mathrm{c},i}}\right|$. Referring to the uncertainty analysis of CHF experiments by Cheng et al.[138], the relative deviation of CHF experiment is around 7%. Thereby, the threshold of the distance r_{ij} is assigned the value 0.1, which implies that the tested data point $\boldsymbol{j}$ with r_{ij} lower than 0.1 will be regarded as an adjacent point to the reference point $\boldsymbol{i}$. Consequently, each data point would have k ($k \geq 0$) different adjacent points. In case

there is no adjacent point to the reference point $\boldsymbol{i}$, when k is equal to zero, it will be accepted directly, and the following steps will be skipped. In this step, 1880 data points have at least one adjacent points.

Secondly, the critical heat flux of the tested point is normalized to the reference point. For the adjacent data point group to the reference point, suppose that the distribution of parameters (pressure, mass flux, tube diameter, and critical quality) follows the normal distribution. Accordingly, weighting factors are introduced for each variable of the adjacent data point. Taking the weighting factor $w_{j,P}$ of pressure as an example, the $w_{j,P}$ is defined by Eq.(3.4), supposing the mean value of the normal distribution is equal to the pressure of the reference point P_i, and the standard deviation σ_{P_i} is $0.1 \cdot P_i$. Likewise, the weighting factors of mass flux, tube diameter, and the critical quality can be calculated and referred as $w_{j,G}$, w_{j,D_h}, and w_{j,x_c}, respectively. Hence, the integral weighting factor w_j of the tested point $\boldsymbol{j}$ would be calculated by Eq.(3.5). Then, the weighted mean value $\bar{q}_{\mathrm{c},i}$ and the weighted deviation σ_i^2 of the critical heat flux are given by Eq.(3.6) and Eq.(3.7), which considered each tested data point in the adjacent group.

$$w_{j,P} = \frac{1}{\sqrt{2\pi\sigma_{P_i}^2}} \exp\left(-\frac{\left(P_j - P_i\right)^2}{2\sigma_{P_i}^2}\right) \tag{3.4}$$

$$w_j = w_{j,P} \cdot w_{j,G} \cdot w_{j,D_\mathrm{h}} \cdot w_{j,x_\mathrm{c}} \tag{3.5}$$

$$\bar{q}_{\mathrm{c},i} = \frac{\sum_{j=1}^{k+1} w_j q_{\mathrm{c},j}}{\sum_{j=1}^{k} w_j} \tag{3.6}$$

$$\sigma_i^2 = \frac{\sum_{j=1}^{k+1} w_j \left(q_{\mathrm{c},j} - \bar{q}_{\mathrm{c},i}\right)^2}{\sum_{j=1}^{k+1} w_j} \tag{3.7}$$

Finally, Chauvenet's statistical criterion[139] is implemented to identify unreliable data points. The Eq.(3.8) is utilized to calculate the standardized deviation τ between the weighted mean critical heat flux $\bar{q}_{\mathrm{c},i}$ and the reference data point $q_{c,i}$. Then, compare the standardized deviation τ with the corresponding $T(k+1)$ in the table of Chauvenet's criterion[139] (see Appendix B). If the standardized deviation τ is above $T(k+1)$, it implies that the deviation of the adjacent data group for the reference point $\boldsymbol{i}$ is not acceptable and the reference point $\boldsymbol{i}$ will thereby be discarded, otherwise the reference point $\boldsymbol{i}$ will be accepted. 37 data points that cannot satisfy this criterion are removed.

$$\tau = \left|\frac{q_{c,i} - \bar{q}_{\mathrm{c},i}}{\sigma_i}\right| \tag{3.8}$$

3.1.1.4. Distribution of High-Pressure Water CHF Databank

Table 3.1 summarized the ranges of parameters for the high-pressure CHF databank with water as coolant. It contains 1484 data points in total. The pressure could reach up to 21.5 MPa, corresponding reduced pressure P_r up to 0.97. The mass flux ranges from 156 to 6907 kg/(m^2·s), tube diameter from 1.9 to 24.7 mm, the quality from -1.768 to 0.955. Additionally, Appendix C provides the detailed information about each data source and variable range for every data source.

Table 3.1.: Experimental data of CHF with high-pressure water

Parameters	P [MPa]	P_r [-]	G [kg/(m^2·s)]	D_h [m]	x_c [-]	q_c [kW/m^2]
min	15.5	0.7	156	0.0019	-1.768	135
max	21.5	0.97	6907	0.0247	0.955	7770

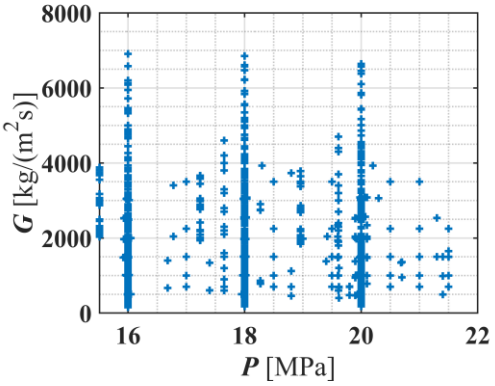

(a) Mass flux vs pressure

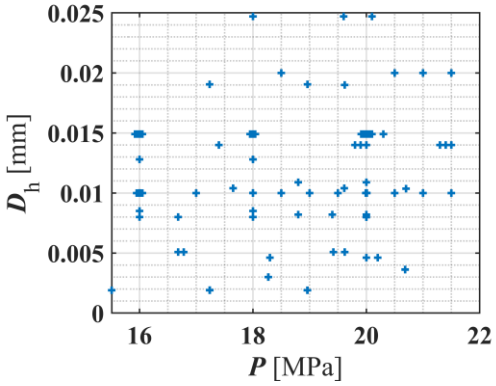

(b) Diameter vs pressure

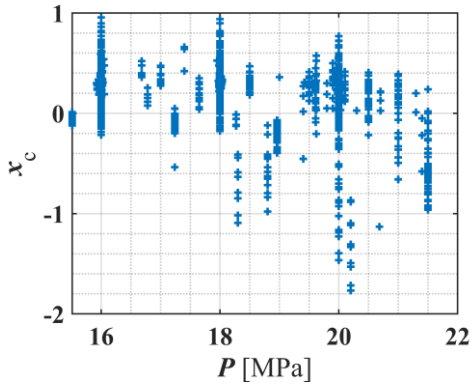

(c) Critical quality vs pressure

Figure 3.1.: Distribution of CHF data points

The data coverage on mass flux, tube diameter, and critical quality versus pressure are

shown in Figure 3.1. In general, they are evenly distributed versus pressure.

3.2. Assessment of Previous CHF Prediction Method

To assess the capability of CHF prediction models, the calculated results are compared with the experimental data collected in the current high-pressure water CHF databank (as described in Table 3.1). For each data point, the error parameter is defined by,

$$\varepsilon_i = \frac{q_{\mathrm{c,cal}}(i) - q_{\mathrm{c,m}}(i)}{q_{\mathrm{c,m}}(i)} \tag{3.9}$$

where $q_{\mathrm{c,cal}}(i)$ is the value of critical heat flux calculated by correlations and $q_{\mathrm{c,m}}(i)$ is the measured value. Moreover, the mean value (*ME*), standard deviation (*SD*), and root-mean-square value (*RMS*) of the error parameter are calculated by Eq.(3.10), Eq.(3.11), and Eq.(3.12), respectively, where N denotes the number of CHF data points.

$$ME = \frac{1}{N}\sum_{i=1}^{N} \varepsilon_i \tag{3.10}$$

$$SD = \sqrt{\frac{1}{N}\sum_{i=1}^{N}(\varepsilon_i - ME)^2} \tag{3.11}$$

$$RMS = \sqrt{\frac{1}{N}\sum_{i=1}^{N} \varepsilon_i^2} \tag{3.12}$$

Table 3.2.: Predictive capability of previous correlations for the high-pressure water CHF databank

Model	No. of data used	*ME*	*SD*	*RMS*
Miropol'skii[103]	1484	-0.233	0.453	0.510
Levitan[101]	1484	0.548	3.178	3.223
Chernobai[102]	1484	0.958	1.835	2.069
Chen[97]	1254	-0.380	0.595	0.706
Becker[98]	1188	-0.952	0.019	0.953
Hall[79]	414	0.133	0.403	0.424
Lombardi[99]	1188	-0.125	0.872	0.881
2006 CHF LUT[83]	1387	0.116	0.524	0.537
Katto[100]	414	0.225	0.864	0.891
Kariya[94]	1484	0.148	0.949	0.960
Vijayarangan[95]	1316	-0.593	0.527	0.793
Shah[96]	1316	1.181	1.640	2.020

Accordingly, Table 3.2 exhibits the prediction accuracy of different correlations against the water CHF database. Levitan correlation[101], Chernobai correlation[102], Becker

correlation[98], Vijayarangan correlation[95], and Shah correlation[96] give the mean error exceeding ± 50%. Although the Hall correlation[79] and Katto's sublayer dryout model[100] can only be applied for 414 subcooled measurements, the RMS error of them is still up to 42.4% and 89.1%, respectively. Specifically, the 2006 CHF LUT[83], which covers a relative wide range than other correlations, achieves mean error of 11.6% and RMS error of 53.7%. In addition, it fails to calculate cases beyond the scope of the 2006 CHF LUT[83].

As can be seen, the calculation accuracy of existing prediction methods is insufficient when compared to high-pressure CHF test data. Hence, it requires a new CHF model for the high-pressure region.

3.3. Development of CHF model

As mentioned, it is desirable to develop a new CHF prediction method for the high-pressure conditions with reduced pressure over 0.7. As the new correlation will be implemented to safety analysis code for power cycle systems, it is expected to be,

- Dimensionless correlation

A physical equation is supposed to be dimension homogeneity, i.e., the combination of variables in both sides of the equation should have consistent dimensions. Otherwise, it does not reflect the physics. Only the dimensionless correlations are considered suitable for various working fluids.

- Local-condition-based correlation

A local-condition-based correlation is not dependent on the upstream history. Hence, it is more convenient to be applied[74].

- Easily implemented to STH code

To meet the research objective of the present work, the new CHF model will be implemented to STH code.

3.3.1. Identification of Dimensionless Parameter

As discussed in Section 2.2, the boiling crisis mechanisms depend on the upstream flow regimes. The DNB type boiling crisis occurs under subcooled or low-quality condition with the upstream in inverted annular flow, while dryout occurs in higher quality where the upstream is annular flow. Thereby, the work to identify key dimensionless parameters is carried out for DNB and dryout, respectively.

3.3.1.1. DNB

As can be seen from Figure 2.5, the boiling crisis occurs when the liquid sublayer is dryout. In this section, significant equations in the sublayer dryout model are re-

organized to identify the key dimensionless parameters.

For the heat balance equation, Katto's assumption[85] is accepted. CHF is equal to the minimum heat flux in which the liquid sublayer could be extinguished by evaporation during the passage time of the liquid blanket. Therefore, the heat balance equation can be written as,

$$q_{\mathrm{c}}=\frac{\rho_{\mathrm{L}}\delta H_{\mathrm{VL}}}{L_{\mathrm{B}}/U_{\mathrm{B}}} \tag{3.13}$$

in which the CHF is a function of the saturated liquid density ρ_{L}, the liquid sublayer thickness δ, the evaporation heat H_{VL}, the vapor blanket length L_{B}, and the vapor blanket velocity U_{B}. Derivation of these unknown parameters is discussed hereunder.

Concerning the force balance of the vapor blanket in the axial direction, it is determined between the drag force and buoyancy force,

$$\frac{1}{2}\rho_{\mathrm{L}}C_{\mathrm{D}}(U_{\mathrm{B}}-U_{\mathrm{BL}})^2\frac{\pi D_{\mathrm{B}}^2}{4}=g(\rho_{\mathrm{L}}-\rho_{\mathrm{V}})\frac{\pi D_{\mathrm{B}}^2}{4}L_{\mathrm{B}} \tag{3.14}$$

where C_{D} stands for the drag force coefficient, U_{BL} for the liquid velocity at the vapor blanket centreline, D_{B} for the vapor blanket diameter, g for the gravitational acceleration, and ρ_{V} for the saturated vapor density.

Besides, the drag force coefficient can be given by Chan and Prince model[140], proposed for pressure above 1 MPa, expressed as,

$$C_{\mathrm{D}}=\frac{48\mu_{\mathrm{L}}}{\rho_{\mathrm{L}}D_{\mathrm{B}}(U_{\mathrm{B}}-U_{\mathrm{BL}})} \tag{3.15}$$

in which μ_{L} denotes the liquid viscosity.

In addition, the bubble diameter is postulated to be proportional to the dimensional diameter proposed by Fritz[141],

$$D_{\mathrm{B}}\propto\sqrt{\frac{\sigma}{g(\rho_{\mathrm{L}}-\rho_{\mathrm{V}})}} \tag{3.16}$$

It is assumed that the vapor blanket length L_{B} is equal to the critical wavelength of the Helmholtz instability of the liquid-vapor interface,

$$L_{\mathrm{B}}=\frac{2\pi\sigma(\rho_{\mathrm{V}}+\rho_{\mathrm{L}})}{\rho_{\mathrm{V}}\rho_{\mathrm{L}}U_{\mathrm{B}}^2} \tag{3.17}$$

where σ is the surface tension.

Dimensionless velocity and length are introduced and expressed as,

$$\text{dimensionless velocity: } U^* = \frac{U}{G/\rho_\mathrm{V}} \tag{3.18}$$

$$\text{dimensionless length: } L^* = \frac{L}{D_\mathrm{h}} \tag{3.19}$$

Thereby, by substituting variables with dimensionless velocity (see Eq.(3.18), where G denotes the mass flux, ρ_V for the saturated vapor density) and dimensionless length (see Eq.(3.19), in which D_h stands for the tube diameter), Eqs.(3.13)–(3.17) would be converted to a set of dimensionless formulas,

$$\begin{cases} \dfrac{q_\mathrm{c}}{GH_\mathrm{VL}} = \dfrac{\rho_\mathrm{L}}{\rho_\mathrm{V}} \cdot \dfrac{\delta^* U_\mathrm{B}^*}{L_\mathrm{B}^*} \\ \dfrac{1}{2} C_\mathrm{D} \cdot (U_\mathrm{B}^* - U_\mathrm{BL}^*)^2 = L_\mathrm{B}^* \cdot \dfrac{D_\mathrm{h} g \rho_\mathrm{V}^2}{G^2} \cdot \left(1 - \dfrac{\rho_\mathrm{V}}{\rho_\mathrm{L}}\right) \\ L_\mathrm{B}^* \cdot {U_\mathrm{B}^*}^2 = 2\pi \cdot \left(1 + \dfrac{\rho_\mathrm{V}}{\rho_\mathrm{L}}\right) \cdot \dfrac{\sigma \rho_\mathrm{V}}{\mathrm{G}^2 D_\mathrm{h}} \\ C_\mathrm{D} = \dfrac{48}{D_\mathrm{B}^* (U_\mathrm{B}^* - U_\mathrm{BL}^*)} \cdot \dfrac{\rho_\mathrm{V}}{\rho_\mathrm{L}} \cdot \dfrac{\mu_\mathrm{L}}{G D_\mathrm{h}} \\ D_\mathrm{B}^* = \dfrac{D_\mathrm{B}}{D_\mathrm{h}} \propto \sqrt{\dfrac{\sigma}{D_\mathrm{h}^2 g (\rho_\mathrm{L} - \rho_\mathrm{V})}} \end{cases} \tag{3.20}$$

Regarding the vapor blanket, the boiling number $Bo = q_\mathrm{c}/GH_\mathrm{VL}$, the density ratio $\pi_\rho = \rho_\mathrm{V}/\rho_\mathrm{L}$, the Froude number $Fr_\mathrm{V} = G^2/(D_\mathrm{h} g \rho_\mathrm{V}^2)$, the Weber number $We_\mathrm{V} = \mathrm{G}^2 D_\mathrm{h}/(\sigma \rho_\mathrm{V})$, the Reynolds number with liquid properties $Re_\mathrm{L} = GD_\mathrm{h}/\mu_\mathrm{L}$, and the dimensionless diameter $\pi_\mathrm{D} = \sqrt{\sigma/[D_\mathrm{h}^2 g(\rho_\mathrm{L} - \rho_\mathrm{V})]}$ are accountable dimensionless parameters. Additionally, since the Froude number Fr_V could be expressed as a function of We_V, π_ρ, and π_D, Fr_V is excluded and will not be considered in the new model.

Further, in the view of the liquid sublayer, U_BL and δ are related to the near-wall velocity distribution and near-wall temperature distribution. Suppose that the superheated layer y^* is equal to the distance from the centerline of the vapor blanket to the wall, so that,

$$y^* = \delta + D_\mathrm{B}/2 \tag{3.21}$$

Supposing y^* could be calculated with the three-layer near wall temperature distribution[142], the liquid sublayer thickness could be obtained from Eq.(3.21). Accordingly, U_BL could be obtained by using the three-layer near wall velocity distribution[84]. Thereby, it can be concluded from three-layer near wall velocity and temperature distribution, that the Reynolds number $Re_\mathrm{L} = GD_\mathrm{h}/\mu_\mathrm{L}$, the Prandtl number $Pr_\mathrm{L} = \mu_\mathrm{L} c_{p,\mathrm{L}}/\lambda_\mathrm{L}$ is the most significant to the calculation of the U_BL and δ[84,

142].

Moreover, for two-phase flow boiling, the quality at the critical point x_c is usually a crucial parameter. In summary, for DNB type boiling crisis, dimensionless parameters in the Eq.(3.22) should be considered in the new model.

$$Bo = f(We_V, Re_L, Pr_L, \pi_D, \pi_\rho, x_c) \tag{3.22}$$

3.3.1.2. Dryout

As Figure 2.4(b) shows, the dryout of the liquid film in annular flow leads to the dryout type boiling crisis. As the liquid film thickness at the dryout point is thin, the effect of entrainment could be neglected. Assume that evaporation rate equals to deposition rate at the dryout point. Supposing the supplied heat is used to evaporate the liquid film, the heat balance is thereby written as,

$$q_c = \rho_V U_{EV} H_{VL} \tag{3.23}$$

where q_c denotes the critical heat flux, ρ_V saturated vapor density, U_{EV} the vapor velocity induced by the vaporization of the liquid film, H_{VL} the evaporation heat.

At the dryout point, suppose the work done by evaporation force equals the droplet turbulent kinetic energy supporting it to reach the wall[128]. Then, it can be expressed by,

$$\frac{1}{2}\rho_V U_{EV}^2 \cdot \frac{\pi D_d^2}{4} \cdot S = \frac{1}{2}\rho_d U_d^2 \cdot \frac{\pi}{6} D_d^3 \tag{3.24}$$

where D_d is devoted for the droplet diameter, S for the working distance of the evaporation force, ρ_d for the density of the droplet, U_d for the droplet turbulent velocity corresponding to the droplet kinetic energy supporting it to reach the wall. S is assumed to be proportional to the tube diameter D_h[128].

In addition, U_d can be given by correlation for the average velocity fluctuation of the droplets. Here, the correlation of Cousins et al.[143] is applied for it,

$$U_d = 0.022\left[\frac{GD_h(1-x_c)}{\mu_d}\right]^{-0.26} \cdot \left(\frac{\mu_d}{\mu_V}\right)^{0.26} \cdot \left(\frac{1-x_c}{1-\alpha_c}\right) \cdot \frac{G}{\rho_d} \tag{3.25}$$

in which D_h stands for the tube diameter, x_c for the critical quality, μ_d for the viscosity of the droplet, μ_V for the vapor viscosity, α_c for the void fraction, G for the mass flux, and ρ_d for the droplet density.

Further, the droplet diameter D_d can be given by the correlation of Kataoka et al.[144],

$$D_d = 0.01\frac{\sigma}{\rho_V U_{sV}^2}\left(\frac{\rho_V U_{sV} D_h}{\mu_V}\right)^2 \left(\frac{\rho_V}{\rho_d}\right)^{-\frac{1}{3}} \left(\frac{\mu_V}{\mu_d}\right)^{2/3} \tag{3.26}$$

where the $U_{sV} = x_c G/\rho_V$ is the superficial vapor velocity, σ the surface tension. ρ_V and ρ_d are devoted for the vapor density and the droplet density, respectively. μ_V and μ_d represent the vapor viscosity and droplet viscosity, respectively. D_h stands for the tube diameter.

Substituting Eqs.(3.24)–(3.26) to Eq.(3.23), the critical heat flux q_c would be expressed by a complicated correlation without unknown parameters. Further, supposing the droplet and vapor are in equilibrium and the temperature of vapor and droplet are therefore at saturation temperature, it could be simplified to the following combination of dimensionless parameters,

$$Bo = f(Re_V, We_V, \pi_\mu, \pi_\rho, x_c) \tag{3.27}$$

where, the boiling number is denoted by $Bo = q_c/GH_{VL}$, the Reynolds number with vapor properties $Re_V = GD_h/\mu_V$, the Weber number $We_V = G^2 D_h/(\sigma\rho_V)$, the viscosity ratio $\pi_\mu = \mu_V/\mu_L$, the density ratio $\pi_\rho = \rho_V/\rho_L$, and the critical quality x_c.

3.3.2. Derivation of CHF Model

As discussed above, key dimensionless parameters are identified, and a high-pressure CHF databank is established. Accordingly, this section will focus on the development of the new CHF model using these dimensionless parameters. In the present work, experimental results for water in the current high-pressure CHF databank, as listed in Table 3.1, is utilized to establish a new CHF correlation.

Although the mechanisms of DNB and dryout are different, as Eq.(3.22) and Eq.(3.27) demonstrated, key dimensionless parameters are similar. Furthermore, since reliable distinguish criteria between DNB and dryout is still unavailable so far, these dimensionless parameters will be considered together as,

$$Bo = f(We_V, Re_V, Pr_L, \pi_\mu, \pi_\rho, \pi_D, x_c) \tag{3.28}$$

Consequently, by establishing connection between the Boiling number Bo and dimensionless parameters in the RHS of Eq.(3.28), a prediction correlation of CHF will be obtained. To do this, the key issue is to identify the most significant ones from these dimensionless parameters.

The group-wise statistic method proposed by Cheng et al.[62], which has been applied successfully to develop prediction correlations of heat transfer to supercritical fluids, is used to select the most significant dimensionless parameters. It is demonstrated that the group-wise statistic approach could provide consistent results compared to other global sensitivity statistic method, e.g., Spearman's rank correlation coefficient. Additionally, the group-wise statistic could give the variation tendency in the meanwhile[62]. Therefore, the derivation of the new CHF correlation with the group-wise statistic method will be utilized in the present work and introduced in the following.

For each dimensionless parameter in the RHS of Eq.(3.28), the data points are sorted

according to the value of the selected dimensionless parameter. Then, the data points are divided into groups in sequence, with 100 data points in one group. For each group, the mean value μ and standard deviation σ of the selected dimensionless parameter and the Boiling number are calculated, respectively. In addition, the measured Boiling number Bo_{m} is calculated by,

$$Bo_{\mathrm{m}} = q_{\mathrm{c}}/GH_{\mathrm{VL}} \tag{3.29}$$

in which q_{c} and G are the heat flux and mass flux recorded in the CHF databank, respectively, H_{VL} is the evaporation heat. Consequently, the variation of the Bo_{m} with the selected dimensionless parameter can be seen in Figure 3.2, with the mean value μ and the distribution range $(\mu - \sigma, \mu + \sigma)$.

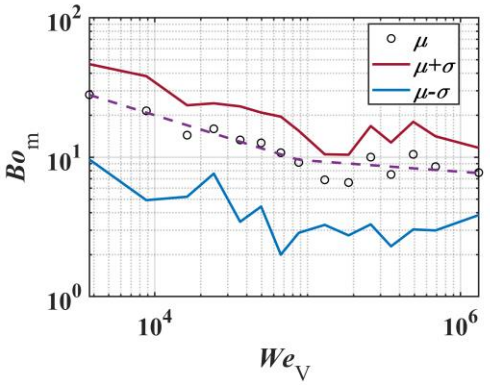

(a) Weber number We_{V}

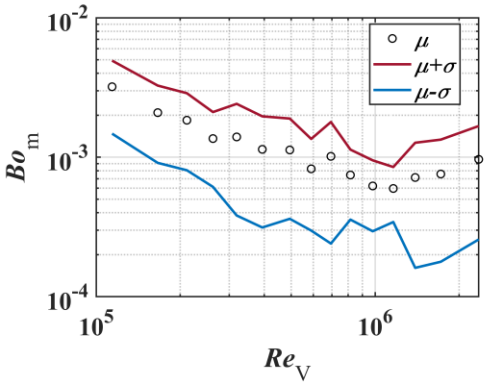

(b) Reynolds number Re_{V}

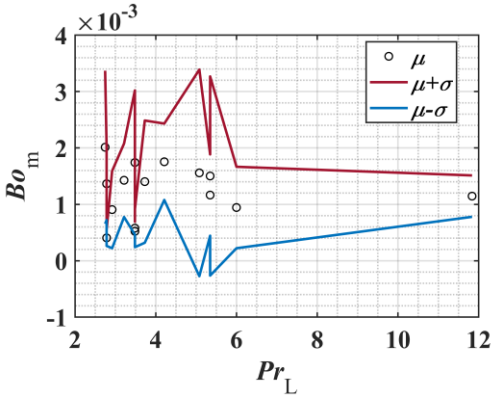

(c) Prandtl number Pr_{L}

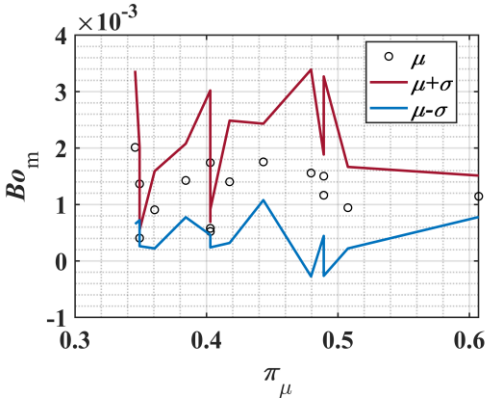

(d) Viscosity ratio π_{μ}

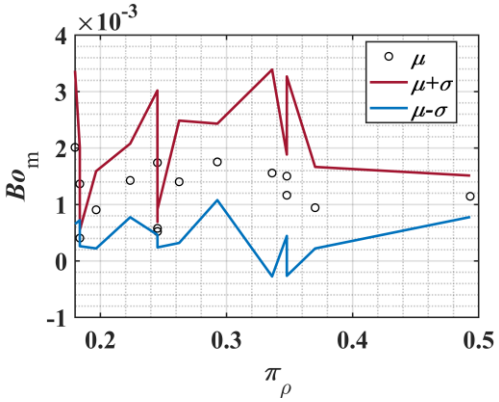

(e) Density ratio π_{ρ}

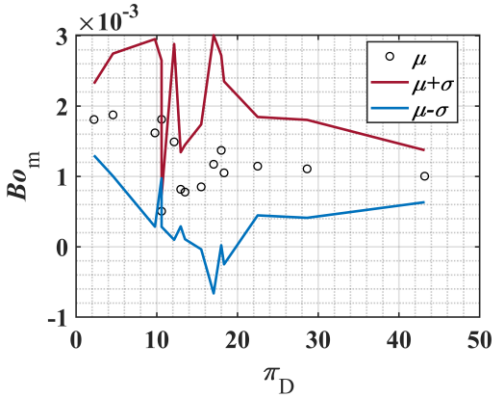

(f) Dimensionless diameter π_{D}

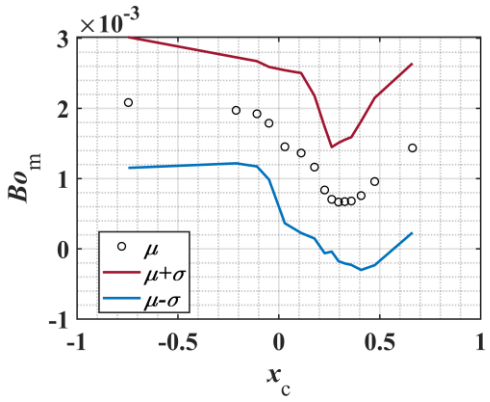

(g) Critical quality x_c

Figure 3.2.: Variation of Boiling number with dimensionless parameters

As illustrated, the value of the Boiling number keeps nearly constant with the variation of the Prandtl number Pr_L, the viscosity ratio π_{μ}, the density ratio π_{ρ}, and the dimensionless diameter π_D. Thereby, the variation of Boiling number is not sensitive to Pr_L, π_{μ}, π_{ρ}, and π_D, and these four dimensionless parameters will not be considered in the new model.

While the tendency of the Boiling number with the change of other dimensionless parameters is apparent, it implies that We_V, Re_V, and x_c are significant parameters. Hence, Eq.(3.28) could be simplified to,

$$Bo = f(We_V, Re_V, x_c) \tag{3.30}$$

Observing the variation tendency, as Figure 3.2(a) shows, the Boiling number decreases with the increase of Weber number We_V nearly monotonously. However, the tendency along Re_V and x_c are not monotonous. Therefore, it will be easier to establish a formula to describe the relationship between the Boiling number and the Weber number firstly.

Accordingly, the following equation is proposed to capture the effect of the Weber number,

$$Bo_{c1} = f(We_V) = \max(A_1, A_2) \tag{3.31}$$

with,

$$A_1 = 7.796 \times 10^{-2} \cdot We_V^{-0.439} \tag{3.32}$$

$$A_2 = 1.530 \times 10^{-3} \cdot We_V^{-0.0803} \tag{3.33}$$

In Figure 3.2(a), the Eq.(3.31) is plotted in a dash curve. As can be seen, the predicted line fits well with the mean value of data groups. Further, to assess the predictive capability of Bo_{c1}, the variation of the Boiling number ratio (Bo_{c1}/Bo_m) is analyzed. As illustrated, the mean value of data groups in Figure 3.3(a) and Figure 3.3(b) tends to equal to unity. Thereby, it implies that the Boiling number ratio (Bo_{c1}/Bo_m) is not sensitive to We_V, and Re_V. While as shown in Figure 3.3(c), the Boiling number ratio still increases apparently along the critical quality. Therefore, a function with x_c is proposed to modify Bo_{c1},

$$f(x_c) = (B_1 + B_2 + B_3) - \max(B_1, B_2, B_3) - \min(B_1, B_2, B_3) \tag{3.34}$$

where,

$$B_1 = 2.156 \cdot (1 - x_c)^{0.688} \tag{3.35}$$

$$B_2 = 1.841 \cdot (1 - x_c)^{2.137} \tag{3.36}$$

$$B_3 = 0.672 \cdot (1 - x_c)^{0.219} \tag{3.37}$$

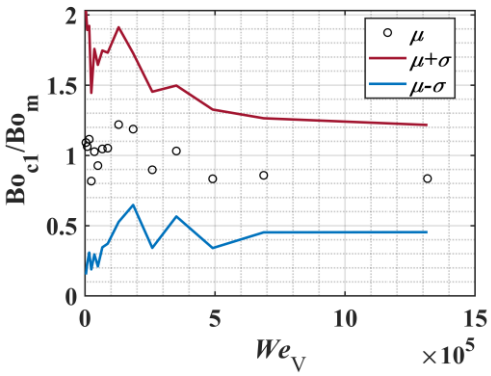

(a) Weber number We_V

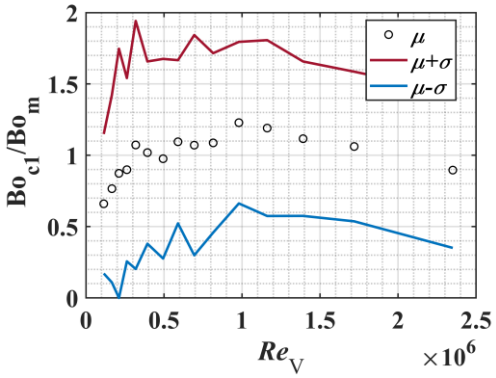

(b) Reynolds number Re_V

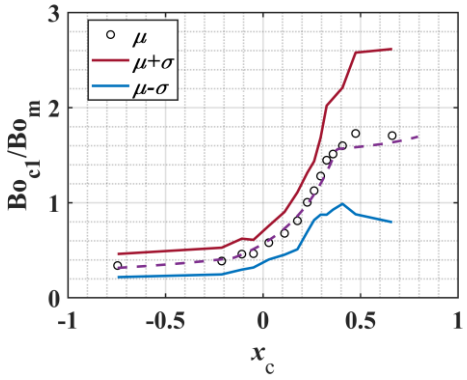

(c) Critical quality x_c

Figure 3.3.: Variation of Boiling number ratio $\frac{Bo_{c1}}{Bo_m}$ with dimensionless parameters

The function $f(x_c)$ is the middle value of B_1, B_2, and B_3. Additionally, the result calculated by the function $f(x_c)$ is plotted with dash line in Figure 3.3(c) and it gets good agreement with the mean value dots of the Boiling number ratio (Bo_{c1}/Bo_m).

Thus, the modified version of the Boiling number will be,

$$Bo_{c2} = f(We_V) \cdot f(x_c) \tag{3.38}$$

Moreover, the predictive capability of the modified Boiling number Bo_{c2} are supposed to be evaluated. Figure 3.4 exhibits the distribution of the Boiling number ratio (Bo_{c2}/Bo_m) along selected dimensionless parameters. As seen, the Boiling number ratio does not change along the dimensionless parameter further. It indicates that the predictive capability of Bo_{c2} is acceptable. Further modification to Bo_{c2} is not required.

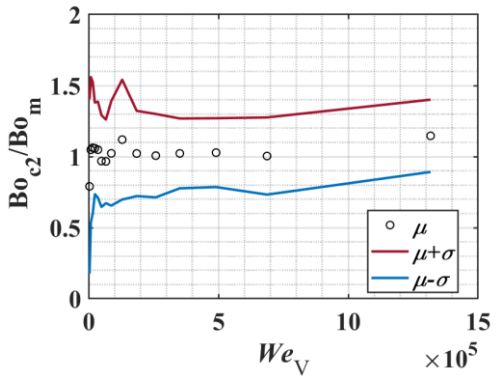

(a) Weber number We_V

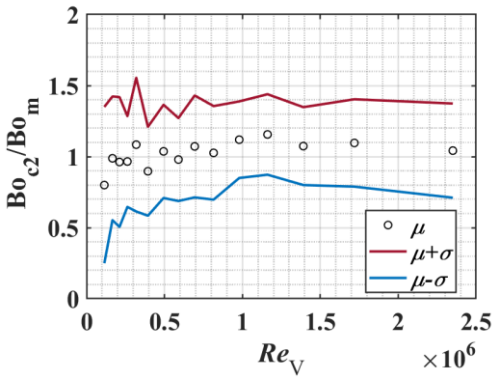

(b) Reynolds number Re_V

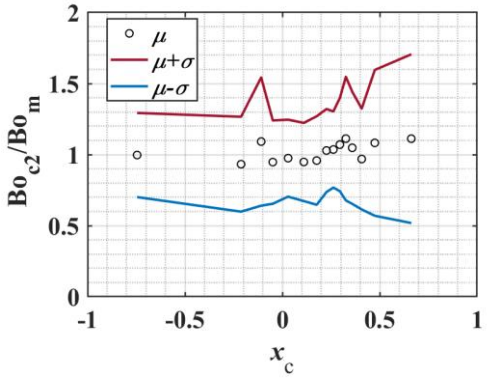

(c) Critical quality x_c

Figure 3.4.: Variation of the modified Boiling number ratio $\frac{Bo_{c2}}{Bo_m}$ with dimensionless parameters

In summary, as illustrated by Eq.(3.38), the final version of the present CHF prediction model will be a combination of the Boiling number, Weber number We_V, and the critical quality x_c. In addition, for the high-pressure water CHF databank listed in Table 3.1, the Weber number We_V ranges from 5.43× 10^2 to 2.67× 10^6, the critical quality from -1.768 to 0.955.

3.4. Assessment of Present CHF Model

Error parameter defined by Eq.(3.9) will be calculated with the new proposed CHF correlation (see Eq.(3.38)) to assess its predictive capability. For the CHF database of high-pressure water, which is utilized to develop the present CHF correlation, Figure 3.5 shows the distribution of the error parameter versus the pressure, mass flux, tube diameter, and the critical quality, respectively. As illustrated, no apparent systematic error is observed. However, it is illustrated by Figure 3.5(b) that the present correlation tends to underestimate the CHF at mass flux lower than 500 kg/(m^2·s), which implies that the present correlation is more conservative.

For the present CHF correlation, the mean value and RMS of the error parameter with the 1484 high-pressure water CHF data points are 2% and 37.4%, respectively. Figure 3.6 compares the mean error and the standard deviation of the present correlation and some of previous CHF prediction methods (see Table 3.2). As seen, the present correlation gives a better prediction accuracy.

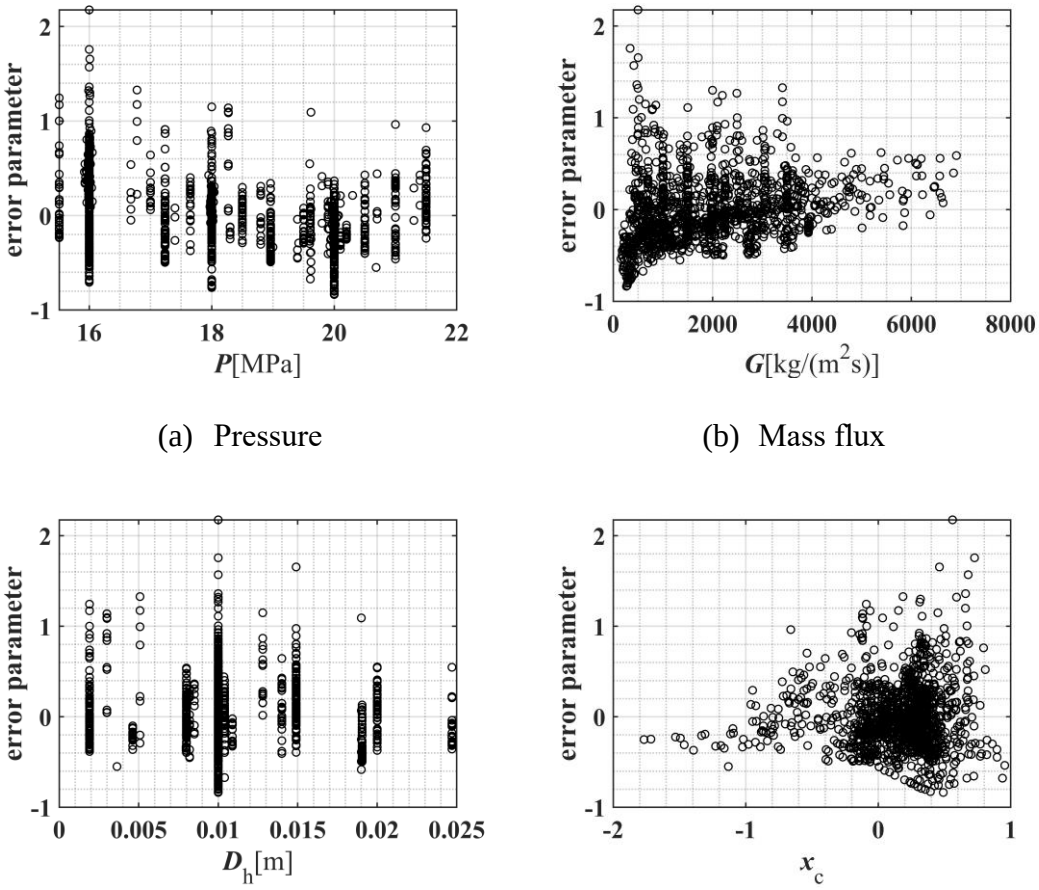

(a) Pressure (b) Mass flux

(c) Tube diameter (d) Critical quality

Figure 3.5.: Distribution of the CHF prediction error parameter

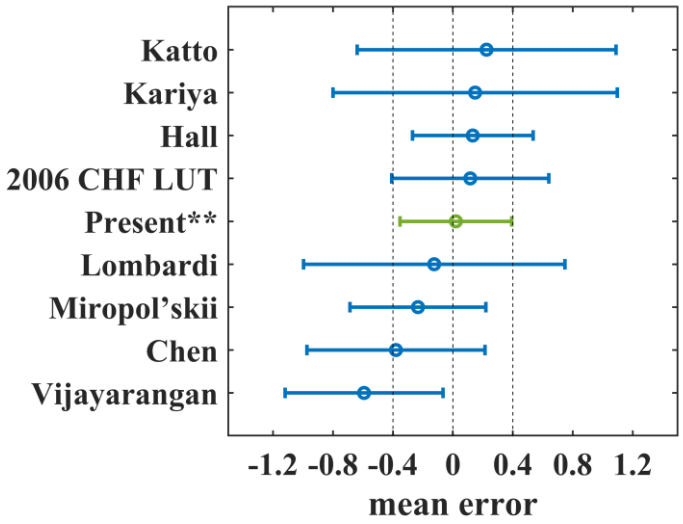

Figure 3.6.: Mean error and standard deviation of different correlations with the high-pressure water CHF database

3.5. Validation of Present CHF Model

The present CHF correlation, as a dimensionless one developed from water experiments, has potential to be applied for non-aqueous fluids. Accordingly, predictive capability of the present correlation is evaluated and compared with other prediction methods and CHF experiment with non-aqueous fluids.

Table 3.3.: Experimental data in the high-pressure R12 and CO_2 CHF databank

	R12 (N=1140)		CO_2 (N=28)	
Parameters	min	max	min	max
P, MPa	2.9	3.5	6.2	7.1
P_r, -	0.70	0.85	0.84	0.96
G, kg/(m^2·s)	121	10440	494	2041
D_h, m	0.003	0.0158	0.008	0.008
x_c, -	-0.745	0.902	-0.771	0.294
q_c, kW/m^2	18.0	991.0	53.6	225.2
$Bo \times 10^4$	1.92	35.89	6.77	17.19
We_V	9.61×10^2	2.6×10^6	1.51×10^4	6.91×10^5

As mentioned in Section 3.1, the present work collects high-pressure R12 and CO_2 CHF experiments as well. The range of parameters could be found in Table 3.3. For the high-pressure R12 databank, it is made up of 1140 data points with the reduced pressure up to 0.85. The range of Weber number covers from 9.61×10^2 to 2.6×10^6, critical quality from -0.745 to 0.902. However, the high-pressure CO_2 databank has only 28 data points with reduced pressure from 0.84 to 0.96. Moreover, further information about the CHF databank could be found in the Appendix C.

Table 3.4.: Prediction accuracy of different correlations for the high-pressure R12 and CO_2 CHF databank

	R12			CO_2		
Model	No. of data used	*ME*	*RMS*	No. of data used	*ME*	*RMS*
Present correlation	1140	-0.020	0.333	28	0.068	0.304
Miropol'skii[103]	1140	-0.807	0.809	28	-0.805	0.812
Hall[79]	356	-0.162	0.236	9	0.785	0.886
Lombardi[99]	1140	-0.349	0.487	28	-0.607	0.620
Katto[100]	356	0.113	0.319	9	0.002	0.376
Kariya[94]	1140	0.434	0.879	28	0.093	0.304
Shah[96]	1140	0.368	1.169	28	1.277	1.526

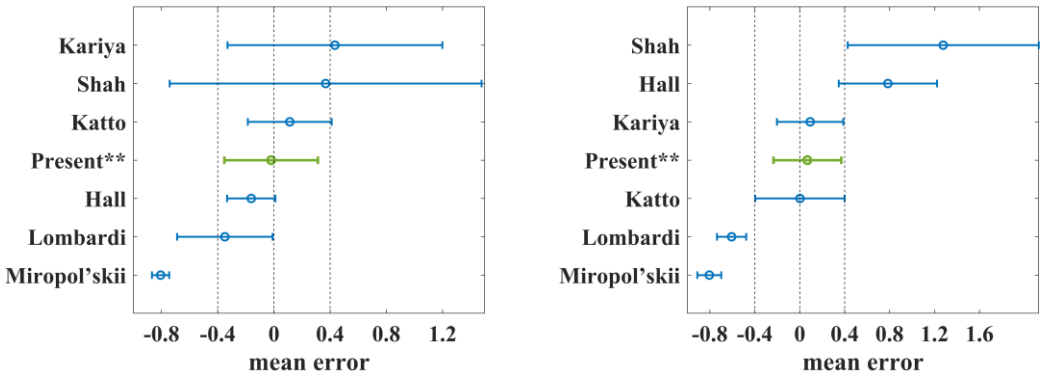

(a) R12 CHF database (b) CO_2 CHF database

Figure 3.7.: Comparison of different correlations with the high-pressure R12 and CO_2 CHF database

As listed in Table 3.4, for the present CHF correlation, i.e., Eq.(3.38), the mean error and RMS error with R12 CHF experiments are 2% and 33.3%, respectively. While for the CO_2 CHF database, the mean error becomes higher, which is 6.8%, but still seems acceptable compared to other prediction methods. The comparison between different prediction methods is shown in Figure 3.7 as well, with the mean error and the standard deviation of different prediction methods. It is indicated that the present CHF correlation shows a good adaptation to non-aqueous fluids.

Regarding previous prediction methods, only dimensionless correlations are listed in Table 3.4. It demonstrates that the predictive capability of the Kariya correlation[94] is comparable to the present CHF correlation when applied to the CO_2 database, with the mean error of 9% and RMS error of 30.4%. Particularly, it seems that the Katto's sublayer dryout[100] model also obtains a good prediction to CO_2 experiments, while it can only be applied for 9 subcooled data points. Generally, the present CHF correlation shows a better prediction accuracy than previous prediction methods.

3.6. Parametric CHF Trends

In this section, the parametric trends predicted by the Eq.(3.38) as well as experiments will be discussed for uniformly heated round tubes with water as coolant. Figure 3.8-Figure 3.10, solid lines stand for the calculated CHF, discrete dots for experimental CHF data points. As seen, the predicted CHF is in good agreement with experimental results. In the following, the influence of pressure, mass flux, and tube diameter will be discussed.

3.6.1. Effect of Pressure on CHF

Figure 3.8 shows the influence of pressure on CHF. Figure 3.8(a) is the comparison of CHF for pressure at 16.0 MPa and 20.0 MPa, with mass flux at 1000 kg/(m^2·s) and tube diameter at 10 mm. Figure 3.8(b) shows the results with constant mass flux at 1500 kg/(m^2·s) and tube diameter at 10 mm, while the pressures are at 16 MPa, 18.5 MPa, and 21.5 MPa, respectively. Obviously, the higher pressure results in a lower CHF.

As shown by Figure 1.2, the increase in pressure leads to reduction in evaporation heat, which promotes the vaporization process. Thereby, refering to Eq.(3.13) and Eq.(3.23), the heat flux requied to make the liquid sublayer or liquid film dryout will decrease. Hence, the value of CHF both for DNB and dryout drops when the pressure increases.

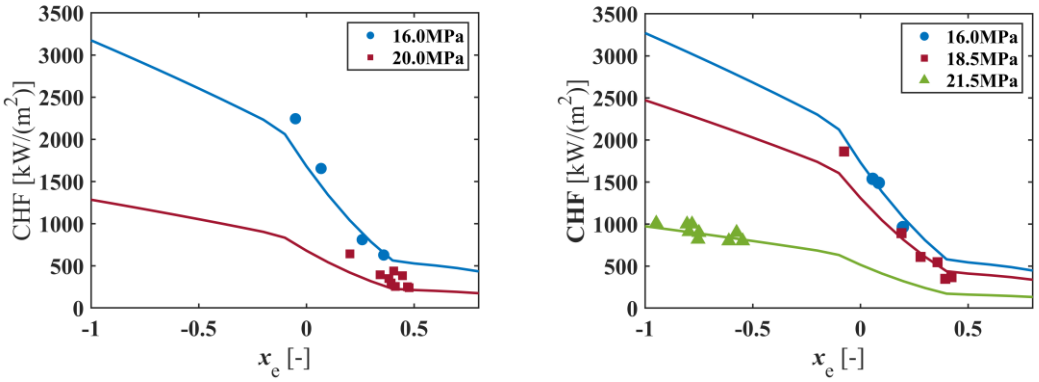

(a) G=1000 kg/(m^2·s), D=10 mm (b) G=1500 kg/(m^2·s), D=10 mm

Figure 3.8.: Variation of CHF with quality at different pressure

3.6.2. Effect of Mass Flux on CHF

Figure 3.9(a) shows the variation of CHF at the mass flux of 350, 1500, 2000, and 3500 kg/(m^2·s), respectively, with a constant pressure at 18 MPa and tube diameter at 10 mm. Similarly, the influence of mass flux at pressure of 20 MPa is indicated by Figure 3.9(b), with mass flux from 650 kg/(m^2·s) to 3500 kg/(m^2·s). There is an increase in CHF as the mass flux rises.

Regarding the sublayer dryout model for DNB, the higher mass flux could reduce the passage time of the liquid blanket for the increase in vapor velocity. Therefore, according to Eq.(3.13), the increase in mass flux leads to a higher CHF. With respect to dryout, the higher mass flux would enhance the turbulent convection, resulting in higher velocity fluctuation of the droplets. Consequently, referring to Eq.(3.24), it would increase the droplet deposition ability and thus increase the CHF.

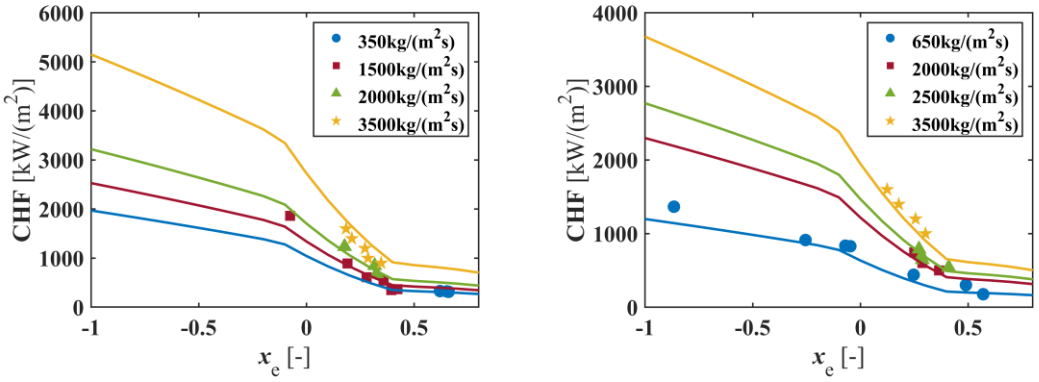

(a) P= 18 MPa, D=10 mm (b) P= 20 MPa, D=10 mm

Figure 3.9.: Variation of CHF with quality at different mass flux

3.6.3. Effect of Tube Diameter on CHF

The effect of tube diameter is shown in Figure 3.10 with pressure at 20 MPa. Figure 3.10(a) and Figure 3.10(b) compares the variation of CHF with tube diameter at mass flux of 700 kg/(m^2·s) and 3000 kg/(m^2·s), respectively. Figure 3.10(a) shows that when the tube diameter decreases form 20 mm to 10 mm, the CHF increases. The tendency indicated by Figure 3.10(b) is similar with tube diameter at 10 mm and 14.9 mm respectively.

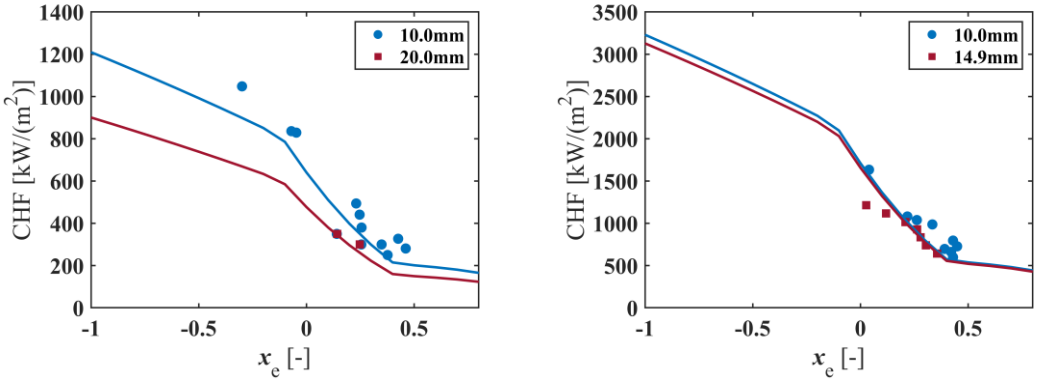

(a) P= 20 MPa, G=700 kg/(m^2·s) (b) P= 20 MPa, G=3000 kg/(m^2·s)

Figure 3.10.: Variation of CHF with quality at different tube diameter

With a smaller tube diameter, the slope of the velocity profile in the two-phase boundary layer will increase. Therefore, the vapor blanket velocity will be higher. As a result, a smaller tube diameter gives rise to the critical heat flux for DNB type. Meanwhile, for dryout, according to Eq.(3.25), the decrease in tube diameter will increase the droplet turbulent velocity, so that the droplet deposition capability will be promoted. The CHF

thus increases with the decrease of tube diameter.

3.7. Summary

In this chapter, a CHF databank has been established for the high-pressure region with reduced pressure above 0.7 in uniformly heated round tubes. The reliability of the databank is guaranteed by heat balance verification, duplication screening, and reproducibility check. In consequence, the new CHF databank contains 2652 data points in total for water, R12, and CO_2. By comparing against the high-pressure water CHF databank, the predictive capability of previous prediction methods is evaluated. It is implied that a new CHF model for the high-pressure region is necessary.

To develop a new dimensionless CHF correlation, firstly, the relevant dimensionless parameters are identified out by analyzing the mechanism of DNB and dryout respectively. Secondly, the group-wise statistic method is applied to figure out the most significant dimensionless parameters. Finally, it is indicated that the new CHF correlation is a function with the Boiling number, Weber number, and the critical quality, written as,

$$Bo_c = f(We_V) \cdot f(x_c)$$

where,

$$f(We_V) = \max(A_1, A_2)$$

$$f(x_c) = (B_1 + B_2 + B_3) - \max(B_1, B_2, B_3) - \min(B_1, B_2, B_3)$$

and,

$$A_1 = 7.796 \times 10^{-2} \cdot We_V^{-0.439}$$

$$A_2 = 1.530 \times 10^{-3} \cdot We_V^{-0.0803}$$

$$B_1 = 2.156 \cdot (1 - x_c)^{0.688}$$

$$B_2 = 1.841 \cdot (1 - x_c)^{2.137}$$

$$B_3 = 0.672 \cdot (1 - x_c)^{0.219}$$

The new CHF correlation has the following validity range:

- We_V: 5.43× 10^2 ~ 2.67× 10^6 ,
- x_c: -1.768 ~ 0.955.

As demonstrated, although the new CHF correlation is developed from the high-pressure water CHF databank, it gets good agreement with the test data obtained from R12 and CO_2. Besides, the new CHF correlation also shows better predictive capability over previous prediction methods.

Moreover, it is illustrated that the value of CHF falls with a higher pressure or larger tube diameter, while the higher mass flux leads to a higher CHF.

4. Modelling of Post-CHF Heat Transfer

As has been reviewed in Section 2.3, after the boiling crisis occurs, the post-CHF heat transfer region will be encountered, where the heated wall can no longer be cooled by the continuous liquid phase. Corresponding to DNB and dryout, post-CHF heat transfer are indicated as post-DNB heat transfer and post-dryout (PDO) heat transfer, respectively. Since the high-pressure region is of interest in the present work and post-DNB heat transfer experiment is unavailable, this chapter will focus on post-dryout heat transfer. A post-dryout heat transfer databank will be established. Then, predictive capability of previous prediction methods will be evaluated.

4.1. PDO Heat Transfer Databank

Here, for droplet flow heat transfer, since the wall temperature is usually not very high, the portion of radiation heat transfer could be neglected. Supposing the boiling system is under equilibrium condition, the vapor phase is in saturation temperature. Further, supposing the direct droplet-wall heat transfer is neglected, the supplied heat is transferred to saturated vapor totally and then utilized to evaporate the saturated droplets by interfacial heat transfer. Thereby, the mass quality will equal to the equilibrium quality derived from heat balance, which is the maximum value of actual vapor quality[115]. In consequence, this assumption will provide an upper boundary to the stable PDO heat transfer coefficient and therefore a minimum wall temperature limit.

Further, assume that the forced convection heat transfer to saturated vapor in the droplet flow can be described by the well-known Dittus-Boelter heat transfer correlation, expressed as,

$$Nu_{\mathrm{eq}} = 0.023 Re_{\mathrm{V,eq}}^{0.8} Pr_{\mathrm{V}}^{0.4} \tag{4.1}$$

where Nu_{eq} denotes the equilibrium Nusselt number. $Re_{\mathrm{V,eq}} = GD_{\mathrm{h}}x_{\mathrm{m}}/(\mu_{\mathrm{V}}\alpha)$ is the equilibrium Reynolds number, here x_{m} is the mass quality evaluated by Eq.(2.40), and α is the void fraction calculated by Eq.(2.41). $Pr_{\mathrm{V}} = \mu_{\mathrm{V}}c_{p,\mathrm{V}}/\lambda_{\mathrm{V}}$ is devoted for the Prandtl number, where μ_{V}, $c_{p,\mathrm{V}}$, and λ_{V} are the dynamic viscosity, specific heat, and thermal conductivity of saturated vapor. Then, the equilibrium wall temperature $T_{\mathrm{w,eq}}$

would be given by,

$$T_{\mathrm{w,eq}} = T_{\mathrm{V,e}} + \frac{qD_{\mathrm{h}}}{\lambda_{\mathrm{V}} Nu_{\mathrm{eq}}} \tag{4.2}$$

with $T_{\mathrm{V,e}}$ the saturation temperature, q the heat flux, D_{h} the tube diameter.

In the PDO region, in case the $T_{\mathrm{w,m}}$ is lower than the $T_{\mathrm{w,eq}}$, it indicates that there are still significant direct droplet-wall heat transfer, so that the total heat transfer is better than equilibrium assumption. This condition is regarded as "unstable PDO region" according to the definition in Section 2.3.1. Otherwise, it will be the "stable PDO region".

As discussed in Section 2.3, for the stable PDO heat transfer region, only two heat transfer processes, i.e., heat transfer from the wall to the vapor phase and the interfacial heat transfer, are considered. In the current work, to simplify the model mechanism, the unstable PDO heat transfer region is not considered. After data points with the wall temperature lower than the $T_{\mathrm{w,eq}}$ are discarded, reliable check is carried out as well as that for the CHF databank. Details of reliable data check, the literature sources, and parameter ranges are given in Appendix E.

Since the high-pressure region is of interest in the present work, 5391 data points with reduced pressure over 0.7 are obtained for the stable post-dryout region in round tubes with uniform heating and upward flow. Parameter ranges of these high-pressure data points are listed in Table 4.1. The pressure covers the range from 15.92 to 21.51 MPa, mass flux from 492.8 to 3500.0 kg/(m^2·s), tube diameter from 2.5 to 24.7 mm, heat flux from 147.0 to 1923.0 kW/m^2, equilibrium quality from 0.001 to 0.999, and the wall superheat from 8.66 to 304.2 ℃.

Table 4.1.: Parameter ranges of the high-pressure PDO heat transfer measurements with water in uniformly heated round tubes

Parameters	P [MPa]	P_{r} [-]	G [kg/(m^2·s)]	D_{h} [mm]	q [kW/m^2]	x_{e} [-]	$T_{\mathrm{w}} - T_{\mathrm{s}}$ [℃]
Min	15.92	0.722	497.8	2.5	147.0	0.001	8.66
Max	21.51	0.975	3500.0	24.7	1923.0	0.999	304.20

4.2. Assessment of Previous PDO Heat Transfer Model

The predictive capability of previous high-pressure PDO heat transfer prediction method will be assessed against high-pressure PDO heat transfer experiments (see Table 4.1). For each data point, the error parameter will be evaluated by,

$$\varepsilon_i = \frac{h_{\mathrm{cal}}(i) - h_{\mathrm{m}}(i)}{h_{\mathrm{m}}(i)} \tag{4.3}$$

$h_{\mathrm{cal}}(i)$ is the calculated HTC given by previous prediction methods. $h_{\mathrm{m}}(i)$ denotes

the measured HTC, expressed as,

$$h_{\mathrm{m}}(i) = \frac{q(i)}{T_{\mathrm{w}}(i) - T_{\mathrm{V,e}}(i)} \tag{4.4}$$

with $q(i)$ for the supplied heat flux, $T_{\mathrm{w}}(i)$ for the wall temperature, and $T_{\mathrm{V,e}}(i)$ for the equilibrium vapor temperature.

Thereby, statistical parameters, i.e., ME, SD, and RMS of the error parameter (ε_i), are calculated by Eq.(3.10), Eq.(3.11), and Eq.(3.12), respectively. The comparison of the predictive capability among existing prediction methods is carried out and listed in Table 4.2. The 2003 Post-CHF LUT[118] can only be applied to 2839 data points, while other experimental data points are out of the table prediction range. It achieves mean error of -15.1% and RMS error of 25.6%. As indicated by the reference [118], most areas of the LUT are colored in yellow in the high-pressure region, which implies that most table values are derived from heat transfer models rather from experiments directly. Therefore, the 2003 Post-CHF LUT[118] could not give a satisfying prediction. The mean error and RMS error provided by Slaughterbeck correlation[135] are -20.5% and 25.2%, respectively. The Groeneveld correlation[111] is with mean error of 19.3% and RMS error of 37.1%. In general, previous PDO heat transfer prediction methods could not provide a good prediction accuracy. Therefore, a new PDO heat transfer correlation is required.

Table 4.2.: Prediction accuracy of different correlations for PDO experiments in the high-pressure region

Model	*ME*	*SD*	*RMS*	No. of used data points
2003 Post-CHF LUT[118]	-0.151	0.207	0.256	2839
Miropol'skii[113]	0.487	0.560	0.742	5391
Slaughterbeck[135]	-0.205	0.146	0.252	5391
Groeneveld[111]	0.193	0.316	0.371	5391
Swenson[136]	0.432	0.475	0.642	5391

4.3. Development of PDO Heat Transfer Model

Referring to the discussion in Section 3.3 about the requirement of a new CHF correlation, the new PDO heat transfer correlation is supposed to be a dimensionless correlation and independent of upstream information. Hence, significant dimensionless parameters will be identified firstly.

4.3.1. Identification of Dimensionless Parameter

Analyzing the vapor-droplet system in one-dimension homogeneous mixture model and

according to the definition of Nusselt number, the two-phase Nusselt number Nu_{TP} for the stable PDO region can be expressed by,

$$Nu_{\mathrm{TP}} = \frac{qD_{\mathrm{h}}}{\lambda_{\mathrm{TP}}(T_{\mathrm{w}} - T_{\mathrm{TP}})} \tag{4.5}$$

Here, q stands for the heat flux, D_{h} for the tube diameter, λ_{TP} for the two-phase thermal conductivity, T_{w} for the wall temperature, and T_{TP} for the two-phase coolant temperature. Supposing λ_{TP} and T_{TP} can capture the real two-phase mixture property, the two-phase Nusselt number Nu_{TP} can thereby characterize the actual heat transfer characteristics. Obviously, it is usually difficult. Consequently, for the vapor-droplet system in the stable PDO region, the Nusselt number Nu calculated from measured parameters is normally written as,

$$Nu = \frac{qD_{\mathrm{h}}}{\lambda_{\mathrm{V}}(T_{\mathrm{w}} - T_{\mathrm{V,e}})} \tag{4.6}$$

with λ_{V} for the saturated vapor thermal conductivity and $T_{\mathrm{V,e}}$ for the equilibrium vapor temperature, i.e., saturation temperature.

Supposing the two-phase mixture properties could be estimated reasonably, the two-phase Nusselt number is thus written as,

$$Nu_{\mathrm{TP}} = c_{\mathrm{TP}} Re_{\mathrm{TP}}^{n_{\mathrm{TP}}} Pr_{\mathrm{TP}}^{m_{\mathrm{TP}}} \tag{4.7}$$

where c_{TP}, n_{TP} and m_{TP} are constant factors. Re_{TP} and Pr_{TP} are introduced for the two-phase Reynolds number and the two-phase Prandtl number, respectively.

Hence, by substituting Eq.(4.5) and Eq.(4.7) into Eq.(4.6), Nu will be rearranged as,

$$Nu = \frac{\lambda_{\mathrm{TP}}}{\lambda_{\mathrm{V}}} \cdot \frac{T_{\mathrm{w}} - T_{\mathrm{TP}}}{T_{\mathrm{w}} - T_{\mathrm{V,e}}} \cdot c_{\mathrm{TP}} \cdot \mathrm{Re}_{\mathrm{TP}}^{n_{\mathrm{TP}}} \cdot Pr_{\mathrm{TP}}^{m_{\mathrm{TP}}} \tag{4.8}$$

Besides, the two-phase Reynolds number Re_{TP} is assumed as,

$$Re_{\mathrm{TP}} = \frac{GD_{\mathrm{h}}}{\mu_{\mathrm{TP}}} \tag{4.9}$$

Referring to the research of McAdams et al.[145], the two-phase viscosity μ_{TP} can be expressed as a combination of local quality and saturation properties,

$$\frac{1}{\mu_{\mathrm{TP}}} = \frac{x_{\mathrm{m}}}{\mu_{\mathrm{V}}} + \frac{1 - x_{\mathrm{m}}}{\mu_{\mathrm{L}}} \tag{4.10}$$

so that the Re_{TP} will be expressed by,

$$Re_{\mathrm{TP}} = \frac{GD_{\mathrm{h}}}{\mu_{\mathrm{V}}} \left[x_{\mathrm{m}} + \frac{\mu_{\mathrm{V}}}{\mu_{\mathrm{L}}} (1 - x_{\mathrm{m}}) \right] \tag{4.11}$$

Then, in the stable PDO region, as assumed, the supplied heat can only be transferred

to the vapor phase directly. Accordingly, since the near wall region is of great significance to heat transfer, the Prandtl number of the vapor phase in the wall temperature as $Pr_{\mathrm{w}} = c_{p,\mathrm{w}}\mu_{\mathrm{w}}/\lambda_{\mathrm{w}}$ is thereby introduced to simplify the Pr_{TP},

$$Pr_{\mathrm{TP}} = \frac{c_{p,\mathrm{TP}}\mu_{\mathrm{TP}}}{\lambda_{\mathrm{TP}}} = Pr_{\mathrm{w}} \cdot \frac{c_{p,\mathrm{TP}}}{c_{p,\mathrm{w}}} \cdot \frac{\mu_{\mathrm{TP}}}{\mu_{\mathrm{w}}} \cdot \frac{\lambda_{\mathrm{w}}}{\lambda_{\mathrm{TP}}} \tag{4.12}$$

As seen, Pr_{TP} is expressed as a combination of Pr_{w} and property ratios.

In the above and hereunder equations, properties with the subscript 'V', 'L', 'TP' and 'w', are saturated vapor properties, saturated liquid properties, two-phase mixture properties, and vapor properties at wall temperature, respectively. λ, c_p, and μ denote the thermal conductivity, the specific heat, and the dynamic viscosity, respectively. G is devoted for the mass flux, D_{h} for the tube diameter, and x_{m} for the mass quality given by Eq.(2.40).

Moreover, since the constant c_{TP}, n_{TP} and m_{TP} in Eq.(4.8) are unknown, here, referring to the Dittus-Boelter correlation, assign the value of 0.023, 0.8, and 0.4 to them, respectively. Thus, Eq.(4.8) will be expressed as,

$$Nu = F \cdot (0.023 Re_{\mathrm{TP}}^{0.8} Pr_{\mathrm{w}}^{0.4}) = F \cdot Nu_0 \tag{4.13}$$

with $Nu_0 = 0.023 Re_{\mathrm{TP}}^{0.8} Pr_{\mathrm{w}}^{0.4}$ as the reference Nusselt number. F is a correction factor to be determined. To correct the inaccuracy of constant factors in Nu_0, Re_{TP} and Pr_{W} should be considered in the correction factor F as well. Furthermore, comparing Eq.(4.8) and Eq.(4.13), the correction factor F is supposed to contain dimensionless parameters about the effect of the wall temperature T_{w}, the two-phase coolant temperature T_{TP}, and two-phase properties.

In the present work, the influence of T_{w} is considered by property ratios, i.e., $c_{p,\mathrm{V}}/c_{p,\mathrm{w}}$, $\lambda_{\mathrm{V}}/\lambda_{\mathrm{W}}$, $\mu_{\mathrm{V}}/\mu_{\mathrm{w}}$. The two-phase temperature T_{TP} characterizes the system non-equilibrium or the heat transfer ability from the vapor phase to the droplets directly (interfacial heat transfer). Referring to the research of Nishikawa et al.[146], Shah et al.[147], and Groeneveld et al.[115], Boiling number $Bo = q/(GH_{\mathrm{VL}})$ (H_{VL}, the evaporation heat), Prandtl number $Pr_{\mathrm{V}} = (c_{p,\mathrm{V}}\mu_V)/\lambda_{\mathrm{V}}$, Reynolds number $Re_{\mathrm{V}} = (GD_{\mathrm{h}})/\mu_{\mathrm{V}}$, Froude number $Fr_{\mathrm{L}} = G^2/(D_{\mathrm{h}}\, g\rho_{\mathrm{L}}^2)$ (g, gravitational acceleration), Weber number $We_{\mathrm{V}} = (G^2 D_{\mathrm{h}})/(\sigma\rho_{\mathrm{V}})$ (σ, the surface tension), the equilibrium quality x_{e}, and the density ratio $\rho_{\mathrm{L}}/\rho_{\mathrm{V}}$ are significant dimensionless parameters to the non-equilibrium phenomena. Further, assume that two-phase properties could be expressed as a function about property ratios (i.e., $c_{p,\mathrm{L}}/c_{p,\mathrm{V}}$, $\lambda_{\mathrm{L}}/\lambda_{\mathrm{V}}$, $\mu_{\mathrm{L}}/\mu_{\mathrm{V}}$) and the mass quality x_{m} (see Eq. (2.40)). As a result, by removing independent parameters, the correction factor could be expressed by,

$$F = f\left(\frac{c_{p,\mathrm{V}}}{c_{p,\mathrm{w}}}, \frac{c_{p,\mathrm{L}}}{c_{p,\mathrm{V}}}, \frac{\lambda_{\mathrm{V}}}{\lambda_{\mathrm{W}}}, \frac{\lambda_{\mathrm{L}}}{\lambda_{\mathrm{V}}}, \frac{\mu_{\mathrm{V}}}{\mu_{\mathrm{w}}}, \frac{\mu_{\mathrm{L}}}{\mu_{\mathrm{V}}}, \frac{\rho_{\mathrm{L}}}{\rho_{\mathrm{V}}}, x_{\mathrm{e}}, Bo, Fr_{\mathrm{L}}, We_{\mathrm{V}}, Re_{\mathrm{TP}}, Pr_{\mathrm{W}}\right) \tag{4.14}$$

In the following, the most significant dimensionless parameters in Eq.(4.14) will be

identified to develop a new PDO heat transfer model.

4.3.2. Derivation of PDO Heat Transfer Model

Referring to Yu's work[148], the PDO heat transfer model developed from the whole pressure database achieves a better predictive capability, compared to the one developed with the same strategy but from high-pressure experiments (with reduced pressure above 0.7). Therefore, the prediction model for the whole pressure range will be discussed hereunder.

The databank for stable PDO heat transfer from experiments with water in uniformly heated vertical tubes is obtained and summarized in Table 4.3. It contains 9902 data points in total and covers a pressure range from 2.98 to 21.51 MPa, mass flux from 496.3 to 3500 kg/(m^2·s), tube diameter from 2.5 to 24.7 mm, heat flux from 147 to 1923 kW/m^2, equilibrium quality from 0.001 to 0.999, and wall superheat from 8.66 to 499.68 ℃.

Table 4.3.: Parameter range of the whole-pressure water PDO heat transfer experiments in uniformly heated round tubes

Parameters	P [MPa]	P_r [-]	G [kg/(m^2·s)]	D_h [mm]	q [kW/m^2]	x_e [-]	$T_w - T_s$ [℃]
Min	2.98	0.135	496.3	2.5	147	0.001	8.66
Max	21.51	0.975	3500	24.7	1923	0.999	499.68

The uniformly heated water database listed in Table 4.3 is applied to develop a new heat transfer model for the stable PDO region. As has been discussed in the previous section, the vital issue is to find out the most significant dimensionless parameters listed in Eq.(4.14). Referring to the derivation of the new CHF model, the group-wise statistic method proposed by Cheng et al.[62] is utilized in this section.

The Nusselt number ratio (Nu_0/Nu_m) is introduced to express the correction factor, with Nu_0 the reference Nusselt number in Eq.(4.13) and Nu_m the measured Nusselt number calculated by Eq.(4.6). After sorted and grouped with 400 data points in each group, the average value μ and standard deviation σ of dimensionless parameters and the Nusselt number ratio (Nu_0/Nu_m) are calculated for every group.

Accordingly, the dependence of (Nu_0/Nu_m) on the selected dimensionless parameter will be analyzed by plotting the distribution tendency, as can be seen from Figure 4.1.

Figure 4.1(a) illustrates that when the equilibrium quality x_e lower than 0.4, the Nusselt number ratio (Nu_0/Nu_m) decreases with the increase of x_e, while it keeps nearly constant when x_e exceeds 0.4.

Figure 4.1(b)–Figure 4.1(d) demonstrate that the (Nu_0/Nu_m) tends to decrease along the Froude number Fr_L, the Weber number We_V, and the Reynolds number Re_{TP}.

In Figure 4.1(e), as seen, the (Nu_0/Nu_m) falls as Pr_W increases when it is below unity, whereas it increases in case Pr_W above unity.

Besides, Figure 4.1(f) and Figure 4.1(g) give examples of dimensionless parameters on which the dependence is not strong. Thus, these dimensionless parameters will no longer be considered.

In the present work, the correction factor F_1 is introduced to compensate the dependence on Re_{TP},

$$F_1 = 8.346 \times 10^{-03} Re_{TP}^{0.319} \tag{4.15}$$

Followed by the correction with Re_{TP}, F_2 is proposed to capture the effect of Pr_W,

$$F_2 = \max\left(0.795 Pr_W^{-1.752}, 0.809 Pr_W^{1.287}\right) \tag{4.16}$$

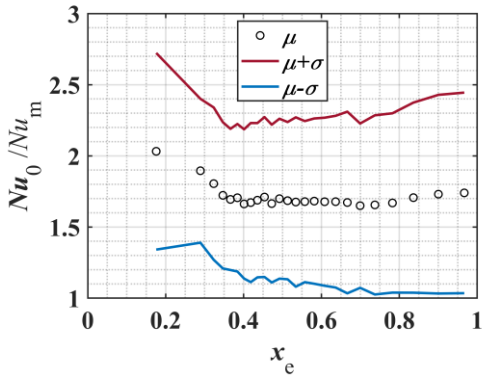

(a) Equlibrium quality x_e

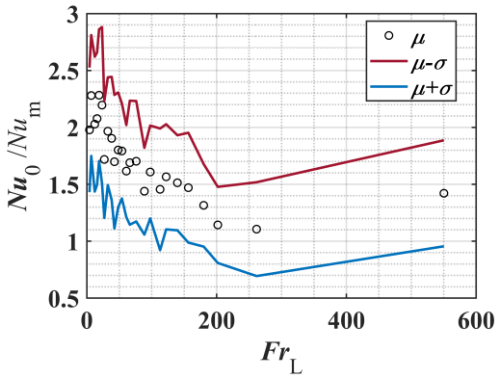

(b) Froude number Fr_L

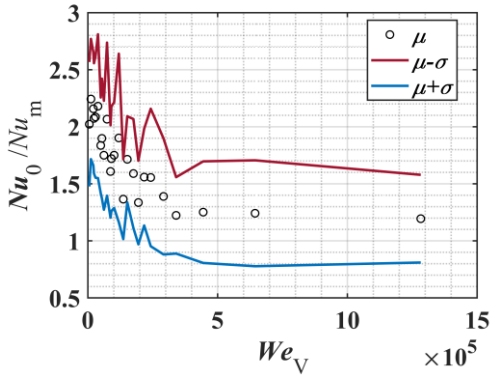

(c) Weber number We_V

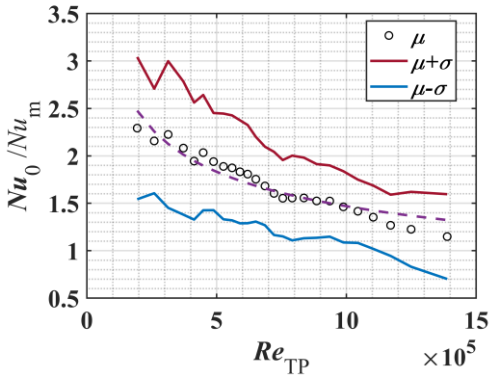

(d) Reynolds number Re_{TP}

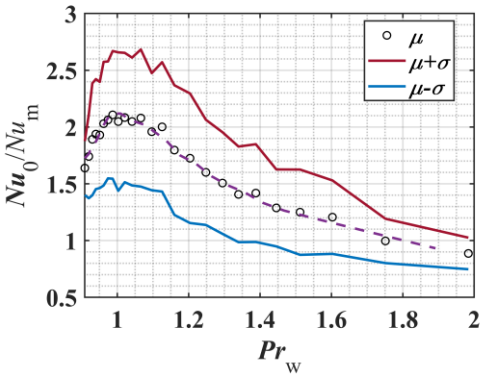

(e) Prandtl number Pr_{W}

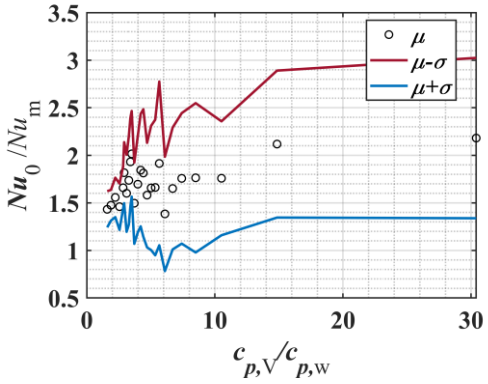

(f) Specific heat ratio $\frac{c_{p,\mathrm{V}}}{c_{p,\mathrm{W}}}$

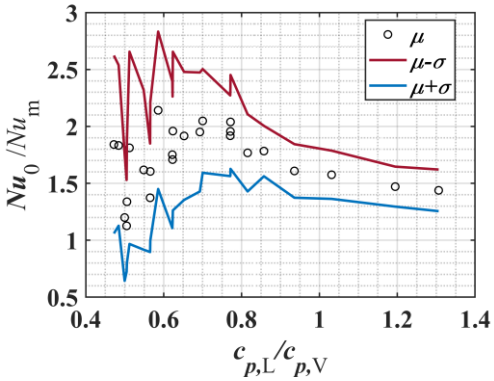

(g) Specific heat ratio $\frac{c_{p,\mathrm{L}}}{c_{p,\mathrm{V}}}$

Figure 4.1.: Variation of Nu_0/Nu_{m} versus dimensionless parameters

Correction factor F_1 and F_2 are also plotted in Figure 4.1(d) and Figure 4.1(e), respectively. As seen, the correction factors agree well with the group mean value. Specifically, the intersection of the two terms in F_2 is around $Pr_{\mathrm{W}} = 1$. The exponent for Pr_{W} in the new correlation will therefore be negative for $Pr_{\mathrm{W}} < 1$, which is different to the value of 0.4 in the single-phase Dittus-Boelter correlation. The thermal diffusivity is more significant compared to the momentum diffusivity when Prandtl number lower than unity. As mentioned, the heat transfer in the stable PDO region is determined by both the vapor-wall and vapor-droplet heat transfer. Therefore, the lower Pr_{W} may enhance the heat transfer ability by the increase of heat conduction in the near wall region. Thus, the exponent of correction factor with Pr_{W} is negative.

Accordingly, the new Nusselt number ratio will be given by,

$$\frac{Nu_{\mathrm{c1}}}{Nu_{\mathrm{m}}} = \frac{F_1 \cdot F_2 \cdot Nu_0}{Nu_{\mathrm{m}}} \tag{4.17}$$

The distribution of $(Nu_{\mathrm{c1}}/Nu_{\mathrm{m}})$ is exhibited in Figure 4.2. As seen, the $(Nu_{\mathrm{c1}}/Nu_{\mathrm{m}})$

keeps nearly constant along selected dimensionless parameters, except the equilibrium quality. It implies that the dependence on the Froude number Fr_{L}, the Weber number We_{V}, the Reynolds number Re_{TP}, and the Prandtl number Pr_{W} have been eliminated.

As indicated by Figure 4.2(a), in the low-quality region, the heat transfer coefficient is still underestimated, perhaps in consequence of the overvalued non-equilibrium effect. Since $(Nu_{\mathrm{c1}}/Nu_{\mathrm{m}})$ decreases with the increase of x_{e} at low-quality region, while it remains constant when x_{e} exceeds 0.4, a correction equation is proposed as a function of the equilibrium quality,

$$F_3 = \min\left[0.715(1-x_{\mathrm{e}})^{-0.678}, 1.0\right] \tag{4.18}$$

The modified Nusselt number will thereby be expressed by,

$$Nu_{\mathrm{c2}} = F_1 \cdot F_2 \cdot F_3 \cdot Nu_0 \tag{4.19}$$

In consequence, the distribution of the $(Nu_{\mathrm{c2}}/Nu_{\mathrm{m}})$ is analyzed again and displayed in Figure 4.3. As seen, the value of $(Nu_{\mathrm{c2}}/Nu_{\mathrm{m}})$ equals unity and further modification to Nu_{c2} seems not required.

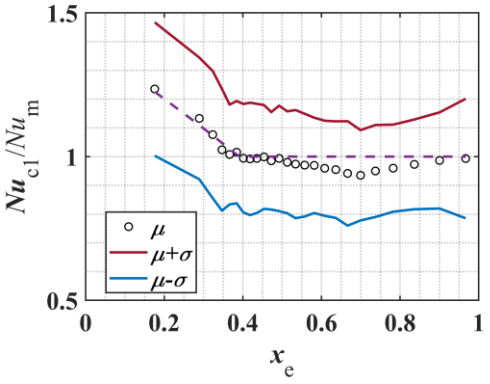

(a) Equlibrium quality x_{e}

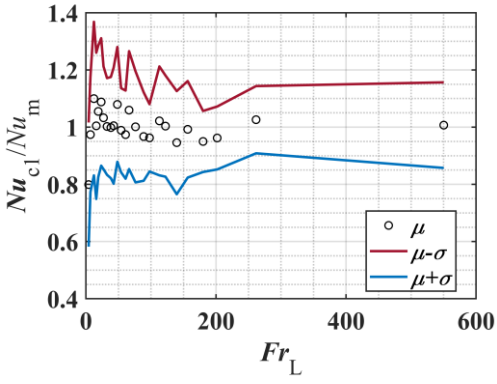

(b) Froude number Fr_{L}

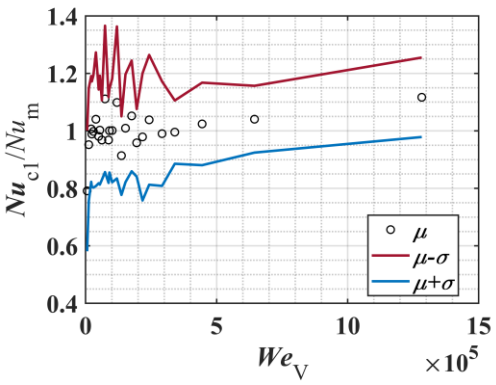

(c) Weber number

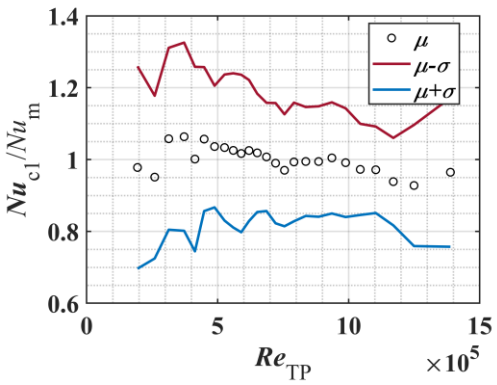

(d) Two-phase Reynolds number $\mathrm{Re}_{\mathrm{TP}}$

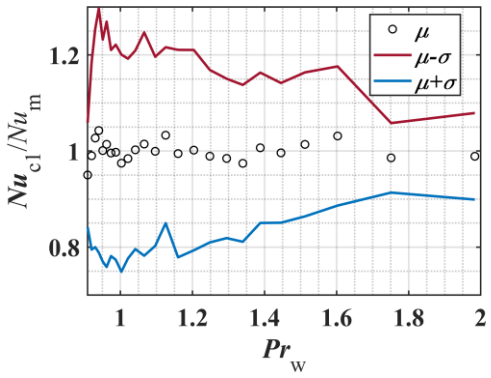

(e) Prandtl number

Figure 4.2.: Variation of Nu_{c1}/Nu_m versus dimensionless parameters

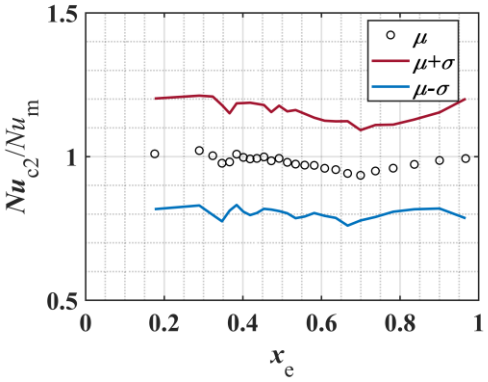

(a) Equlibrium quality x_e

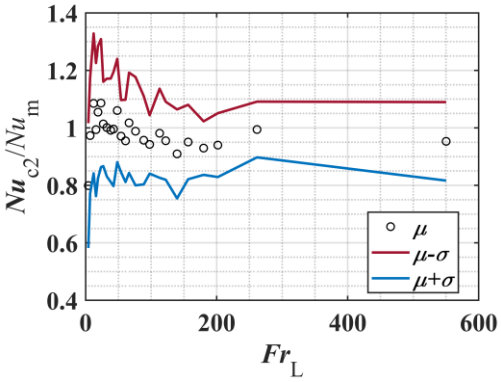

(b) Froude number $\mathrm{Fr_L}$

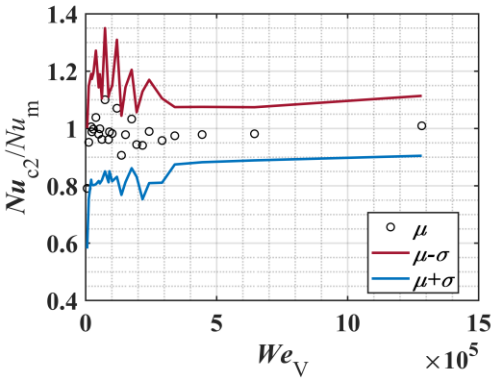

(c) Weber number

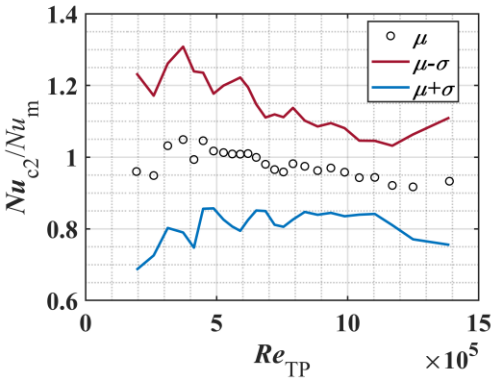

(d) Two-phase Reynolds number $\mathrm{Re_{TP}}$

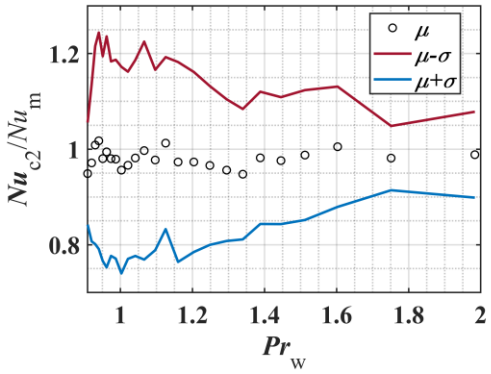

(e) Prandtl number

Figure 4.3.: Variation of Nu_{c2}/Nu_m versus dimensionless parameters

4.4. Assessment of Present PDO Heat Transfer Model

For the whole-pressure PDO heat transfer database (Table 4.3), which is applied to develop the present model, the distribution of error parameters (defined by Eq.(4.3)) with the variation of the pressure, mass flux, tube diameter, heat flux, quality, and wall superheat, are displayed in Figure 4.4. As can be seen, there is no drastic deviation along these system parameters. Although the heat transfer tends to be lower estimated when pressure is below about 12 MPa, systematic deviation in the interested pressure range, which is above 15.5 MPa with reduced pressure over 0.7, is not evidence. It could be demonstrated that the present heat transfer model for the stable PDO heat transfer region is reasonable.

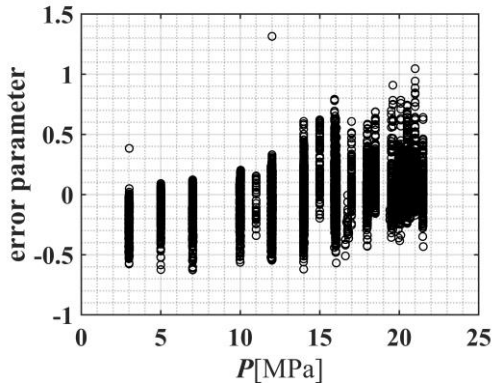

(a) Pressure

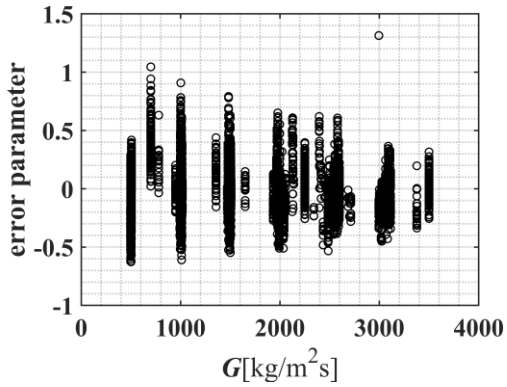

(b) Mass flux

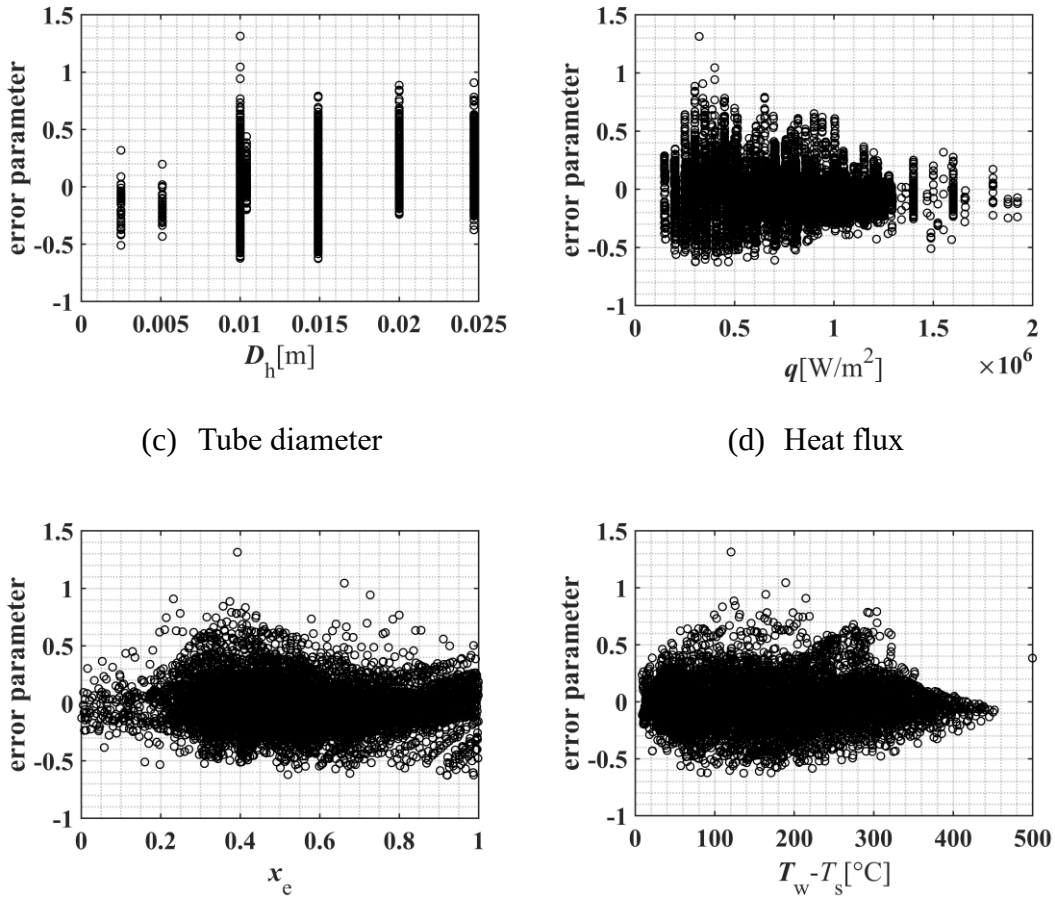

(c) Tube diameter (d) Heat flux

(e) Quality (f) Wall superheat

Figure 4.4.: Distribution of PDO heat transfer coefficient prediction error parameter

As shown in Table 4.4, for the whole-pressure water PDO heat transfer database, the present PDO heat transfer prediction model gives the mean error of -2.0% and the RMS error of 18.1%. The deviation of the Swenson correlation[136] is considerable, with mean error up to 83.3% and RMS error of 104.4%. The 2003 Post-CHF LUT[118] obtains mean error of -10.6% and RMS error of 20.9% for 7350 data points. It is indicated that the present PDO heat transfer correlation achieves a better accuracy than other prediction approaches listed in Table 2.2.

Furthermore, when applying the present PDO heat transfer correlation to the high-pressure water experiments, the mean error and RMS error are 2.3% and 17.6%, respectively. Compared to prediction accuracy of previous prediction methods summarized in Table 4.2, as seen, the present PDO heat transfer correlation provides a better accuracy for the high-pressure PDO heat transfer as well.

To sum up, compared to previous prediction approaches, the present PDO heat transfer correlation achieves a higher prediction accuracy for both the high-pressure and the whole-pressure water PDO heat transfer database. Additionally, for the whole-pressure

database, it covers reduced pressure from 0.135 to 0.975, Re_{TP} from 9.91×10^4 to 1.78×10^6, Pr_W from 0.89 to 2.46, and x_e from 0.001 to 0.999. For the high-pressure part of the PDO heat transfer database of which the reduced pressure is from 0.722 to 0.975, the range of Nu, Re_{TP}, and x_e is the same to the whole database, while Pr_W ranges from 0.93 to 2.46.

Table 4.4.: Prediction accuracy of different correlations for whole-pressure water PDO heat transfer databank

Model	*ME*	*SD*	*RMS*	No. of used data points
Present correlation	-0.020	0.180	0.181	9902
2003 Post-CHF LUT[118]	-0.106	0.180	0.209	7350
Miropol'skii[113]	0.398	0.496	0.636	9902
Slaughterbeck[135]	-0.174	0.166	0.241	9902
Groeneveld[111]	0.191	0.264	0.326	9902
Swenson[136]	0.833	0.629	1.044	9902

4.5. Validation of Present PDO Heat Transfer Model

4.5.1. Validation by High-Pressure CO_2 Experiment

Since the present PDO heat transfer correlation is dimensionless, it could be applied to different working fluids. Therefore, hereunder, the present correlation will be validated by heat transfer experiments carried out by Eter et al.[149], with CO_2 as coolant in uniformly heated tubes for the high-pressure region.

As listed in Table 4.5, the PDO heat transfer database for high-pressure CO_2 experiments in uniformly heated tubes contains 497 data points at a range of reduced pressure 0.88–0.95, Reynolds number Re_{TP} 9.26×10^4–4.83×10^5, Prandtl number Pr_W 0.76–1.25, and equilibrium quality x_e 0.003–0.965. Accordingly, Table 4.6 compares predictive capability of different prediction methods. For the present PDO heat transfer correlation, the mean error and RMS error are 7.9% and 28.9%, respectively. As indicated, the present heat transfer model shows a good adaptation to CO_2, though it is developed from water experiments.

When applied to high-pressure CO_2 experiments, the Miropol'skii correlation[113] obtains mean error of 103.5%. The Groeneveld correlation[111] achieves the mean error of 15.9% and RMS error of 27.5%. Since the 2003 Post-CHF LUT[118] can only be applied to water without fluid-to-fluid scaling and Slaughterbeck correlation[135] is not a dimensionless correlation, they could not be used for non-aqueous fluids and are not listed in Table 4.6. Aa seen, the present correlation exhibits advantage in prediction accuracy over other prediction methods.

Table 4.5.: Parameter ranges of the high-pressure PDO heat transfer measurements with CO_2 in uniformly heated tubes

Parameters	P [MPa]	P_r [-]	G [kg/(m^2·s)]	D_h [mm]	q [kW/m^2]
Min	6.49	0.88	497	8	59.8
Max	7.01	0.95	1991	8	225.2
Parameters	x_e [-]	$T_w - T_s$ [°C]	Nu [-]	Re_{TP} [-]	Pr_W [-]
Min	0.003	24.56	63.06	9.26×10^4	0.76
Max	0.965	213.12	681.70	4.83×10^5	1.25

Table 4.6.: Comparison of different prediction models for high-pressure uniformly heated CO_2 experiments

Model	*ME*	*SD*	*RMS*	No. of used data points
Present correlation	-0.079	0.278	0.289	497
Miropol'skii[113]	1.035	0.421	1.117	497
Groeneveld[111]	0.159	0.225	0.275	497
Swenson[136]	0.954	0.361	1.020	497

4.5.2. Validation by Non-uniformly Heated Water and Uniformly Heated R134a Experiment

Moreover, the present model is also validated by experiments in a lower pressure region, i.e., water experiments with non-uniform heating and R134a experiments with uniform heating, as listed in Table 4.7.

- Non-uniformly Heated Water Experiments

Concerning the "non-uniformly heated water" database, experiments of water in non-uniformly heated vertical round tubes were carried out by Becker et al.[98], made up of five different axial power profiles including inlet peak, middle peak, outlet peak, narrow middle peak, and narrow inlet peak. As summarized in Table 4.7, for the non-uniformly heated water database, the reduced pressure ranges from 0.045 to 0.727. It covers the range of Re_{TP} from 2.19×10^5 to 1.50×10^5, the range of Pr_W from 0.89 to 2.35, and the range of x_e from 0.003 to 0.965.

It can be found in the Table 4.8 that the mean error and RMS error of present PDO heat transfer model are -1.5% and 20.3%, respectively. In addition, the 2003 Post-CHF LUT[118] can only be utilized to predict 17550 non-uniformly heated water data points and obtains mean error and RMS error of 7.4% and 22.9%, respectively. The Slaughterbeck correlation[135] achieves the mean error of 5.5% and RMS error of 37.2%. It is obvious that the present correlation performs better than other prediction methods.

- Uniformly Heated R134a Experiments

Koeckert et al.[150] performed experimental study about post-dryout heat transfer with R134a as coolant in a uniformly heated vertical tube at the KIT Model Fluid Facility (KIMOF). The uniformly heated R134a database covers the reduced pressure range 0.27–0.694, Re_{TP} 1.37 × 10^5–7.79 × 10^5, Pr_{W} 0.78–0.95, and x_{e} 0.263–0.999. As can be seen in Table 4.8, the present heat transfer model obtains mean error of 2.7% and RMS error of 19.4%. The mean error and RMS error of the Groeneveld correlation[111] is only 0.7% and 16.0%, respectively, which performs slightly better than the present heat transfer model.

As can be concluded, when applied to the non-uniformly heated water experiments and uniformly heated R134a experiments, the present PDO heat transfer model could give a good prediction and is more accurate than other prediction methods.

Table 4.7.: Parameter ranges of non-uniformly heated water and uniformly heated R134a PDO heat transfer experiments

	Non-uniformly heated water (N=18895)		Uniformly heated R134a (N=2806)	
Parameters	min	max	min	max
P, MPa	0.99	16.03	1.10	2.82
P_r, -	0.045	0.727	0.270	0.694
G, kg/(m^2·s)	496.6	3117.9	294.6	1517.4
D_{h}, mm	15.0	15.0	10.0	10.0
q, kW/m^2	70.0	1587.0	24.8	139.8
x_{e}, -	0.129	0.999	0.263	0.999
$T_{\mathrm{w}} - T_{\mathrm{s}}$, ℃	3.74	540.82	30.81	190.81
Nu, -	157.41	1.74 × 10^4	162.66	688.49
Re_{TP}, -	2.19 × 10^5	1.50 × 10^5	1.37 × 10^5	7.79 × 10^5
Pr_{W}, -	0.89	2.35	0.78	0.95

Table 4.8.: Prediction accuracy of different prediction methods to non-uniformly heated water experiments and uniformly heated R134a experiments

	Non-uniformly heated water (N=18895)		Uniformly heated R134a (N=2806)	
Model	*ME*	*RMS*	*ME*	*RMS*
Present correlation	-0.015	0.203	0.027	0.194
2003 Post-CHF LUT[118]	0.074	0.229	-	-
Miropol'skii[113]	0.208	0.531	0.328	0.446
Slaughterbeck[135]	0.055	0.372	-	-
Groeneveld[111]	0.523	0.704	0.007	0.160
Swenson[136]	1.727	1.812	2.909	2.957

4.6. Parametric Trends of PDO Heat Transfer

In this section, the influence of pressure, mass flux, heat flux, and tube diameter are discussed, respectively, for PDO heat transfer experiments in uniformly heated round tubes at high-pressure region with water or CO_2 as coolant.

4.6.1. Effect of Pressure on PDO Heat Transfer

Comparison of PDO heat transfer under different pressure conditions could be found in Figure 4.5. The parameters for selected test cases are summarized in Table 4.9. Figure 4.5(a) and Figure 4.5(b) shows the variation of heat transfer coefficient versus the equilibrium quality, when the pressure increases from 16 MPa to 20 MPa for water experiments. Figure 4.5(c) compares the PDO heat transfer for uniformly heated round tubes with CO_2 at pressure of 6.49 MPa and 7.0 MPa, respectively. Moreover, the prediction results with Eq.(4.19) for each test case are plotted in Figure 4.5 as well. In general, the predicted heat transfer coefficient gets a good agreement with the experiment.

As observed, PDO heat transfer coefficient increases with increasing pressure. As the pressure increases, according to research of Kataoka et al.[144], the droplet diameter will be smaller with a lower surface tension, therefore the total interfacial area is larger at the same equilibrium quality. It facilitates the interfacial heat transfer from the vapor phase to liquid droplets. In consequence, a better total heat transfer could be obtained at a higher pressure.

Table 4.9.: Test cases for PDO heat transfer under different pressure

Case No.	Fluid	P [MPa]	P_r [-]	G [kg/(m^2·s)]	D_h [mm]	q [kW/m^2]
BEC98	water	15.99	0.72	1970.10	14.9	608.0
BEC57	water	17.99	0.82	1974.40	14.9	608.0
BEC18	water	19.92	0.90	1979.50	14.9	603.0
BEC95	water	16.00	0.73	2553.70	14.9	1151.0
BEC53	water	17.99	0.82	2548.00	14.9	1140.0
BEC14	water	20.03	0.91	2571.90	14.9	1119.0
GRO4	CO_2	6.49	0.88	703	8	79.9
GRO5	CO_2	7.00	0.95	703	8	79.9

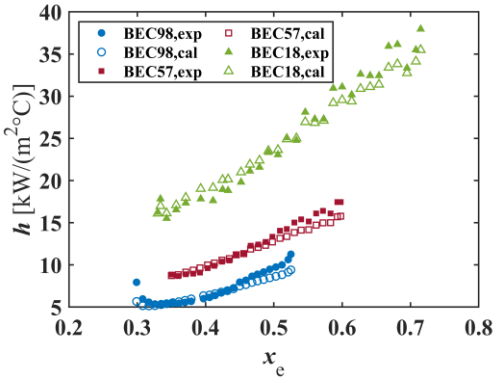

(a) Water experiments: G=2000 kg/(m^2·s), q= 600 kW/m^2

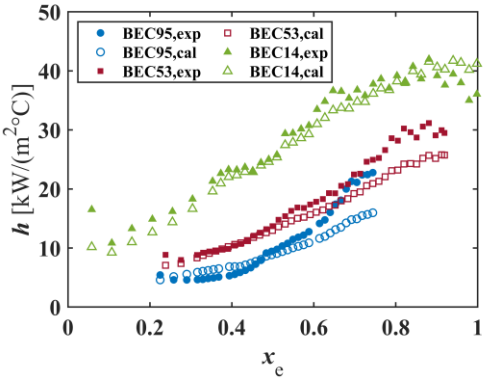

(b) Water experiments: G=2500 kg/(m^2·s), q= 1100 kW/m^2

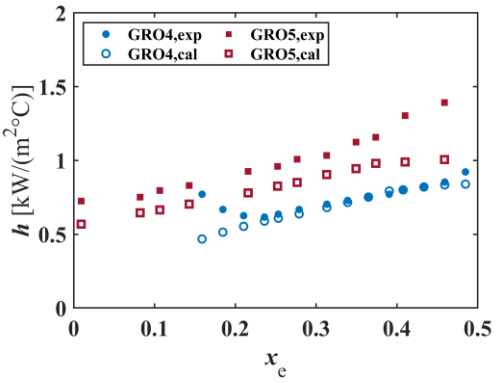

(c) CO_2 experiment: G=703 kg/(m^2·s), q= 79.9 kW/m^2

Figure 4.5.: Effect of pressure on PDO heat transfer

4.6.2. Effect of Mass Flux on PDO Heat Transfer

Test cases selected to investigate the mass flux influence on the PDO heat transfer are listed in Table 4.10. The first four cases are prepared for water experiments with pressure at 20 MPa and heat flux about 750 kW/m^2, which are shown in Figure 4.6(a).

Table 4.10.: Test cases for PDO heat transfer under different mass flux

Case No.	Fluid	P [MPa]	P_r [-]	G [kg/(m^2·s)]	D_h [mm]	q [kW/m^2]
BEC27	water	19.98	0.91	1485.30	14.9	748.0
BEC19	water	20.00	0.91	1991.10	14.9	749.0
BEC11	water	20.00	0.91	2566.70	14.9	741.0
BEC3	water	19.98	0.91	3082.50	14.9	742.0
GRO1	CO_2	6.56	0.89	500	8	97.9
GRO3	CO_2	6.56	0.89	700	8	96.2

Further, the experiments about CO_2 summarized in Table 4.10 can be seen from Figure 4.6(b), at the pressure of 6.56 MPa and heat flux of 97 kW/m^2. Obviously, the increase in mass flux leads to a better heat transfer since the vapor velocity is higher.

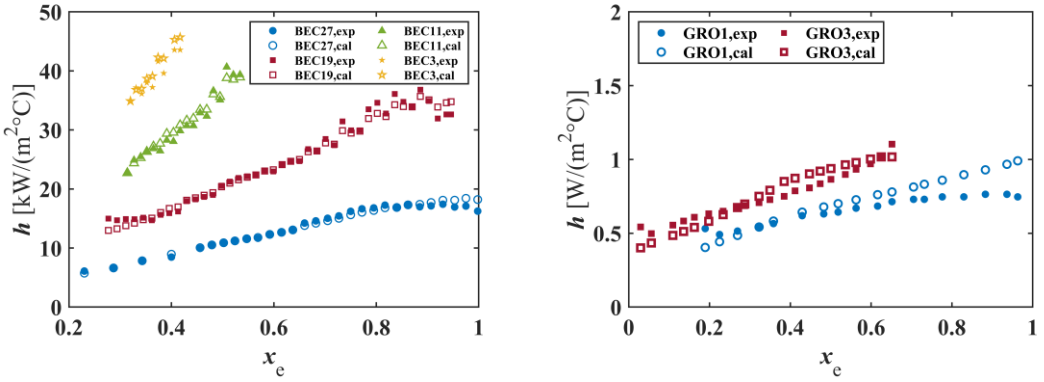

(a) Water experiment: P= 20 MPa, q= 750 kW/m^2

(b) CO2 experiment: P= 6.56 MPa, q=97 kW/m^2

Figure 4.6.: Effect of mass flux on PDO heat transfer

4.6.3. Effect of Heat Flux on PDO Heat Transfer

Regarding the effect of heat flux, test cases under different heat flux are listed in Table 4.11. Figure 4.7(a) shows the variation of heat transfer coefficient for water experiments when the heat flux increases from 742.0 kW/m^2 to 1218.0 kW/m^2, with pressure at 20 MPa and mass flux at around 3000 kg/(m^2·s). Figure 4.7(b) exhibits water experiments at a lower mass flux of 1500 kg/(m^2·s) with the range of heat flux from 500.0 kW/m^2 to 795.0 kW/m^2. Figure 4.7(a) and Figure 4.7(b) indicates the increasing heat transfer with decreasing heat flux.

Table 4.11.: Test cases for PDO heat transfer under different heat flux

Case No.	Fluid	P [MPa]	P_r [-]	G [kg/(m^2·s)]	D_h [mm]	q [kW/m^2]
BEC3	water	19.98	0.91	3082.50	14.9	742.0
BEC4	water	20.06	0.91	3084.50	14.9	837.0
BEC5	water	20.01	0.91	3103.90	14.9	931.0
BEC8	water	20.30	0.92	3061.60	14.9	1218.0
BEC24	water	19.99	0.91	1488.50	14.9	500.0
BEC25	water	19.99	0.91	1480.40	14.9	604.0
BEC27	water	19.98	0.91	1485.30	14.9	748.0
BEC28	water	19.97	0.91	1485.10	14.9	795.0
GRO2	CO_2	6.56	0.89	700	8	79.8
GRO3	CO_2	6.56	0.89	700	8	96.2

The higher heat flux implies higher interfacial heat flux, whereas the variation in heat flux does not influence the heat transfer coefficient between the vapor phase and droplets. Thereby, the increase in supplied heat flux will result in higher vapor superheat, which will impair the heat transfer between the heated wall and bulk flow.

For CO_2 experiments, as can be seen from Figure 4.7(c), when the heat flux rises from 79.8 kW/m^2 to 96.2 kW/m^2, there is no apparent difference on heat transfer coefficient.

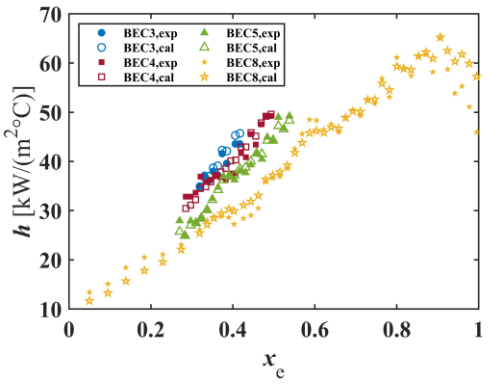

(a) Water experiment: P= 20 MPa, G=3000 kg/(m^2·s)

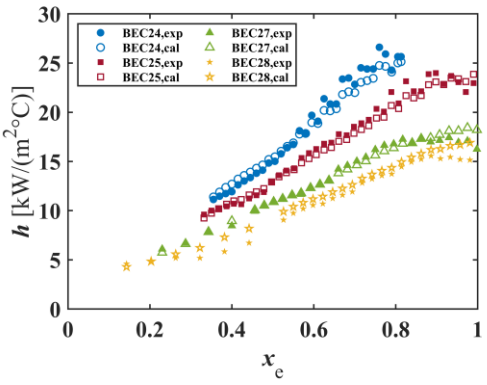

(b) Water experiment: P= 20 MPa, G=1500 kg/(m^2·s)

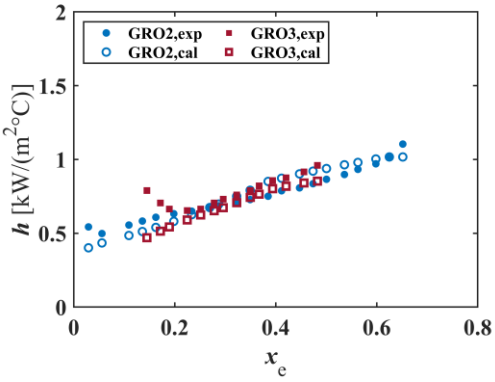

(c) CO_2 experiment: P= 6.56 MPa, G=700 kg/(m^2·s)

Figure 4.7.: Effect of heat flux on PDO heat transfer

4.6.4. Effect of Tube Diameter on PDO Heat Transfer

The effect of tube diameter is discussed hereunder. As summarized in Table 4.12, water experiments at constant pressure of 20 MPa, mass flux of 1500 kg/(m^2·s), heat flux of 604.0 kW/m^2, and in tubes with different diameter are compared. In general, as Figure 4.8 shows, the heat transfer increases when the tube diameter increases from 10 mm to 24.7 mm.

A larger tube diameter means higher value of Reynolds number and stronger flow turbulent, which could promote the vapor-droplet convective heat transfer. As a result, in the PDO regime, the heat transfer coefficient tends to be higher with a larger tube

diameter.

Table 4.12.: Test cases for PDO heat transfer under different tube diameters

Case No.	Fluid	P [MPa]	P_r [-]	G [kg/(m^2·s)]	D_h [mm]	q [kW/m^2]
BEC349	water	19.99	0.91	1507.40	10.0	597.0
BEC25	water	19.99	0.91	1480.40	14.9	604.0
BEC476	water	20.10	0.91	1493.00	24.7	598.0

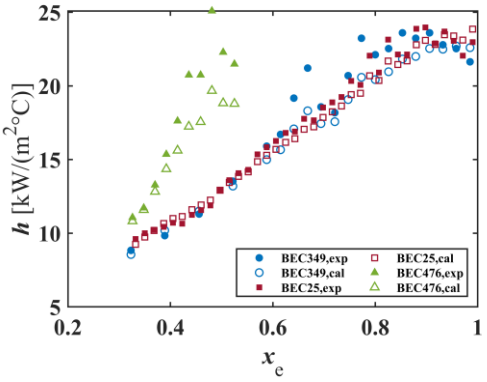

Figure 4.8.: Effect of tube diameter on PDO heat transfer

4.7. Summary

In this chapter, heat transfer in the post-dryout region is discussed. It is indicated that previous post-dryout heat transfer prediction approaches could not provide a reliable prediction to the high-pressure region. Thereby, a new PDO heat transfer correlation is developed by considering the two-phase mixture property effect, wall temperature effect, and non-equilibrium effect. The new PDO correlation is a combination of Re_{TP}, Pr_{W}, and the equilibrium quality x_{e}, expressed as,

$$Nu = F_1 \cdot F_2 \cdot F_3 \cdot (0.023 Re_{\mathrm{TP}}^{0.8} Pr_{\mathrm{w}}^{0.4})$$

with,

$$F_1 = 8.346 \times 10^{-03} Re_{\mathrm{TP}}^{0.319}$$

$$F_2 = \max\left(0.795 Pr_{\mathrm{W}}^{-1.752}, 0.809 Pr_{\mathrm{W}}^{1.287}\right)$$

$$F_3 = \min\left[0.715(1 - x_{\mathrm{e}})^{-0.678}, 1.0\right]$$

Derived from PDO heat transfer experiments in uniformly heated round tubes with upward flowing water as coolant, the validity range of the present PDO heat transfer correlation covers:

- Re_{TP}: $9.91 \times 10^4 \sim 1.78 \times 10^6$,

- Pr_{W}: 0.89 ~ 2.46
- x_{e}: 0.001 ~ 0.999

It has been demonstrated that the present correlation achieves better prediction accuracy against the high-pressure water PDO heat transfer experiments than previous prediction methods. Moreover, the present correlation achieves a good agreement when applied to high-pressure CO_2 experiments. Besides, the present correlation shows a good predictive capability to water experiments with non-uniform heating and R134a experiments with uniform heating.

As indicated, PDO heat transfer is facilitated as the increase of pressure, mass flux, and tube diameter. However, the PDO heat transfer becomes better under a lower heat flux.

5. Modification and Application of ATHLET-SC

The ATHLET-SC code is capable of simulation for trans-critical transients, since the discontinuity problem during the transition between the supercritical condition and subcritical two-phase condition has been solved by implementing the pseudo two-phase model. However, validation of trans-critical transient heat transfer experiment is still missing. In this chapter, the new CHF model and PDO heat transfer model developed in the present work will be implemented to ATHLET-SC to improve the prediction accuracy in the high-pressure region.

5.1. Introduction to ATHLET-SC Heat Transfer Model

Related information about heat transfer prediction models implemented in ATHLET-SC[44] are described below in respect of supercritical condition and subcritical condition.

Heat transfer correlations for the supercritical conditions are included in independent subroutines, in case the critical pressure exceeded, it will be utilized. Five heat transfer correlations for supercritical water, i.e., Bishop correlation[63], Krasnoshchekov correlation[64], Yamagata correlation[56], Jackson correlation[151], and Cheng correlation [57], were included and assessed. Referring to the literature review in Section 2.1, the Cheng correlation with given heat flux[62], seen in Eq.(2.10), is added and implemented for the prediction of heat transfer at supercritical pressures.

While for subcritical conditions, the heat transfer is determined using a complicated heat transfer logic controlled by numerous options[44]. Generally, it is separated to four main heat transfer regimes, i.e.,

- Level I: Heat flow from fluid to wall
- Level II: Heat flow from wall to fluid (forced and natural convection, Nucleate boiling (NB))
- Level III: Transition boiling (TB)
- Level IV: Film boiling (FB)

The Modified Chen correlation[152] and Chen correlation[153] are applied to subcooled and saturated nucleate boiling, respectively.

For film boiling region, the heat transfer coefficient is evaluated by post-CHF correlations, as Eq.(5.1) indicated. When the void fraction below 0.75, post-DNB correlations, i.e., Bromley correlation[106] or the Berenson correlation[107] will be utilized. For void fraction above 0.85, one of Modified Dougall-Rohsenow correlation[110], the Groeneveld correlation[111], and the Condie-Bengston IV correlation[112] will provide the PDO heat transfer coefficient. In the region with void fraction between 0.75 and 0.85, it will be obtained by cosine shape interpolation.

$$h_{\mathrm{FB}} = \begin{cases} h(\text{post-DNB}), \alpha \leq 0.75 \\ \text{interpolation}, 0.75 < \alpha \leq 0.85 \\ h(\text{post-dryout}), \alpha \geq 0.85 \end{cases} \tag{5.1}$$

Besides, the heat transfer coefficient for transition boiling is achieved by interpolation of nucleate boiling and the film boiling heat transfer coefficient.

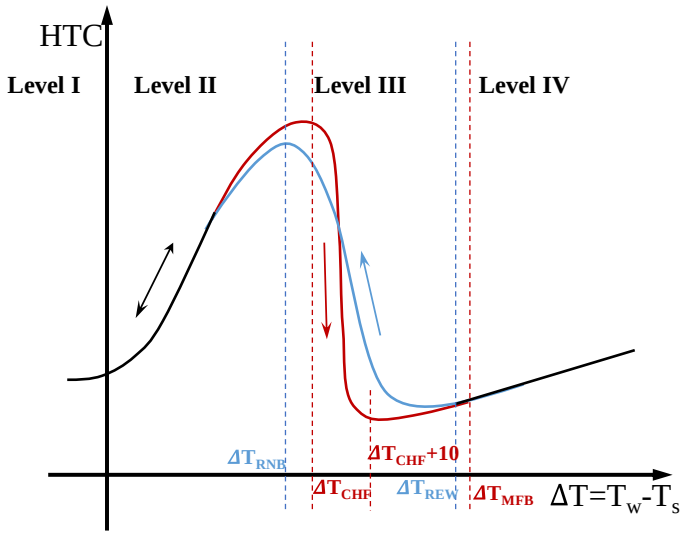

Figure 5.1.: Sketch of ATHLET-SC heat transfer logic[44]

The main part of the heat transfer logic could be simplified to Figure 5.1. The transfer from NB to TB is determined by the critical heat flux. ATHLET-SC provides eight CHF correlations for PWR and BWR simulations, i.e., W-3 correlation[80], Israel-Casterline-Matzner correlation[81], Hench-Levy correlation[154], Biasi correlation[155], Zuber-Griffith correlation[156], Hydropress correlation[157], Osmachkin correlation[158], and Mirshak correlation[159]. As concluded by GRS[44], the validated pressure range of the Osmachkin correlation[158] is the highest, which is up to 17 MPa.

In a heating process, the heat transfer turns to film boiling after the wall temperature above the minimum film boiling temperature (T_{MFB}). The Groeneveld-Stewart correlation[160] is implemented to compute the T_{MFB}. It has to be noted that this correlation is based on rewetting experiments at pressure up to 9 MPa. Conversely, for

the rewetting process, it is in another way, in which the heat transfer mode can only back to nucleate boiling when the wall temperature is lower than the rewetting temperature T_{REW}. By default, T_{REW} is 5 °C below T_{MFB}.

5.2. Preliminary Simulation of Trans-critical Transients by ATHLET-SC

Since ATHLET-SC is developed for supercritical water cooled system, the transient experiment carried out by Hu[34] in the Supercritical WAter MUltiPurpose loop (SWAMUP) will be simulated. However, simulation of other experiments which were performed with Freon as coolant and have been summarized in Section 1.2, could not be carried out so far. The information about Hu's experiments[34] and the ATHLET-SC simulation model is discussed hereunder.

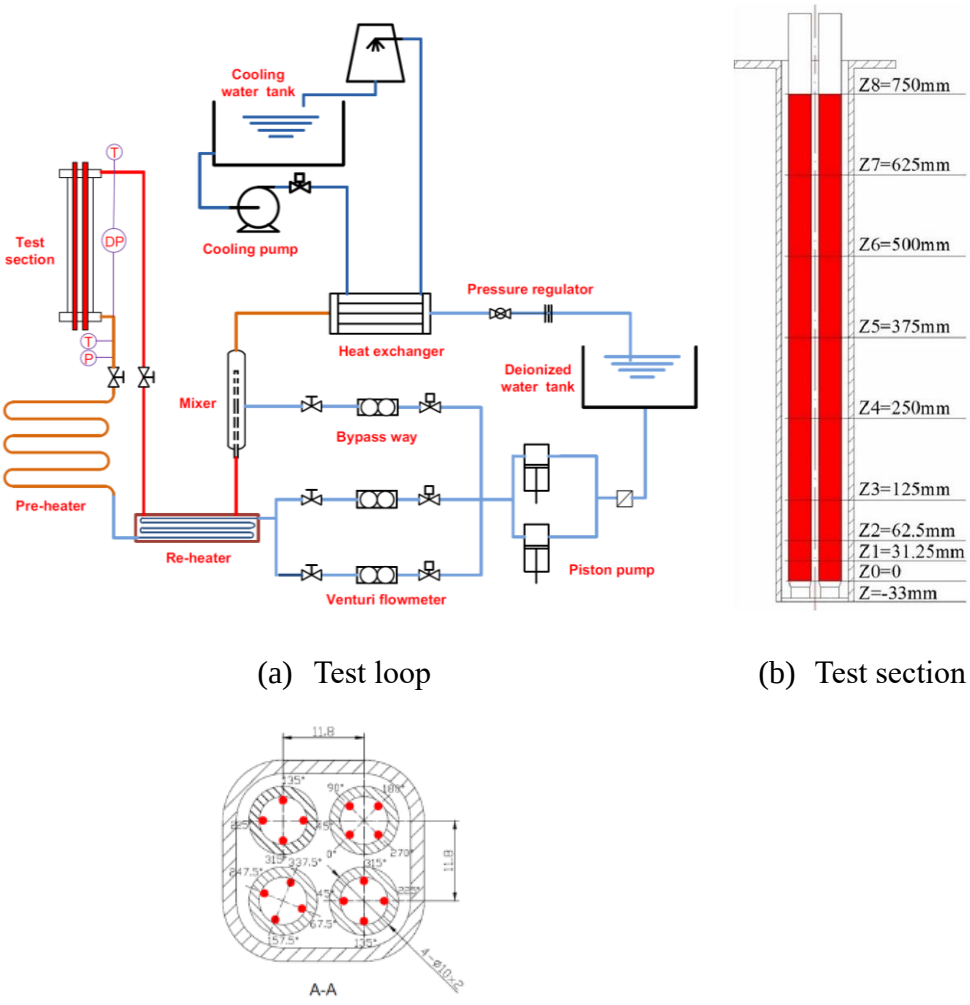

(a) Test loop (b) Test section

(c) Cross section

Figure 5.2.: Schematic of SWAMUP test loop and test section[161]

5.2.1. SWAMUP Test Facility and Experimental Procedure

SWAMUP test facility was established in Shanghai Jiao Tong University (SJTU), as Figure 5.2(a) shows, mainly containing the pre-heater, piston pump, mixer, and the test section. The design pressure is up to 30 MPa, the design temperature up to 550 °C, the mass flow rate up to 10.0 m^3/h, and the total power up to 1.2 MW[34, 161, 162].

For the trans-critical transient experiments performed on SWAMUP, the test section is displayed in Figure 5.2(b) and Figure 5.2(c). The 2×2 rod bundle heated by electric power is inserted into the assembly box and fixed by wrapping wire. The length of heated rod is 750 mm, and the outer diameter 10 mm. After reaching the pre-defined temperature, the deionized water flows upward into the test section to cooling the heating rods. As summarized in Table 5.1, during the pressure transient, the inlet mass flux, heat flux, and inlet enthalpy were kept constant. The system pressure decreases from 25 MPa to 17 MPa with a pressure change rate at 1 MPa/min. The wall temperature at eight different elevations (see Figure 5.2(b)) are recorded over time by thermocouples for every 0.2 second.

Table 5.1.: Test parameters of trans-critical experiments

Case ID	Pressure range (MPa)	Mass flux ($kg/m^2 \cdot s$)	Heat flux (kW/m^2)	Inlet enthalpy (kJ/kg)	Pressure change rate (MPa/min)
Case 1	25-17	885	424	1610	-1
Case 2	25-17	1297	604	1610	-1

5.2.2. ATHLET-SC Simulation Model

According to the experimental design, the ATHLET-SC simulation model has been established. Figure 5.3 shows the schematic of the simulation model, of which the geometry size is calculated from Figure 5.2(b) and Figure 5.2(c).

Referring to Hu's measurements[34], the inlet mass flux and enthalpy are kept constant, while the outlet is a time dependent volume (TDV) with given pressure. Four heated rods are applied with distance between rod centers at 11.8 mm. Corresponding to the elevations of thermocouples, the pipe is divided into ten control volumes. For each simulation, 100 seconds steady state calculation is carried out firstly at 25 MPa. Then the pressure decreases from 25 MPa to 17 MPa.

Especially, in the simulation, CHF will be evaluated as the minimum value of all eight CHF correlations. The selection of other heat transfer models obeys the default option in ATHLET-SC.

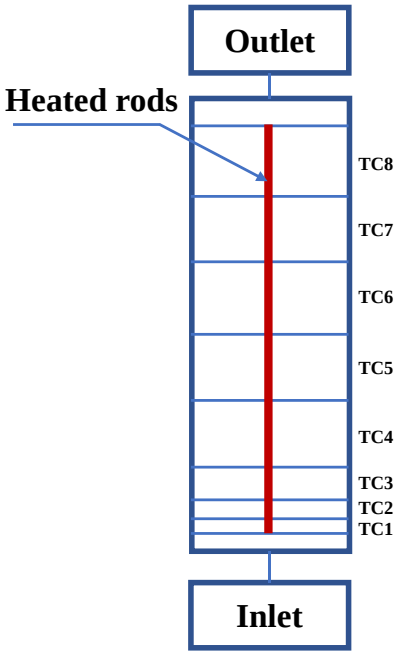

Figure 5.3.: Sketch of ATHLET-SC simulation model

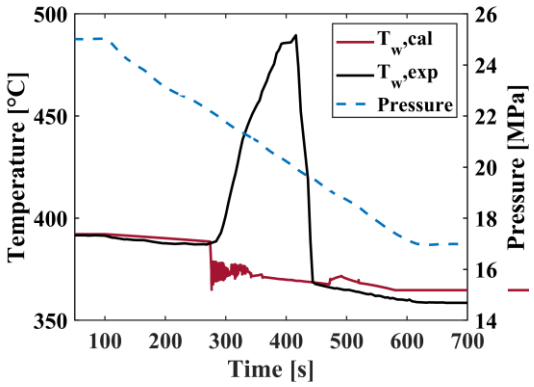

(a) Wall temperature

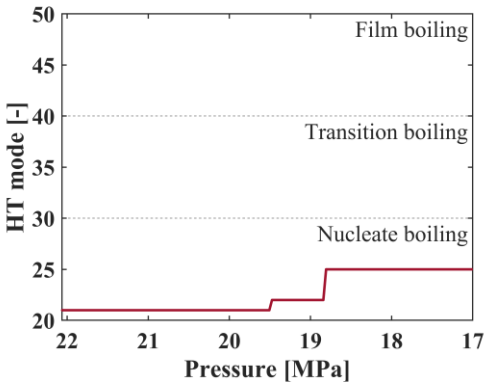

(b) HT mode

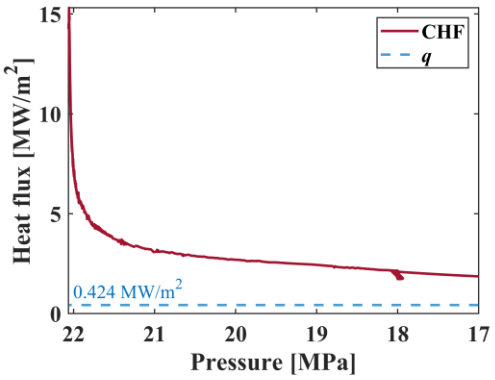

(c) Supplied heat flux vs CHF

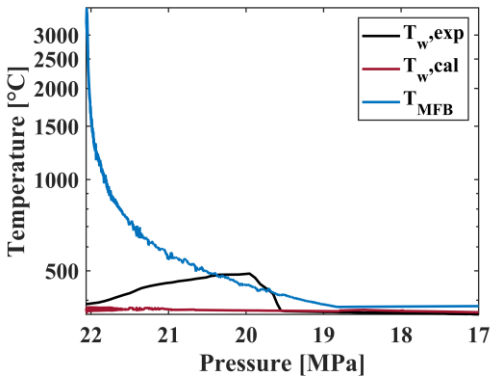

(d) Minimum film boiling temperature

Figure 5.4.: Simulated results with ATHLET-SC for Case 1

5.2.3. Preliminary Simulation Result

ATHLET-SC simulation results for the two cases in Table 5.1 are shown in Figure 5.4 and Figure 5.5, respectively.

In the supercritical condition, as indicated by the solid lines in Figure 5.4(a) and Figure 5.5(a), when the pressure reduces, the wall temperature drops systematically. The calculated wall temperature gets good agreement with measurement. Therefore, for a pressure transient, at supercritical conditions, the predictive capability of the Cheng correlation with given heat flux[62], seen in Eq.(2.10), gets proved.

In the subcritical condition, the characteristic of the heat transfer illustrated with experiments will be discussed firstly. As shown by the solid black line in Figure 5.4(a) and Figure 5.5(a), a sudden wall heat-up occurs when the pressure crosses the critical point. The wall temperature keeps increase when the system depressurized in the subcritical region. While as indicated by experiments, the hot wall could get rewetted at around 20 MPa in Case 1 and near 21 MPa in Case 2, respectively. Accordingly, the wall temperature drops to normal level again.

However, ATHLET-SC could not capture the heat transfer behavior in the subcritical

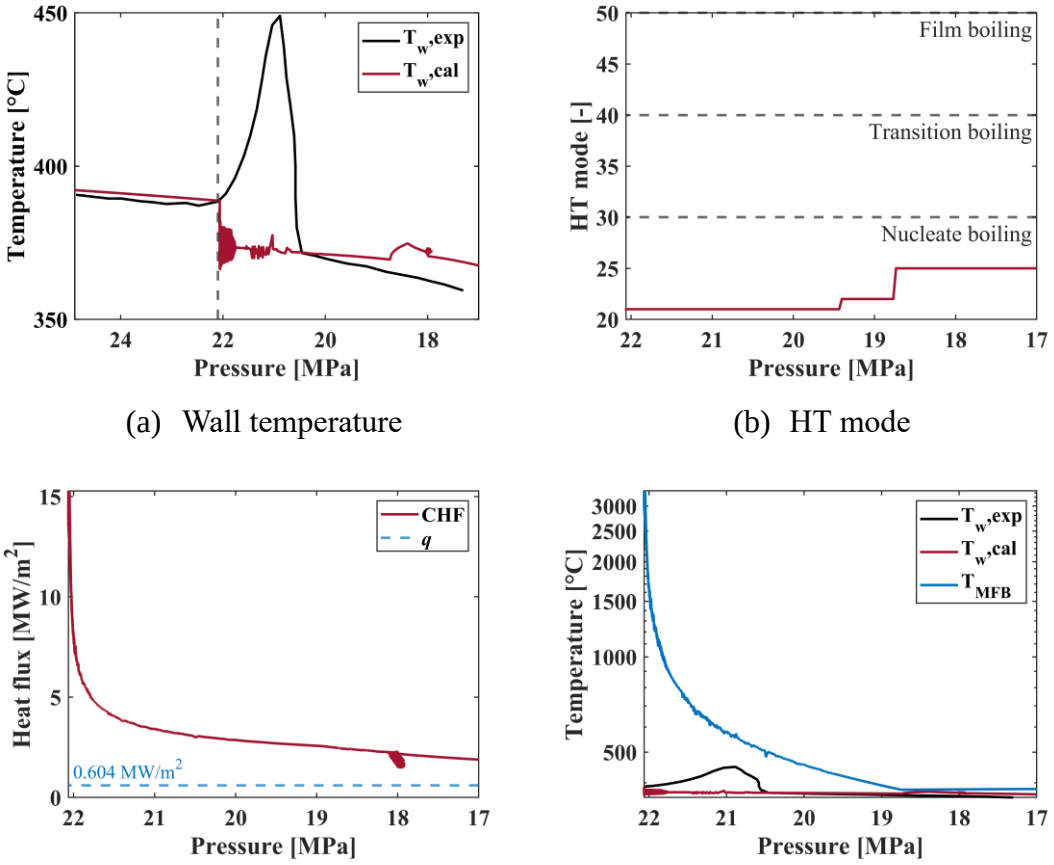

(a) Wall temperature (b) HT mode

(c) Supplied heat flux vs CHF (d) Minimum film boiling temperature

Figure 5.5.: Simulated results with ATHLET-SC for Case 2

region accurately. As can be seen from Figure 5.4(a), in the simulation for Case 1, the wall temperature remains at a low level, and there is no apparent wall heat-up as the experiment observed. Figure 5.4(b) shows that the simulated heat transfer mode stays in nucleate boiling region, with the index of heat transfer (HT) mode between twenty and thirty as ATHLET-SC defined. Further, Figure 5.4(c) plotted the value of CHF given by ATHLET-SC, which is assigned as the minimum value produced by all eight CHF correlations. As seen, the predicted CHF decreases during the pressure drops in the subcritical region. Since the supplied heat flux is always lower than CHF, the HT mode would not transfer from nucleate boiling to transition boiling. Since the minimum film boiling temperature is another crucial variable implemented in ATHLET-SC, which is as the boundary between the transition boiling and film boiling, the comparison of T_{MFB} and the wall temperature are provided in Figure 5.4(d). As indicated, the T_{MFB} is too high to be exceeded by the wall temperature, so the HT mode will not turn to film boiling regime. Thus, in comparison to the experiment, ATHLET-SC fails to predict the occurrence of the boiling crisis and the heated wall thus stays at a low temperature.

As Figure 5.5(a) shows, the simulation for Case 2 displays similar results with that for Case 1. In subcritical condition, as shown by Figure 5.5(b), the HT mode is in the nucleate boiling region. Therefore, the simulation does not display a sudden wall temperature increase after the pressure reduced to subcritical values. Besides, the variation of CHF and T_{MFB} predicted by ATHLET-SC are shown in Figure 5.5(c) and Figure 5.5(d), respectively. As seen, the supplied heat flux is lower than CHF. The heated wall temperature is below T_{MFB}. Hence, in the simulation, an apparent temperature rise of the heated wall is not observed during the depressurization transient.

5.3. Modification of ATHLET-SC

The simulation results given by ATHLET-SC imply that the heat transfer for supercritical pressures could be well predicted by the Cheng correlation with given heat flux[62]. While for the subcritical condition, it is confirmed that the prediction is unreliable since the CHF and T_{MFB} are overestimated by ATHLET-SC in the high-pressure region. Thereby, the heat transfer package in the subcritical condition will be modified.

CHF models implemented in ATHLET-SC are validated for safety analysis of PWR and BWR with pressure range below 17 MPa. Besides, as the preliminary simulation shows, seen from Figure 5.4 and Figure 5.5, even though the smallest heat flux given by the provided CHF models is used to calculated CHF, the value of CHF is still above the supplied heat flux. Therefore, the predicted HT mode stays in nucleate boiling region. The boiling crisis does not occur in the simulation. It proves that out of their validated pressure range, the predictive capability of CHF models used in ATHLET-SC are not sufficient. Consequently, the new correlation proposed in the present work, seen

Eq.(3.38), will be implemented.

Referring to the typical N-shaped boiling curve, the heat transfer condition turns from nucleate boiling to film boiling regime directly once the CHF is exceeded, unless the wall temperature could be controlled. Therefore, for the heating process, discussion about T_{MFB} is not necessary. Accordingly, the HT mode in ATHLET-SC would transfer from nucleate boiling to film boiling directly. Moreover, to simplify the simulation, the rewetting process is not considered.

Regarding to post-CHF heat transfer, the new PDO heat transfer correlation, Eq.(4.19), is added. Meanwhile, the selection of post-DNB and PDO is still determined by Eq.(5.1) according to the void fraction.

To sum up, the modification of ATHLET-SC is carried out in the following aspects,

(a) Implement of the new CHF correlation, i.e., Eq.(3.38);

(b) Implement of the new PDO heat transfer correlation, i.e., Eq.(4.19);

(c) Updating the heat transfer logic, i.e., allowing transfer from NB to FB directly when CHF is exceeded; and

(d) Exclusion of the rewetting process.

5.4. Simulation of Trans-critical Transient with Modified ATHLET-SC

With the modified ATHLET-SC, the trans-critical transients are calculated again. As shown in Figure 5.6(a) and Figure 5.7(a), the wall temperature starts to increase when the pressure drops to subcritical condition.

Figure 5.6 shows the simulation results of Case 1. Figure 5.6(c) implies that the predicted CHF increases along the pressure reduction. As seen, the supplied heat flux is above CHF. The HT mode therefore turns to film boiling. It must be noted that in this simulation, after the film boiling region encountered, post-DNB heat transfer correlation is selected by the default logic (see Eq.(5.1)), since the fluid is in high subcooled condition as indicated in Figure 5.6(b). Accordingly, the comparison of two post-DNB heat transfer correlations, i.e., Bromley correlation[106] and Berenson correlation[107], is displayed in Figure 5.6(a) in red curve and blue curve, respectively. Obviously, in the subcritical condition, the wall temperature increases systematically during the depressurization transient, which agrees with the experiment. However, the wall temperature is overestimated. Predicted by the Berenson correlation[107], it rises drastically and reaches up to 800 °C. As a comparison, the new PDO correlation is also applied for the trans-critical transient, although it is developed for the PDO heat transfer. The green line in the Figure 5.6(a) indicates that the new PDO correlation also

overestimate the wall temperature. In general, the Bromley correlation[106] provides the best prediction for Case 1.

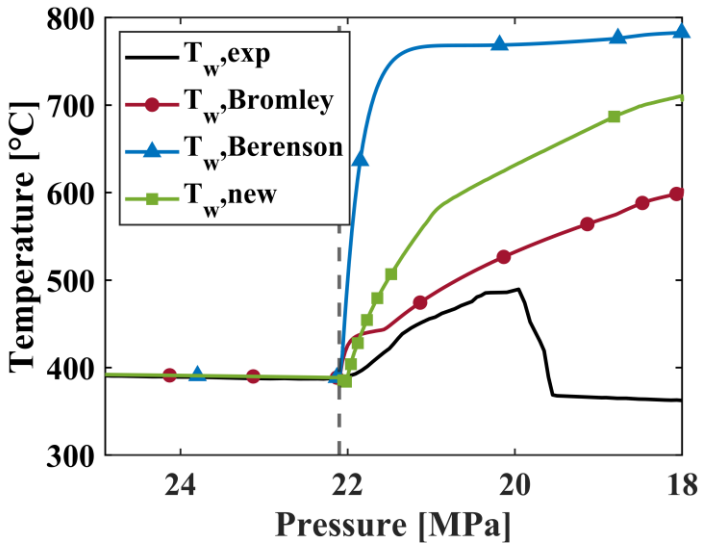

(a) Wall temperature

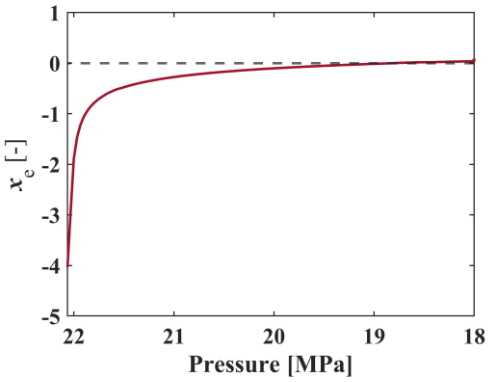

(b) Quality

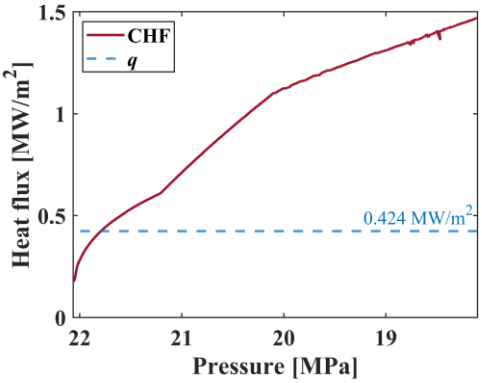

(c) Critical heat flux

Figure 5.6.: Simulation with the modified ATHLET-SC for Case 1

For the simulation of Case 2, as Figure 5.7(b)-Figure 5.7(c) shows, the variation of quality and CHF with the system pressure are similar to that for Case 1. Since the CHF is exceeded, the HT mode transfers to film boiling when the system pressure crosses the critical point. Consequently, the sudden wall temperature rise is observed in the simulation. Moreover, in the film boiling region, the wall temperature is also predicted by post-DNB heat transfer correlation. As the red line and blue line in Figure 5.7(a) illustrated, the predicted wall temperature is higher than the measurement. The maximum temperature given by the Berenson correlation[107] is even nearly 1000 °C. Besides, it is interesting to find that the prediction with the Bromley correlation[106] is consistent to that of the new PDO correlation.

In addition, since the rewetting process is excluded in the modified ATHLET-SC code,

the heated wall would not be rewetted during the depressurization procedure as observed in the experiment. According to the hysteresis phenomena of the boiling curve, the rewetting heat flux is usually below CHF. Further research about rewetting is required in the future.

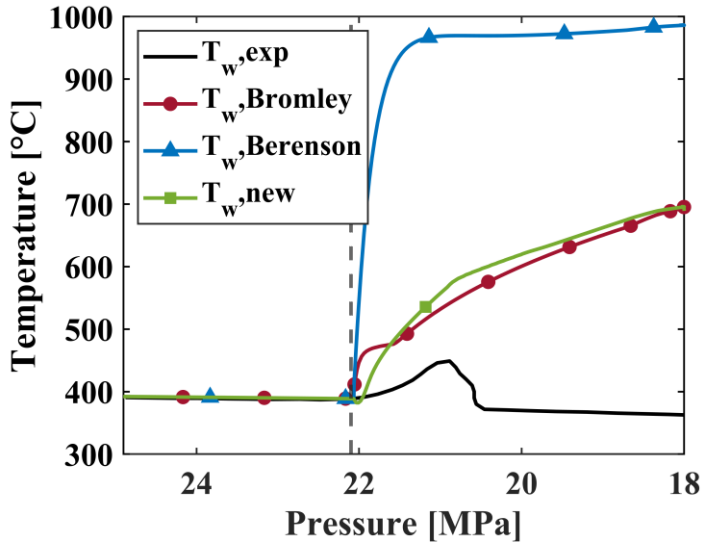

(a) Wall temperature

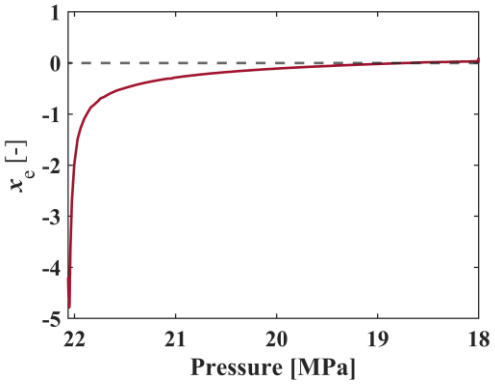

(b) Quality

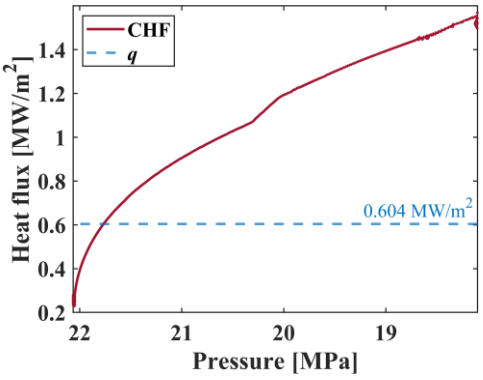

(c) Critical heat flux

Figure 5.7.: Simulation with the modified ATHLET-SC for Case 2

In general, the modified ATHLET-SC could predict the sudden wall temperature rise. After encountering the film boiling regime, post-DNB heat transfer correlation will be selected by default as the quality is low. It is indicated that the Berenson correlation[107] leads to an ultra-high temperature. The prediction with Bromley correlation[106] seems more reasonable but still insufficient. Since the new PDO heat transfer developed in the present work is for higher equilibrium quality region, it cannot give a reliable prediction to the current trans-critical depressurization transient.

As discussed before, post-DNB heat transfer experiments for the high-pressure region is unavailable so far. Therefore, to extend the post-DNB correlation to the high-pressure

region, relative experiments are required.

5.5. Simulation of Steady-State PDO Heat Transfer Experiment

Since current heat transfer experiments for trans-critical transient is in subcooled condition, as a supplement, the modified ATHLET-SC is applied to a steady-state PDO heat transfer experiment at high-pressure condition in order to assess the predictive capability of the new PDO heat transfer correlation.

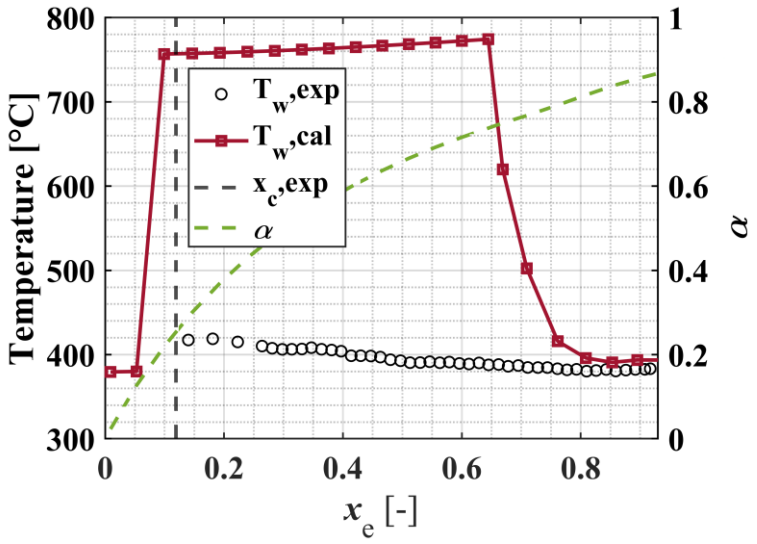

Figure 5.8.: Simulation of the steady-state PDO heat transfer experiment with the modified ATHLET-SC

The Becker's PDO heat transfer experiment was carried out with a uniformly heated round tube of diameter in 14.9 mm and length in 7 m. The experiment with water at pressure of 20.1 MPa, mass flux of 3079 kg/(m^2·s), heat flux of 1.112 MW/m^2 were simulated by the modified ATHLET-SC. Consequently, the simulation is compared with the experiment in Figure 5.8. The black dash line illustrates the measured critical quality.

For the simulation, the boiling crisis occurs when CHF is exceeded. Accordingly, the heat transfer mode turns to film boiling and the wall has a sudden heat-up. It is indicated that the predicted critical quality is a little bit lower. Therefore, the onset of boiling crisis predicted by the new CHF correlation is reliable.

According to Eq.(5.1), the Bromley correlation[106] is used to predict the wall temperature when the void fraction (the green dash line in Figure 5.8) is lower than 0.75. As seen, it overestimates the wall temperature. The simulation with Berenson correlation[107] is not exhibited in Figure 5.8 for the predicted temperature is so high

and out of the property package range. Moreover, the wall temperature drops when the void fraction becomes over 0.75. It indicates that the wall temperature predicted by PDO correlation gets better agreement with the experiment as the void fraction increases. Hence, the selection logic for post-CHF heat transfer provided by Eq.(5.1) is unreasonable. The void fraction criterion in Eq.(5.1) is thereby discarded. Supposing only the PDO correlation will be utilized after the film boiling region is encountered, while post-DNB correlation is abandoned, Figure 5.9 is thereby obtained. The green line in Figure 5.9 indicates that the simulation with the new PDO heat transfer correlation gets good agreement with the measurement.

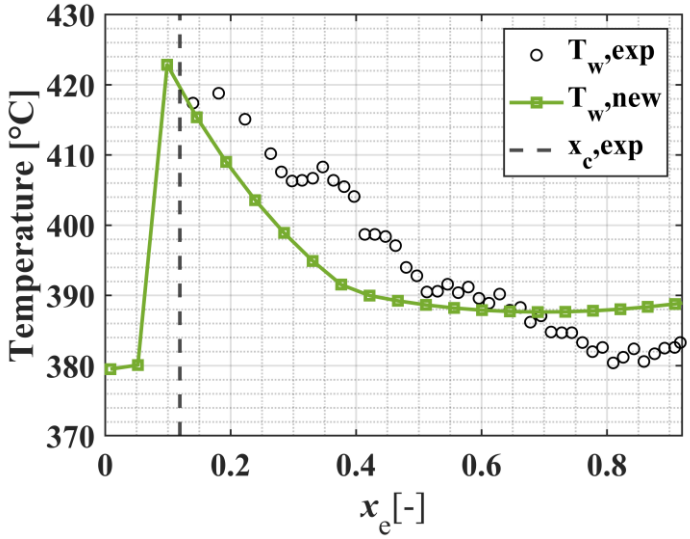

Figure 5.9.: Simulation of the steady-state PDO heat transfer experiment using the new PDO heat transfer correlation with the modified ATHLET-SC

5.6. Summary

The system thermal-hydraulic code ATHLET-SC is applied to simulate the trans-critical transient heat transfer experiments from Hu[34].

For supercritical condition, the wall temperature falls with the pressure reduction. The heat transfer behavior could be well predicted by the Cheng correlation[62], Eq.(2.10). However, as indicated by the preliminary simulation, the original ATHLET-SC code cannot predict the occurrence of boiling crisis as the pressure passes the critical point, since such high-pressure subcritical condition is out of the code's validity range.

Therefore, the new CHF model and new PDO heat transfer model are implemented to improve the prediction of CHF and post-CHF heat transfer in the high-pressure condition. With the modified ATHLET-SC, the sudden wall heat-up is observed in the simulation. After post-CHF regime encountered, the wall temperature increases as the pressure decreases. For current two experimental cases, since the system quality is low,

post-DNB heat transfer correlation is selected rather than the new PDO heat transfer correlation proposed in the present work. However, the wall temperature is significantly over predicted, which implies the predictive capability of post-DNB heat transfer is not sufficient. Since post-DNB heat transfer experiment for the high-pressure is unavailable up to now, a validated model for high-pressure post-DNB heat transfer has not been updated. Besides, applying the new PDO heat transfer correlation proposed in the present work, it is found that the predicted wall temperature is still higher than the measured value. The new PDO heat transfer correlation could not provide a good prediction accuracy to high-subcooled condition.

In general, the new CHF correlation covers a wider range of quality and could meet the requirement of the current trans-critical transient experiment cases. However, it is not the same for the new PDO correlation, which is developed for higher quality rather than for post-DNB heat transfer. Therefore, further research about high-pressure post-DNB heat transfer is required in the future.

Additionally, to test the new PDO heat transfer correlation, a steady state PDO heat transfer experiment with pressure at 20 MPa is simulated by the modified ATHLET-SC. It implies that the simulation with the new PDO heat transfer correlation is in good agreement with the measurement.

Besides, due to less knowledge of rewetting process, the trigger of rewetting is not included in the current work. Hence, the temperature drop following the heat-up is not observed in the simulation. Related research is required in the future.

6. Conclusions and Outlook

Supercritical power systems are possible to work under high-pressure subcritical conditions during some trans-critical procedures, when the system pressure transfers between supercritical and subcritical conditions. The low value of CHF in the high-pressure subcritical condition makes the occurrence of boiling crisis easier. Therefore, it is of great importance to carry out the heat transfer analysis of these trans-critical transient. For system thermal-hydraulic codes such as ATHLET, RELAP5, although some of them have been upgraded to the simulation of trans-critical transients, there remains deficiency of heat transfer models between 15.5 MPa to the critical point.

In the present work, heat transfer model for supercritical pressures, CHF model, and post-CHF heat transfer model are evaluated. Well validated prediction models are implemented in the ATHLET-SC code to simulate the trans-critical transient experiment.

6.1. Conclusions

Main conclusions can be drawn in the following aspects.

- Through literature review, knowledge of heat transfer for supercritical pressures is updated. It is noted that the heat transfer deterioration (HTD) phenomenon may lead to drastic temperature increase. Consequently, the recently developed Cheng correlation[62] with given heat flux is recommended, for it is based on an extended databank containing HTD cases and exhibits a better prediction accuracy than previous correlations. As demonstrated, when the Cheng correlations[62] is implemented in ATHLET-SC, the simulated wall temperature agrees well with the measurement in the trans-critical experiment.
- A CHF databank for high pressure has been established with experiments in uniformly heated round tubes. Compared against the high-pressure CHF databank (with reduced pressure above 0.7), existing prediction methods shows insufficient predictive capability.
- A new CHF correlation is developed based on the high-pressure water CHF databank. To identify the important dimensionless parameters, sublayer dryout model is taken into consideration for DNB. While at the dryout point, assume that

all the supplied heat is applied to evaporate the liquid film. Accordingly, a set of significant dimensionless parameters are identified. With the group-wise statistic method, a new CHF correlation is obtained by establishing the function between Boiling number, Weber number We_{V}, and quality, and expressed as,

$$Bo_{\mathrm{c}} = f(We_{\mathrm{V}}) \cdot f(x_{\mathrm{c}})$$

where,

$$f(We_{\mathrm{V}}) = \max(A_1, A_2)$$

$$f(x_{\mathrm{c}}) = (B_1 + B_2 + B_3) - \max(B_1, B_2, B_3) - \min(B_1, B_2, B_3)$$

and,

$$A_1 = 7.796 \times 10^{-2} \cdot We_{\mathrm{V}}^{-0.439}$$

$$A_2 = 1.530 \times 10^{-3} \cdot We_{\mathrm{V}}^{-0.0803}$$

$$B_1 = 2.156 \cdot (1 - x_{\mathrm{c}})^{0.688}$$

$$B_2 = 1.841 \cdot (1 - x_{\mathrm{c}})^{2.137}$$

$$B_3 = 0.672 \cdot (1 - x_{\mathrm{c}})^{0.219}$$

The new CHF correlation achieves mean error of 2% and RMS error of 37.4% in comparison with test data. The validity range of dimensionless parameters is,

We_{V}: 5.43× 10^2 ~ 2.67× 10^6,

x_{c}: -1.768 ~ 0.955.

- The new CHF correlation shows a good prediction accuracy for R12 and CO_2 experiments as well. For the high-pressure R12 CHF databank, the mean error and RMS error of the new CHF correlation are 2% and 33.3%, respectively. When applied to high-pressure CO_2, it obtains mean error of 6.8% and RMS error of 30.4%.
- Based on PDO heat transfer experiments with high-pressure water flowing in circular tubes, it is indicated that existing prediction methods of PDO heat transfer could not provide a satisfying predictive capability.
- A new PDO heat transfer correlation is developed using PDO heat transfer experiments in uniformly heated round tubes with water as coolant:

  $$Nu = F_1 \cdot F_2 \cdot F_3 \cdot (0.023 Re_{\mathrm{TP}}^{0.8} Pr_{\mathrm{w}}^{0.4})$$

  with,

  $$F_1 = 8.346 \times 10^{-03} Re_{\mathrm{TP}}^{0.319}$$

  $$F_2 = \max(0.795 Pr_{\mathrm{W}}^{-1.752}, 0.809 Pr_{\mathrm{W}}^{1.287})$$

  $$F_3 = \min[0.715(1 - x_{\mathrm{e}})^{-0.678}, 1.0]$$

  The new PDO correlation has the range of validity:

Re_{TP}: $9.91 \times 10^4 \sim 1.78 \times 10^6$,

Pr_W: 0.89 ~ 2.46,

x_e: 0.001 ~ 0.999.

The new PDO heat transfer correlation gets mean error of 2.3% and the RMS error of 17.6% for the high-pressure water databank.

- The new PDO heat transfer correlation is well validated by the high-pressure CO_2 databank, with mean error 7.9% and RMS error 28.9%. Moreover, it obtains mean error and RMS error of -1.5% and 20.3% for the non-uniformly heated water databank, mean error 2.7% and RMS error 19.4% for the uniformly heated R134a databank, respectively.
- The STH code ATHLET-SC is modified by implementing the new CHF correlation and new PDO heat transfer correlation. As indicated by the simulation of the trans-critical depressurization transient with the modified ATHLET-SC code, the wall heat-up is observed when the pressure passes the critical point and the heated wall temperature keeps increase as the pressure falls in the subcritical condition, which is the same to experimental results. However, in the post-CHF region, the wall temperature is overestimated by the new PDO correlation since the experiment is in subcooled condition but out of the validity range of the present PDO correlation.

6.2. Outlook

The present work developed CHF model and PDO heat transfer model for the high-pressure condition. However, there are still some works related to the trans-critical transient should be carried out in the future:

- Post-DNB heat transfer experiments in the high-pressure region,
- Trans-critical transient experiments with higher outlet quality, and
- Further research about rewetting.

Appendix

A. High-Pressure CHF Prediction Methods

A.1. Miropol'skii Correlation[103]

$$\frac{q_c \mu_{\mathrm{L}}}{\sigma \rho_{\mathrm{L}} H_{\mathrm{VL}}} = \begin{cases} \frac{0.174}{3600}\left(\frac{c_{p,\mathrm{L}} T_{\mathrm{sat}}}{H_{\mathrm{VL}}}\right)^{0.8} K^{0.4}\left[1 - 0.45\left(\frac{\rho_{\mathrm{L}}}{\rho_{\mathrm{V}}}\right)^{0.8} x_{\mathrm{c}}\right], x_{\mathrm{c}} < 0 \\ \frac{0.174}{3600}\left(\frac{c_{p,\mathrm{L}} T_{\mathrm{sat}}}{H_{\mathrm{VL}}}\right)^{0.8} K^{0.4}(1 - x_{\mathrm{c}})^{n}, x_{\mathrm{c}} \geq 0 \end{cases} \quad \text{(A.1)}$$

Where,

$$K = \left(\frac{G\mu_{\mathrm{L}}}{\sigma \rho_{\mathrm{L}}}\right)\left(\frac{\rho_{\mathrm{L}}}{\rho_{\mathrm{V}}}\right)^{0.2}$$

$$\mathrm{n} = \begin{cases} 0.8, \mathrm{K} \leq 0.016 \\ 50\mathrm{K}, 0.016 < \mathrm{K} \leq 0.06 \\ 3, \mathrm{K} > 0.06 \end{cases}$$

A.2. Levitan Correlation[101]

$$q_{\mathrm{c}} = 10^6(10.3 - 17.5P_{\mathrm{r}} + 8.0P_{\mathrm{r}}^2)\left(\frac{G}{1000}\right)^{0.68P_{\mathrm{r}} - 1.2x_{\mathrm{c}} - 0.3} \exp(-1.5x_{\mathrm{c}})\left(\frac{0.008}{D}\right)^{0.5} \quad \text{(A.2)}$$

A.3. Chernobai Correlation[102]

$$\frac{8D_*}{Re_{\mathrm{L}} Pr_{\mathrm{L}}}\left(1 + \frac{1.8H_{\mathrm{L}}}{H_{\mathrm{VL}}}\right)\left(1 + \frac{D_*}{Nu_{\mathrm{L}}}\right) = \begin{cases} \left(Bo + \frac{x_{\mathrm{c}} Nu_{\mathrm{L}}}{Re_{\mathrm{L}} Pr_{\mathrm{L}}}\right)^2, x_{\mathrm{c}} < 0 \\ Bo + \frac{2x_{\mathrm{c}} Nu_{\mathrm{L}}}{Re_{\mathrm{L}} Pr_{\mathrm{L}}}, x_{\mathrm{c}} \geq 0 \end{cases} \quad \text{(A.3)}$$

where,

$$D_* = 10\left(\frac{D_*}{0.004}\right)^{0.5},$$

$$Nu_{\mathrm{L}} = \frac{\left(\frac{f}{2}\right) Re_{\mathrm{D}} Pr_{\mathrm{L}}}{1.07 + 12.7\left(\frac{f}{2}\right)^{0.5}\left(Pr_{\mathrm{L}}^{\frac{2}{3}} - 1\right)}$$

$$f = [1.58\ln(Re_{\mathrm{L}}) - 3.28]^{-2}$$

A.4. Chen Correlation[97]

$$q_{\mathrm{c}} = \frac{[1 - 0.00216(GH_{\mathrm{VL}})^{0.25}]\,(1 - x_{\mathrm{c}})GD_{\mathrm{h}}H_{\mathrm{VL}}}{4L} \tag{A.4}$$

A.5. Becker Correlation[98]

$$q_{\mathrm{c}} = \frac{G(450 + \Delta H_{\mathrm{in}})}{40\frac{L}{D_{\mathrm{h}}} + 156G^{0.45}}\left[1.02 - \left(\frac{P}{P_{\mathrm{r}}} - 0.54\right)^{2}\right] \tag{A.5}$$

A.6. Hall Correlation[79]

$$Bo = 0.0722We_{\mathrm{L}}^{-0.312}\left(\frac{\rho_{\mathrm{L}}}{\rho_{\mathrm{V}}}\right)^{-0.644}\left[1 - 0.9\left(\frac{\rho_{\mathrm{L}}}{\rho_{\mathrm{V}}}\right)^{0.724}x_{\mathrm{c}}\right] \tag{A.6}$$

A.7. Lombardi Correlation[99]

$$q_{\mathrm{c}} = \frac{G\Delta H_{\mathrm{in}}}{4\left[\frac{L}{D_{\mathrm{h}}} + 2\left(\frac{0.5G^{2}}{\rho_{\mathrm{L}}}\right)^{0.5}D_{\mathrm{h}}^{0.4}\right]} \tag{A.7}$$

A.8. Kariya Correlation[94]

$$Bo = \begin{cases} Bo_{\mathrm{F1}}, Bo_{\mathrm{F1}} > Bo_{\mathrm{F2}} \\ Bo_{\mathrm{D2}}, Bo_{\mathrm{F1}} \le Bo_{\mathrm{F2}} \text{ and } Bo_{\mathrm{F2}} \ge Bo_{\mathrm{D1}} \text{ and } Bo_{\mathrm{F2}} \ge Bo_{\mathrm{D2}} \\ Bo_{\mathrm{F2}}, Bo_{\mathrm{F1}} \le Bo_{\mathrm{F2}} \text{ and } Bo_{\mathrm{F2}} \ge Bo_{\mathrm{D1}} \text{ and } Bo_{\mathrm{F2}} < Bo_{\mathrm{D2}} \\ Bo_{\mathrm{D2}}, Bo_{\mathrm{F1}} \le Bo_{\mathrm{F2}} \text{ and } Bo_{\mathrm{F2}} < Bo_{\mathrm{D1}} \text{ and } Bo_{\mathrm{D1}} \ge Bo_{\mathrm{D2}} \\ Bo_{\mathrm{D1}}, Bo_{\mathrm{F1}} \le Bo_{\mathrm{F2}} \text{ and } Bo_{\mathrm{F2}} < Bo_{\mathrm{D1}} \text{ and } Bo_{\mathrm{D1}} < Bo_{\mathrm{D2}} \end{cases} \tag{A.8}$$

Where,

$$Bo_{\mathrm{F1}} \times 10^{4} = \begin{cases} -10.6(x_{\mathrm{c}} - 0.1), for\ R22\ and\ R134A \\ -18.1(x_{\mathrm{c}} - 0.1), for\ water \end{cases}$$

$$Bo_{\mathrm{F2}} \times 10^{4} = -5.43\left(\frac{\rho_{\mathrm{L}}}{\rho_{\mathrm{V}}}\right)^{-0.47}\left(\frac{\rho_{\mathrm{L}}\sigma}{G^{2}D_{\mathrm{h}}}\right)^{0.082}\left(\frac{GD}{\mu_{\mathrm{L}}}\right)^{0.08}x_{\mathrm{c}} + 5.17\left(\frac{\rho_{\mathrm{L}}}{\rho_{\mathrm{V}}}\right)^{-1.87}\left(\frac{\rho_{\mathrm{L}}\sigma}{G^{2}D_{\mathrm{h}}}\right)^{0.35}\left(\frac{GD_{\mathrm{h}}}{\mu_{\mathrm{L}}}\right)^{0.3}$$

$$Bo_{\mathrm{D1}} \times 10^{4} = -1.62x_{\mathrm{c}} + 5.13\left(\frac{\rho_{\mathrm{L}}}{\rho_{\mathrm{V}}}\right)^{-0.64}\left(\frac{\rho_{\mathrm{L}}\sigma}{G^{2}D_{\mathrm{h}}}\right)^{0.39}\left(\frac{GD_{\mathrm{h}}}{\mu_{\mathrm{L}}}\right)^{0.36}$$

$$Bo_{\mathrm{D2}} \times 10^4 = 4.74 \left(\frac{\rho_{\mathrm{L}}}{\rho_{\mathrm{V}}}\right)^{0.83} x_{\mathrm{c}} \left(\frac{1}{x_{\mathrm{c}}} - 1\right)^{2.5}$$

A.9. Vijayarangan Correlation[95]

$$Bo = 0.0051 \left(\frac{\rho_{\mathrm{L}}}{\rho_{\mathrm{V}}}\right)^{-0.133} \left(\frac{\rho_{\mathrm{L}}\sigma}{G^2 L}\right)^{1/3} \times \left(\frac{1}{1 + 0.0031 \frac{L}{D_{\mathrm{h}}}}\right) P_{\mathrm{r}}^{0.147} Re_{\mathrm{L}}^{0.25} \tag{A.9}$$

A.10. Shah Correlation[96]

$$Bo = F_{\mathrm{E}} \cdot F_{\mathrm{x}} \cdot Bo_0 \tag{A.10}$$

Where,

$$F_{\mathrm{E}} = \max\left(1.54 - 0.032 \frac{L_{\mathrm{c}}}{D_{\mathrm{h}}}, 1\right)$$

$$\mathrm{Bo}_0 = \max\left(15\mathrm{Y}^{-0.612}, 0.082\mathrm{Y}^{-0.3}(1 + 1.45\mathrm{P}_{\mathrm{r}}^{4.03}), 0.0024\mathrm{Y}^{-0.105}(1 + 1.15 P_{\mathrm{r}}^{3.39})\right)$$

$$Y = G^{1.8} D_{\mathrm{h}}^{0.6} \left(\frac{c_p}{\lambda_{\mathrm{L}} \rho_{\mathrm{L}}^{0.8} g^{0.4}}\right) \left(\frac{\mu_{\mathrm{L}}}{\mu_{\mathrm{V}}}\right)^{0.6}$$

$$\begin{cases} x_{\mathrm{c}} \le 0, F_{\mathrm{x}} = F_3 \left[1 + \frac{\left(F_3^{-0.29} - 1\right)(P_{\mathrm{r}} - 0.6)}{0.35}\right]^c \\ x_{\mathrm{c}} > 0, F_{\mathrm{x}} = F_1 \left[1 - \frac{(1 - F_2)(P_{\mathrm{r}} - 0.6)}{0.35}\right]^b \end{cases}$$

$$c = \begin{cases} 0, P_{\mathrm{r}} \le 0.6 \\ 1, P_{\mathrm{r}} > 0.6 \end{cases}$$

$$F_3 = \left(1.25 \times \frac{10^5}{Y}\right)^{0.833 x_{\mathrm{c}}}$$

$$b = \begin{cases} 0, P_{\mathrm{r}} \le 0.6 \\ 1, P_{\mathrm{r}} > 0.6 \end{cases}$$

$$F_1 = \begin{cases} 1 + 0.0052(-x_{\mathrm{c}}^{0.88}) Y^{0.41}, Y \le 1.4 \times 10^7 \\ 1 + 0.0052(-x_{\mathrm{c}}^{0.88})(1.4 \times 10^7)^{0.41}, Y > 1.4 \times 10^7 \end{cases}$$

$$F_2 = \begin{cases} F_1^{-0.42}, F_1 \le 4 \\ 0.55, F_1 > 4 \end{cases}$$

B. Chauvenet's Criterion

n	2	3	4	5	6	7	8	9	10	12	14
T(n)	1.15	1.38	1.54	1.65	1.73	1.8	1.86	1.92	1.96	2.03	2.1
n	16	18	20	22	24	26	30	40	50	100	200
T(n)	2.15	2.2	2.24	2.28	2.31	2.35	2.39	2.5	2.58	2.8	3.02

n: total number in the tested group

T(n): maximum acceptable value

C. Details of the CHF Data Bank

Reference	Fluid	No. of data points	P, MPa		G, kg/m^2		D_h, m		x_c, -		q_c, kW/m^2		P_r, -	
			min	max	min	max	min	max	min	max	min	max	min	max
Becker,1971[163]	water	571	16	20	156	6907	0.0100	0.0100	-0.866	0.955	135	3679	0.73	0.91
Smolin, 1965[164]	water	43	17.7	19.6	600	4700	0.0104	0.0104	-0.090	0.450	700	1860	0.80	0.89
Hein, 1979[165]	water	24	17.4	21.5	472	2535	0.0140	0.0140	-0.580	0.660	260	610	0.79	0.97
Becker, 1983[129]	water	168	15.9	20.3	497.8	3106.5	0.0100	0.0247	0.027	0.612	146	1240	0.72	0.92
Chen, 2017[97]	water	31	18.3	20.2	460	3928.5	0.0046	0.0109	-1.716	0.270	935	7770	0.83	0.92
Chen, 2016[166]	water	21	18.3	20.2	1140	3928.5	0.0046	0.0109	-1.768	-0.332	1840	7310	0.83	0.92
Herkenrath, 1967[167]	water	118	17	21.5	700	3500	0.0100	0.0200	-0.924	0.474	200	1600	0.77	0.97
Kiameh, 1986[168]	water	4	17.2	20	394	1982	0.0019	0.0100	-0.538	0.360	848	2839	0.78	0.91
Epstein, 1956[169]	water	58	17.2	19.0	1844.5	3783.9	0.0191	0.0191	-0.395	0.044	2082	6056.8	0.78	0.86
Peskov, 1969[170]	water	119	16	20	594.44	5444.4	0.0080	0.0085	0.000	0.334	612.9	3582	0.73	0.91
IATF, 2019[137]	water	161	16	21.5	283	3500	0.0051	0.0200	-0.961	0.574	151	1800	0.73	0.97
Thompson,1964[171]	water	166	15.5	20.7	793.4	3879	0.0019	0.0036	-1.131	0.047	1104	6592	0.70	0.94
IATF, 2019[137]	R12	1140	2.9	3.5	121	10440	0.0030	0.0158	-0.745	0.902	18	991	0.70	0.85
Eter, 2017[149]	CO_2	28	6.19	7.05	494	2041	0.008	0.008	-0.771	0.294	53.6	225.2	0.84	0.96

D. Details of PDO Heat Transfer Prediction Methods

D.1. Miropol'skii Correlation[113]

$$h = 0.023\frac{\lambda_{\mathrm{V}}}{D_{\mathrm{h}}}\left[\frac{GD_{\mathrm{h}}}{\mu_{\mathrm{V}}}\left(x_{\mathrm{e}} + \frac{\rho_{\mathrm{V}}}{\rho_{\mathrm{L}}}(1 - x_{\mathrm{e}})\right)\right]^{0.8} Pr_{\mathrm{w}}^{0.8} Y \tag{D. 1}$$

where,

$Y = 1 - 0.1\left(\frac{\rho_{\mathrm{L}}}{\rho_{\mathrm{V}}} - 1\right)^{0.4}(1 - x_{\mathrm{e}})^{0.4}$

D.2. Slaughterbeck Correlation[135]

$$h = 1.604 \times 10^{-4}\frac{\lambda_{\mathrm{V}}}{D_{\mathrm{h}}}\left[\frac{GD_{\mathrm{h}}}{\mu_{\mathrm{V}}}\left(x_{\mathrm{e}} + \frac{\rho_{\mathrm{V}}}{\rho_{\mathrm{L}}}(1 - x_{\mathrm{e}})\right)\right]^{0.838} \cdot Pr_{\mathrm{w}}^{1.81}(q \times 3.155)^{0.278}\left(\frac{\lambda_{\mathrm{V}}}{\lambda_{\mathrm{c}}}\right)^{-0.508} \tag{D. 2}$$

where,

λ_{c} is the thermal conductivity at the critical point.

D.3. Swenson Correlation[136]

$$h = 0.076\frac{\lambda_{\mathrm{V}}}{D_{\mathrm{h}}}\left[\frac{GD_{\mathrm{h}}}{\mu_{\mathrm{w}}} \cdot \frac{\rho_{\mathrm{w}}}{\rho_{\mathrm{V}}} \cdot \left(x_{\mathrm{e}} + \frac{\rho_{\mathrm{V}}}{\rho_{\mathrm{L}}}(1 - x_{\mathrm{e}})\right)\right]^{0.8} Pr_{\mathrm{w}}^{0.4} \tag{D. 3}$$

E. Reliability Check and Details of PDO Heat Transfer Experimental Databank

E.1. Reliability Check

Duplication check is carried out with the following criterion,

$$\begin{cases} \left|P_i - P_j\right| < 0.01\ \text{bar} \\ \left|G_i - G_j\right| < 0.01\ \text{kg/(m}^2 \cdot \text{s)} \\ \left|D_{\text{h},i} - D_{\text{h},j}\right| < 0.01\ \text{mm} \\ \left|x_{\text{e},i} - x_{\text{e},j}\right| < 0.01 \\ \left|q_i - q_j\right| < 0.01\ \text{kW/m}^2 \\ \left|h_{\text{m},i} - h_{\text{m},j}\right| < 0.01\ \text{kW/(m}^2 \cdot ℃\text{)} \end{cases} \tag{E. 1}$$

As for reproducibility check, the distance between the reference point $\boldsymbol{i}(P_i, G_i, D_{\text{h},i}, x_{\text{e},i}, q_i, h_{\text{m},i})$ and the tested data point $\boldsymbol{j}(P_j, G_j, D_{\text{h},j}, x_{\text{e},j}, q_j, h_{\text{m},j})$ will be given by,

$$r_{ij}^2 = \Delta P_{ij}^2 + \Delta G_{ij}^2 + \Delta D_{\text{h},ij}^2 + \Delta x_{\text{e},ij}^2 + \Delta q_{ij}^2 \tag{E. 2}$$

When r_{ij} is below 10%, the tested data point will be regarded as an adjacent point to point $\boldsymbol{i}$. For the group of point $\boldsymbol{i}$, the weighted average and deviation of the heat transfer coefficient will be expressed as,

$$w_j = w_{j,P} \cdot w_{j,G} \cdot w_{j,D_\text{h}} \cdot w_{j,x_\text{e}} \cdot w_{j,h_\text{m}} \tag{E. 3}$$

$$\bar{h}_{\text{m},i} = \frac{\sum_{j=1}^{k+1} w_j h_{\text{m},j}}{\sum_{j=1}^{k} w_j} \tag{E. 4}$$

$$\sigma_i^2 = \frac{\sum_{j=1}^{k+1} w_j \left(h_{\text{m},j} - \bar{h}_{\text{m},i}\right)^2}{\sum_{j=1}^{k+1} w_j} \tag{E. 5}$$

The standardized deviation τ between the weighted mean heat transfer coefficient $\bar{h}_{\text{m},i}$ and the reference data point $h_{\text{m},i}$ will be calculated by,

$$\tau = \left|\frac{h_{\text{m},i} - \bar{h}_{\text{m},i}}{\sigma_i}\right| \tag{E. 6}$$

Compare τ with the corresponding value in the table of Chauvenet's criterion (see

Appendix B) and decide whether the datapoint should be discarded or not.

E.2. Parameters of Water PDO Heat Transfer Databank

Parameters	P [MPa]	P_r [-]	G [kg/(m^2·s)]	D_h [mm]	q [kW/m^2]	x_e [-]	$T_w - T_s$ [°C]
Herrkenrath[167]	14.00	0.635	700.0	10.0	250.0	0.001	30.1
(N=1201)	21.50	0.974	3500.0	20.0	1800.0	0.999	238.7
Bishop[63]	16.62	0.753	1356.2	2.5	662.0	0.070	14.4
(N=74)	21.51	0.975	3377.0	5.1	1923.0	0.920	259.6
Swenson[136]	20.68	0.937	949.4	10.4	290.0	0.080	8.7
(N=109)	20.68	0.937	1356.2	10.4	573.8	0.980	130.3
Becker[129]	2.98	0.135	496.3	10.0	147.0	0.013	9.0
(N=8518)	20.30	0.920	3112.9	24.7	1295.0	0.999	499.7

Bibliography

[1] Eggers, R., 2012. *Industrial high pressure applications: processes, equipment, and safety*. Philadelphia, Pennsylvania, USA: John Wiley & Sons.

[2] Debenedetti, P.G., 1994. Supercritical Fluids: Fundamentals and Applications. In: Yano, T., Matsuno, R., Nakamura, K. (eds.) *Developments in Food Engineering: Proceedings of the 6th International Congress on Engineering and Food.* Boston, MA: Springer US, pp. 30-35.

[3] Nicol, K., 2013. *Status of advanced ultra-supercritical pulverised coal technology*. CCC/229, IEA Clean Coal Centre, London, UK.

[4] Marion, J., Kutin, M., McClung, A., Mortzheim, J., Ames, R., 2019. The STEP 10 MWe sCO_2 Pilot Plant Demonstration. *Turbo Expo: Power for Land, Sea, and Air*. Phoenix, Arizona, USA, June 17–21, 2019: Paper No. V009T38A031.

[5] Ahn, Y., Bae, S.J., Kim, M., Cho, S.K., Baik, S., Lee, J.I., Cha, J.E., 2015. Review of supercritical CO_2 power cycle technology and current status of research and development. *Nuclear Engineering and Technology*, 47 (6): 647-661.

[6] Crespi, F., Gavagnin, G., Sánchez, D., Martínez, G.S., 2017. Supercritical carbon dioxide cycles for power generation: A review. *Applied Energy*, 195: 152-183.

[7] Sarkar, J., 2015. Review and future trends of supercritical CO_2 Rankine cycle for low-grade heat conversion. *Renewable and Sustainable Energy Reviews*, 48: 434-451.

[8] Musgrove, G., Wright, S., 2017. Introduction and background. In: Brun, K., Friedman, P., Dennis, R. (eds.) *Fundamentals and Applications of Supercritical Carbon Dioxide (sCO_2) Based Power Cycles.* Cambridgeshire, England: Woodhead Publishing, pp. 1-22.

[9] Li, M.J., Zhu, H.H., Guo, J.Q., Wang, K., Tao, W.Q., 2017. The development technology and applications of supercritical CO_2 power cycle in nuclear energy, solar energy and other energy industries. *Applied Thermal Engineering*, 126: 255-275.

[10] Poerner, M., Rimpel, A., 2017. Waste heat recovery. In: Brun, K., Friedman, P., Dennis, R. (eds.) *Fundamentals and Applications of Supercritical Carbon Dioxide (sCO_2) Based Power Cycles.* Cambridge, UK: Woodhead Publishing, pp. 255-267.

[11] Generation IV International Forum, 2014. *Technology roadmap update for*

Generation IV nuclear energy systems. GIF-002-00, Nuclear Energy Agency (NEA) of the Organisation for Economic Co-operation and Development (OECD), Paris, France.

[12] Oka, Y., Koshizuka, S., Ishiwatari, Y., Yamaji, A., 2010. *Super light water reactors and super fast reactors: Supercritical-pressure light water cooled reactors*. Berlin/Heidelberg, Germany: Springer Science & Business Media.

[13] Cheng, X., Yang, Y.H., Liu, X.J., 2016. *Super-critical water cooled reactor with mixed spectrum: design and key technologies*. Shanghai, China: Shanghai Jiao Tong University Press.

[14] Schulenberg, T., Leung, L., 2016. Super-critical water-cooled reactors. In: Pioro, I.L. (ed.) *Handbook of Generation IV Nuclear Reactors.* Cambridge, UK: Woodhead Publishing, pp. 189-220.

[15] Pioro, I.L., 2016. Introduction: Generation IV International Forum. In: Pioro, I.L. (ed.) *Handbook of Generation IV Nuclear Reactors.* Oxford, UK: Woodhead Publishing, pp. 37-54.

[16] Pioro, I.L., Duffey, R.B., Kirillov, P.L., Panchal, R., 2016. Introduction: A survey of the status of electricity generation in the world. In: Pioro, I.L. (ed.) *Handbook of Generation IV Nuclear Reactors.* Cambridge, UK: Woodhead Publishing, pp. 1-34.

[17] Qi, H., Gui, N., Yang, X., Tu, J., Jiang, S., 2018. The application of supercritical CO_2 in nuclear engineering: A review. *The Journal of Computational Multiphase Flows*, 10 (4): 149-158.

[18] Dostal, V., Driscoll, M.J., Hejzlar, P., Todreas, N.E., 2002. A Supercritical CO_2 Gas Turbine Power Cycle for Next-Generation Nuclear Reactors. *10th International Conference on Nuclear Engineering*. Arlington, Virginia, USA, April 14–18, 2002: pp. 567-574.

[19] Hejzlar, P., Dostal, V., Driscoll, M.J., Dumaz, P., Poullennec, G., Alpy, N., 2006. Assessment of Gas Cooled Fast Reactor with indirect supercritical CO_2 cycle. *Nuclear Engineering & Technology*, 38 (2): 109-118.

[20] Sienicki, J.J., Moisseytsev, A., Krajtl, L., 2014. Utilization of the supercritical CO_2 Brayton cycle with sodium-cooled fast reactors. *The 4th Internation Symposium-Supercritical CO_2 Power Cycles*. Pittsburgh, Pennsylvania, USA, September 9-10, 2014: pp. 9-10.

[21] Linares, J.I., Herranz, L.E., Fernández, I., Cantizano, A., Moratilla, B.Y., 2015. Supercritical CO_2 Brayton power cycles for DEMO fusion reactor based on Helium Cooled Lithium Lead blanket. *Applied Thermal Engineering*, 76: 123-133.

[22] Vesely, L., Dostal, V., Entler, S., 2017. Study of the cooling systems with S-CO_2 for the DEMO fusion power reactor. *Fusion Engineering and Design*, 124: 244-247.

[23] Syblik, J., Vesely, L., Entler, S., Stepanek, J., Dostal, V., 2019. Analysis of supercritical CO_2 Brayton power cycles in nuclear and fusion energy. *Fusion Engineering and Design*, 146: 1520-1523.

[24] Osorio, J.D., Hovsapian, R., Ordonez, J.C., 2016. Effect of multi-tank thermal energy storage, recuperator effectiveness, and solar receiver conductance on the performance of a concentrated solar supercritical CO_2-based power plant operating under different seasonal conditions. *Energy*, 115: 353-368.

[25] Binotti, M., Astolfi, M., Campanari, S., Manzolini, G., Silva, P., 2017. Preliminary assessment of sCO_2 cycles for power generation in CSP solar tower plants. *Applied Energy*, 204: 1007-1017.

[26] Yin, J.M., Zheng, Q.Y., Peng, Z.R., Zhang, X.R., 2020. Review of supercritical CO_2 power cycles integrated with CSP. *International Journal of Energy Research*, 44 (3): 1337-1369.

[27] Wang, X., Levy, E.K., Pan, C., Romero, C.E., Banerjee, A., Rubio-Maya, C., Pan, L., 2019. Working fluid selection for organic Rankine cycle power generation using hot produced supercritical CO_2 from a geothermal reservoir. *Applied Thermal Engineering*, 149: 1287-1304.

[28] Frank, E.D., Sullivan, J.L., Wang, M.Q., 2012. Life cycle analysis of geothermal power generation with supercritical carbon dioxide. *Environmental Research Letters*, 7 (3): 034030.

[29] Linstrom, P.J., Mallard, W.G., 2008. *NIST Chemistry WebBook, NIST Standard Reference Database Number 69*. Gaithersburg (MD), USA: National Institute of Standards and Technology.

[30] Hong, S.D., Chun, S.Y., Kim, S.Y., Baek, W.P., 2004. Heat Transfer Characteristics of an Internally-Heated Annulus Cooled with R-134a Near the Critical Pressure. *Nuclear Engineering and Technology*, 36 (5): 403-414.

[31] Kang, K.H., Chang, S.H., 2009. Experimental study on the heat transfer characteristics during the pressure transients under supercritical pressures. *International Journal of Heat and Mass Transfer*, 52 (21): 4946-4955.

[32] Watanabe, N., Chun, S.-Y., Aritomi, M., Kikura, H., 2011. Experimental Study on Heat Transfer Characteristics of Vertical 5×5 Heated Rod Bundles around Critical Pressure with R-134a. *Journal of Nuclear Science and Technology*, 48 (1): 135-144.

[33] Zhang, G., 2015. *Numerical and experimental research on the phase change*

during trans-critical transient (in Chinese). Dissertation, School of Mechanical Engineering, Shanghai Jiao Tong University.

[34] Hu, Z., 2019. *Investigation on the steady state and trans-critical transients heat transfer of supercritical water.* Dissertation, School of Mechanical Engineering, Shanghai Jiao Tong University.

[35] Jackson, J.D., 2018. Applications of Fluids at Supercritical Pressure in the Area of Power Generation – Movements Towards Economically-viable Clean Energy. *Supercritical and Other High-pressure Solvent Systems: For Extraction, Reaction and Material Processing.* London, UK: The Royal Society of Chemistry, pp. 620-666.

[36] Riemke, R., Davis, C., Schultz, R., 2003. RELAP5-3D Code for Supercritical-Pressure Light-Water-Cooled Reactors. *11th The Proceedings of the International Conference on Nuclear Engineering (ICONE-11)*. Tokyo, Japan, April 20-23, 2003: Paper No. ICONE-11-36125.

[37] Fu, S.W., Liu, X.J., Zhou, C., Xu, Z.H., Yang, Y.H., Cheng, X., 2012. Modification and application of the system analysis code ATHLET to trans-critical simulations. *Annals of Nuclear Energy*, 44: 40-49.

[38] Schulenberg, T., Visser, D.C., 2013. Thermal-hydraulics and safety concepts of supercritical water cooled reactors. *Nuclear Engineering and Design*, 264: 231-237.

[39] Barre, F., Bernard, M., 1990. The CATHARE code strategy and assessment. *Nuclear Engineering and Design*, 124 (3): 257-284.

[40] Geffraye, G., Antoni, O., Farvacque, M., Kadri, D., Lavialle, G., Rameau, B., Ruby, A., 2011. CATHARE 2 V2.5_2: A single version for various applications. *Nuclear Engineering and Design*, 241 (11): 4456-4463.

[41] Wagner, W., Cooper, J.R., Dittmann, A., Kijima, J., Kretzschmar, H., Kruse, A., Mares, R., Oguchi, K., Sato, H., Stöcker, I., et al., 2000. The IAPWS Industrial Formulation 1997 for the Thermodynamic Properties of Water and Steam. *Journal of Engineering for Gas Turbines and Power*, 122 (1): 150-184.

[42] Pioro, I.L., Khartabil, H.F., Duffey, R.B., 2004. Heat transfer to supercritical fluids flowing in channels-empirical correlations (survey). *Nuclear Engineering and Design*, 230 (1): 69-91.

[43] Pioro, I.L., Duffey, R.B., Dumouchel, T.J., 2004. Hydraulic resistance of fluids flowing in channels at supercritical pressures (survey). *Nuclear Engineering and Design*, 231 (2): 187-197.

[44] Austregesilo, H., Bals, C., Hora, A., Lerchl, G., Romstedt, P., 2006. *ATHLET Mod 2.1 Cycle A: Models and Methods*. GRS-P-1/Vol.4, Gesellschaft für

Anlagen- und Reaktorsicherheit (GRS) gGmbH, Garching, Germany.

[45] Zhou, C., Yang, Y., Cheng, X., 2012. Feasibility analysis of the modified ATHLET code for supercritical water cooled systems. *Nuclear Engineering and Design*, 250: 600-612.

[46] Liu, X.J., Sun, C., Wang, Z.D., Chai, X., Xiong, J.B., Yang, Y.H., Cheng, X., 2016. Preliminary study to improve the performance of SCWR-M during loss-of-flow accident. *Nuclear Engineering and Design*, 307: 431-444.

[47] Liu, X.J., Fu, S.W., Xu, Z.H., Yang, Y.H., Cheng, X., 2013. LOCA analysis of SCWR-M with passive safety system. *Nuclear Engineering and Design*, 259: 187-197.

[48] Jackson, J.D., Cotton, M.A., Axcell, B.P., 1989. Studies of mixed convection in vertical tubes. *International Journal of Heat and Fluid Flow*, 10 (1): 2-15.

[49] Jaeger, W., Sánchez Espinoza, V.H., Hurtado, A., 2011. Review and proposal for heat transfer predictions at supercritical water conditions using existing correlations and experiments. *Nuclear Engineering and Design*, 241 (6): 2184-2203.

[50] Pioro, I.L., Duffey, R.B., 2005. Experimental heat transfer in supercritical water flowing inside channels (survey). *Nuclear Engineering and Design*, 235 (22): 2407-2430.

[51] Licht, J.R., 2008. *Heat Transfer and Fluid Flow Characteristics in Supercritical Water.* Dissertation, College of Engineering, University of Wisconsin-Madison.

[52] Cheng, X., Liu, X.J., 2017. Research Challenges of Heat Transfer to Supercritical Fluids. *Journal of Nuclear Engineering and Radiation Science*, 4 (1): 011003.

[53] Schatte, G.A., Kohlhepp, A., Wieland, C., Spliethoff, H., 2017. Development of a new empirical correlation for the prediction of the onset of the deterioration of heat transfer to supercritical water in vertical tubes. *International Journal of Heat and Mass Transfer*, 109: 1110.

[54] Feuerstein, F., 2019. *Investigation of heat transfer near the critical point of R134a.* Dissertation, Institut für Angewandte Thermofluidik (IATF), KIT-Fakultät für Maschinenbau, Karlsruher Institut für Technologie (KIT).

[55] Koshizuka, S., Takano, N., Oka, Y., 1995. Numerical analysis of deterioration phenomena in heat transfer to supercritical water. *International Journal of Heat and Mass Transfer*, 38 (16): 3077-3084.

[56] Yamagata, K., Nishikawa, K., Hasegawa, S., Fujii, T., Yoshida, S., 1972. Forced convective heat transfer to supercritical water flowing in tubes. *International*

Journal of Heat and Mass Transfer, 15 (12): 2575-2593.

[57] Cheng, X., Yang, Y.H., Huang, S.F., 2009. A simplified method for heat transfer prediction of supercritical fluids in circular tubes. *Annals of Nuclear Energy*, 36 (8): 1120-1128.

[58] IAEA, 2014. *Heat Transfer Behaviour and Thermohydraulics Code Testing for Supercritical Water Cooled Reactors (SCWRs)*. IAEA-TECDOC-1746, International Atomic Energy Agency, Vienna, Austria.

[59] Kurganov, V.A., Zeigarnik, Y.A., Maslakova, I.V., 2013. Heat transfer and hydraulic resistance of supercritical pressure coolants. Part III: Generalized description of SCP fluids normal heat transfer, empirical calculating correlations, integral method of theoretical calculations. *International Journal of Heat and Mass Transfer*, 67: 535-547.

[60] Zahlan, H., 2015. *Derivation of a look-up table for trans-critical heat transfer in water-cooled tubes.* Dissertation, Ottawa-Carleton Institute for Mechanical and Aerospace Engineering, University of Ottawa.

[61] Zhao, M., 2017. *Experimental and Numerical Study on Heat Transfer of Supercritical Water Flowing in Typical Channels (in Chinese).* Dissertation, School of Mechanical Engineering, Shanghai Jiao Tong University.

[62] Cheng, X., Zhao, M., Feuerstein, F., Liu, X., 2019. Prediction of heat transfer to supercritical water at different boundary conditions. *International Journal of Heat and Mass Transfer*, 131: 527-536.

[63] Bishop, A.A., Sandberg, R.O., Tong, L.S., 1964. *Forced-convection heat transfer to water at near-critical temperatures and supercritical pressures*. WCAP-5449, Westinghouse Electric Corporation, Pittsburgh, Pa., United States.

[64] Krasnoshchekov, E., Protopopov, V., 1959. Heat transfer at supercritical region in flow of carbon dioxide and water in tubes. *Thermal Engineering*, 12: 26-30.

[65] Petukhov, B.S., Polyakov, A.F., Launder, B.E., 1988. *Heat transfer in turbulent mixed convection*. New York, USA: Hemisphere Publ. Corp.

[66] Cheng, X., Schulenberg, T., 2001. *Heat transfer at supercritical pressures: literature review and application to an HPLWR*. FZKA-6009, FZKA, Karlsruhe, Germany.

[67] Zhao, M., Badea, A.F., Cheng, X., 2019. *Improvement of the heat transfer modeling in ATHLET for safety analysis of Supercritical Water-Cooled Reactor*. No.1501524, Institute of Angewandte Thermofluidik (IATF), Karlsruhe, Germany.

[68] Loewenberg, M.F., Laurien, E., Class, A., Schulenberg, T., 2008. Supercritical

water heat transfer in vertical tubes: A look-up table. *Progress in Nuclear Energy*, 50 (2): 532-538.

[69] Liu, X., 2012. *Heat transfer of water under supercritical pressure in vertical upward tubes (in Chinese).* M.Sc. Thesis, School of Mechanical Engineering, Shanghai Jiao Tong University.

[70] Zahlan, H., Tavoularis, S., Groeneveld, D.C., 2015. A look-up table for trans-critical heat transfer in water-cooled tubes. *Nuclear Engineering and Design*, 285: 109-125.

[71] Petukhov, B.S., 1970. Heat Transfer and Friction in Turbulent Pipe Flow with Variable Physical Properties. In: Hartnett, J.P., Irvine, T.F. (eds.) *Advances in Heat Transfer.* Amsterdam, Netherlands: Elsevier, pp. 503-564.

[72] Jackson, J.D., 2013. Fluid flow and convective heat transfer to fluids at supercritical pressure. *Nuclear Engineering and Design*, 264: 24-40.

[73] Jackson, J.D., 2017. Models of heat transfer to fluids at supercritical pressure with influences of buoyancy and acceleration. *Applied Thermal Engineering*, 124: 1481-1491.

[74] IAEA, 2001. *Thermohydraulic relationships for advanced water cooled reactors*. IAEA-TECDOC-1203, International Atomic Energy Agency, Vienna, Austria.

[75] Tong, L.S., Tang, Y.S., 2018. *Boiling heat transfer and two-phase flow*. 2nd ed. Oxfordshire, England: Routledge.

[76] Bruder, M., Bloch, G., Sattelmayer, T., 2017. Critical Heat Flux in Flow Boiling-Review of the Current Understanding and Experimental Approaches. *Heat Transfer Engineering*, 38 (3): 347-360.

[77] Lee, C.H., Mudawwar, I., 1988. A mechanistic critical heat flux model for subcooled flow boiling based on local bulk flow conditions. *International Journal of Multiphase Flow*, 14 (6): 711-728.

[78] Weisman, J., Pei, B.S., 1983. Prediction of critical heat flux in flow boiling at low qualities. *International Journal of Heat and Mass Transfer*, 26 (10): 1463-1477.

[79] Hall, D.D., Mudawar, I., 2000. Critical heat flux (CHF) for water flow in tubes—II.: Subcooled CHF correlations. *International Journal of Heat and Mass Transfer*, 43 (14): 2605-2640.

[80] Tong, L.S., 1967. Prediction of departure from nucleate boiling for an axially non-uniform heat flux distribution. *Journal of Nuclear Energy*, 21 (3): 241-248.

[81] Israel, S., Casterline, J., Matzner, B., 1969. Critical Heat Flux Measurements in

a 16-Rod Simulation of a BWR Fuel Assembly. *Journal of Heat Transfer*, 91 (3): 355-361.

[82] Doroshchuk, V., Levitan, L., Lantzman, F., 1975. Investigation into burnout in uniformly heated tubes. *ASME Publication*, WA-75/HT-22.

[83] Groeneveld, D., Shan, J., Vasić, A., Leung, L., Durmayaz, A., Yang, J., Cheng, S., Tanase, A., 2007. The 2006 CHF look-up table. *Nuclear Engineering and Design*, 237 (15-17): 1909-1922.

[84] Levy, S., 1967. Forced convection subcooled boiling—prediction of vapor volumetric fraction. *International Journal of Heat and Mass Transfer*, 10 (7): 951-965.

[85] Katto, Y., 1990. A physical approach to critical heat flux of subcooled flow boiling in round tubes. *International Journal of Heat and Mass Transfer*, 33 (4): 611-620.

[86] Celata, G.P., Cumo, M., Mariani, A., Simoncini, M., Zummo, G., 1994. Rationalization of existing mechanistic models for the prediction of water subcooled flow boiling critical heat flux. *International Journal of Heat and Mass Transfer*, 37: 347-360.

[87] Liu, W., Nariai, H., Inasaka, F., 2000. Prediction of critical heat flux for subcooled flow boiling. *International Journal of Heat and Mass Transfer*, 43 (18): 3371-3390.

[88] Whalley, P., Hutchinson, P., Hewitt, G.F., 1974. The calculation of critical heat flux in forced convection boiling. *International Heat Transfer Conference Digital Library*. Tokyo, Japan, September 3-7, 1974: pp. 290-294.

[89] Hewitt, G.F., Govan, A.H., 1990. Phenomenological modelling of non-equilibrium flows with phase change. *International Journal of Heat and Mass Transfer*, 33 (2): 229-242.

[90] Govan, A.H., 1990. *Modelling of vertical annular and dispersed two-phase flows.* Dissertation, Imperial College, University of London.

[91] Ahmad, M., 2011. *Modelling of vertical annular and dispersed two-phase flows.* Dissertation, Mechanical Engineering, Imperial College London.

[92] Kataoka, I., Ishii, M., Nakayama, A., 2000. Entrainment and desposition rates of droplets in annular two-phase flow. *International Journal of Heat and Mass Transfer*, 43 (9): 1573-1589.

[93] Okawa, T., Kotani, A., Kataoka, I., Naitoh, M., 2004. Prediction of the critical heat flux in annular regime in various vertical channels. *Nuclear Engineering and Design*, 229 (2): 223-236.

[94] Kariya, K., Yoshizumi, K., Mori, H., Mawatari, T., Ohno, M., Hamamoto, Y., 2013. Correlation for critical heat flux at near-critical pressure in tubes. *The 6th International Symposium on Supercritical Water-Cooled Reactors*. Shenzhen, Guangdong, China, March 03-07, 2013: pp. 1–12.

[95] Vijayarangan, B.R., Jayanti, S., Balakrishnan, A.R., 2006. Studies on critical heat flux in flow boiling at near critical pressures. *International Journal of Heat and Mass Transfer*, 49 (1): 259-268.

[96] Mohammed Shah, M., 1987. Improved general correlation for critical heat flux during upflow in uniformly heated vertical tubes. *International Journal of Heat and Fluid Flow*, 8 (4): 326-335.

[97] Chen, Y., Zhao, M., Bi, K., Yang, B., Zhang, D., Du, K., 2017. Critical Heat Flux of Flowing Water in Tube for Pressure Up to Near Critical Point—Experiment and Prediction. *Journal of Nuclear Engineering and Radiation Science*, 4 (1): 011006.

[98] Becker, K.M., Djursing, D., Lindberg, K., Eklind, O., ÖSterdahl, C., 1972. Burnout conditions for round tubes at elevated pressures. In: Hetsroni, G., Sideman, S., Hartnett, J.P. (eds.) *Proceedings of the International Symposium on Two-Phase Systems.* Pergamon, pp. 55-73.

[99] Lombardi, C., 1995. A formal approach for the prediction of the critical heat flux in subcooled water. *7th international topical meeting on nuclear reactor thermal-hydraulics*. Saratoga Springs, NY (United States), September, 10-15, 1995: Paper No. 0142.

[100] Katto, Y., 1992. A prediction model of subcooled water flow boiling CHF for pressure in the range 0.1–20 MPa. *International Journal of Heat and Mass Transfer*, 35 (5): 1115-1123.

[101] Levitan, L., Lantsman, F., 1975. Investigating burnout with flow of a steam--water mixture in a round tube. *Therm. Eng. (USSR) (Engl. Transl.)*, 22 (1): 102-105.

[102] Chernobai, V., 1980. Model for Heat-Transfer Crisis for Water Bolling in Pipes. *Teplofizika vysokikh temperatur*, 18 (5): 1046-1050.

[103] Miropol'skii, Z.L., Shitsman, M.E., 1962. The critical heat flux for boiling water in tubes. *The Soviet Journal of Atomic Energy*, 11 (6): 1166-1173.

[104] Parker, J.D., Grosh, R.J., 1961. *Heat transfer to a mist flow*. Technical Report No. 5, Purdue Research Foundation, Lafayette, Ind., USA.

[105] Ransom, V.H., Trapp, J., Wagner, R., 2001. *RELAP5/MOD3. 3 code manual Volume IV: models and correlations*. NUREG/CR-5535/Rev 1, Information Systems Laboratories, Maryland Idaho Falls, Idaho, United States.

[106] Bromley, L.A., 1948. *Heat Transfer in Stable Film Boiling*. UCRL-122, Radiation Labratory, University of California, Berkeley, California, USA.

[107] Berenson, P.J., 1961. Film-Boiling Heat Transfer From a Horizontal Surface. *Journal of Heat Transfer*, 83 (3): 351-356.

[108] Chen, J.C., Costigan, G., 1993. Review of Post-dryout heat transfer in dispersed two phase flow. *Multiphase Science and Technology*, 7 (1-4): 1-37.

[109] Groeneveld, D.C., Snoek, C.W., 1986. A comprehensive examination of heat transfer correlations suitable for reactor safety analysis. *Multiphase Science and Technology*, 2 (1-4): 181-274.

[110] Liesch, K., Raemhild, G., Hofmann, K., 1975. *Zur Bestimmung des Wärmüberganges und der kritischen Heizflächenbelastung im Hinblick auf besondere Verhältnisse in den Kühlkanälen eines DWR bei schweren Kühlmittelverlustunfällen*. MRR-150, Laboratorium für Reaktorregelung und Anlagensicherung, Technische Universität München, München, Germany.

[111] Groeneveld, D.C., 1975. Post-dryout heat transfer: Physical mechanisms and a survey of prediction methods. *Nuclear Engineering and Design*, 32 (3): 283-294.

[112] Vojtek, I., 1978. *Auswertung der 25-Stabbündel-Versuche mit dem Rechenprogramm BRUDI-VA*. GRS-A-208, GRS, Garching, Germany.

[113] Miropol'skii, Z.L., 1963. Heat transfer in film boiling of a steam-water mixture in steam-generator tubes. *Teplonergetika*, 10: 49-52.

[114] Yu, D., 2019. *Analysis and Modelling of Full-Range Post-Dryout Heat Transfer in Vertical Tubes.* Dissertation, Institut für Angewandte Thermofluidik (IATF), KIT-Fakultät für Maschinenbau, Karlsruher Institut für Technologie (KIT).

[115] Groeneveld, D.C., Delorme, G.G.J., 1976. Prediction of thermal non-equilibrium in the post-dryout regime. *Nuclear Engineering and Design*, 36 (1): 17-26.

[116] Chen, J.C., Ozkaynak, F.T., Sundaram, R.K., 1979. Vapor heat transfer in post-CHF region including the effect of thermodynamic non-equilibrium. *Nuclear Engineering and Design*, 51 (2): 143-155.

[117] Varone, A.F., Rohsenow, W.M., 1986. Post dryout heat transfer prediction. *Nuclear Engineering and Design*, 95: 315-327.

[118] Groeneveld, D.C., Leung, L.K.H., Vasic', A.Z., Guo, Y.J., Cheng, S.C., 2003. A look-up table for fully developed film-boiling heat transfer. *Nuclear Engineering and Design*, 225 (1): 83-97.

[119] Leung, L., Hammouda, N., Groeneveld, D., 1997. A look-up table for film-

boiling heat-transfer coefficients in tubes with vertical upward flow. *Eighth international topical meeting on nuclear reactor thermal-hydraulics (NURETH-8)*. Kyoto, Japan, September 30-October 4, 1997: JPN-99:010072.

[120] Cachard, F.d., 1994. *Development, implementation and assessment of specific closure laws for inverted-annular film-boiling in a two-fluid model*. NUREG/CP-0142-Vol.1, Paul Scherrer Inst.(PSI), Villigen, Switzerland.

[121] Seok, H., Chang, S.-H., 1990. Mechanistic model of the inverted annular film boiling. *International Heat Transfer Conference Digital Library*. Jerusalem, Israel, August 19-24, 1990: pp. 431-435.

[122] Hammouda, N., Groeneveld, D.C., Cheng, S.C., 1997. Two-fluid modelling of inverted annular film boiling. *International Journal of Heat and Mass Transfer*, 40 (11): 2655-2670.

[123] El Nakla, M., Groeneveld, D.C., Cheng, S.-C., 2010. Modeling Subcooled Flow Film Boiling in a Vertical Tube. *Journal of Thermal Science and Engineering Applications*, 2 (2): 021002.

[124] Liu, Q., 2020. *Post-CHF heat transfer experiments and modeling at subcooled and low-quality conditions.* Dissertation, Nuclear Engineering and Radiological Sciences, University of Michigan.

[125] Guo, Y., Mishima, K., 2002. A non-equilibrium mechanistic heat transfer model for post-dryout dispersed flow regime. *Experimental Thermal and Fluid Science*, 26 (6): 861-869.

[126] Lee, K., Ryley, D.J., 1968. The Evaporation of Water Droplets in Superheated Steam. *Journal of Heat Transfer*, 90 (4): 445-451.

[127] Saha, P., 1980. A nonequilibrium heat transfer model for dispersed droplet post-dryout regime. *International Journal of Heat and Mass Transfer*, 23 (4): 483-492.

[128] Cheng, X., Feuerstein, F., Klingel, D., Yu, D.L., 2018. Mechanistic prediction of post dryout heat transfer and rewetting. *Kerntechnik*, 83 (3): 203-207.

[129] Becker, K.M., 1983. *An experimental investigation of post dryout heat transfer*. KTH-NEL-33, Department of nuclear reactor engineering, Royal Institute of Technology, Stocholm, Sweden.

[130] Hammouda, N., 1996. *Subcooled film boiling in non-aqueous fluids.* Dissertation, Ottawa-Carleton Institute for Mechanical and Aeronautical Engineering, University of Ottawa.

[131] Nakla, M.E., Groeneveld, D.C., Cheng, S.C., 2011. Experimental study of inverted annular film boiling in a vertical tube cooled by R-134a. *International*

Journal of Multiphase Flow, 37 (1): 67-75.

[132] Groeneveld, D.C., 1993. A review of inverted annular and low quality film boiling. *Multiphase Science and Technology*, 7 (1-4): 327-365.

[133] Liu, Q., Sun, X., 2020. Wall heat transfer in the inverted annular film boiling regime. *Nuclear Engineering and Design*, 363: 110660.

[134] Stewart, J.C., Groeneveld, D.C., 1982. Low-quality and subcooled film boiling of water at elevated pressures. *Nuclear Engineering and Design*, 67 (2): 259-272.

[135] Slaughterbeck, D., Ybarrondo, L., Obenchain, C., 1973. *Flow film boiling heat transfer correlations: a parametric study with data comparisons*. CONF-730803-5, Aerojet Nuclear Co., Idaho, USA.

[136] Swenson, H.S., Carver, J.R., Szoeke, G., 1962. The Effects of Nucleate Boiling Versus Film Boiling on Heat Transfer in Power Boiler Tubes. *Journal of Engineering for Power*, 84 (4): 365-371.

[137] IATF, 2019. *Unpublished CHF data bank in Institute of Angewandte Thermofluidik (IATF)*. Institut für Angewandte Thermofluidik (IATF), KIT, Karlsruhe, Germany.

[138] Cheng, X., Erbacher, F.J., Müller, U., Pang, F.G., 1997. Critical heat flux in uniformly heated vertical tubes. *International Journal of Heat & Mass Transfer*, 40 (12): 2929–2939.

[139] Barnett, V., Lewis, T., 1994. *Outliers in Statistical Data*. 3rd ed. Chichester, UK: J.Wiley and Sons.

[140] Chan, B., Prince, R., 1965. Distillation studies—Viscous drag on a gas bubble rising in a liquid. *Aiche Journal*, 11 (1): 176-192.

[141] Friz, W., 1935. Maximum volume of vapor bubbles. *Physic. Zeitschz.*, 36: 379-354.

[142] Martinelli, R.C., 1947. Heat transfer to molten metals. *Trans. Am. Soc. Mech. Eng.*, 69: 947-959.

[143] Cousins, L.B., Denton, W.H., Hewitt, G.F., 1965. Liquid mass transfer in annular two-phase flow. *Proceedings of Symposium on Two-Phase Flow*. Exeter, UK, June 21-23, 1965: Paper No. C4.

[144] Kataoka, I., Ishii, M., Mishima, K., 1983. Generation and Size Distribution of Droplet in Annular Two-Phase Flow. *Journal of Fluids Engineering*, 105 (2): 230-238.

[145] McAdams, W., 1942. Vaporization inside horizontal tubes-II, Benzene oil

mixtures. *Trans. ASME*, 64: 193-200.

[146] Kaneyasu, N., Suguru, Y., Hideo, M., Hiroshi, T., 1986. Post-dryout heat transfer to Freon in a vertical tube at high subcritical pressures. *International Journal of Heat and Mass Transfer*, 29 (8): 1245-1251.

[147] M. Mohammed Shah, M.A.S., 2000. A General Correlation for Heat Transfer During Dispersed-Flow Film Boiling in Tubes. *Heat Transfer Engineering*, 21 (4): 18-32.

[148] Yu, K.P., 2019. *Assessment of post-dryout heat transfer correlations for vertical tubes.* B.Sc. Thesis, Institut für Angewandte Thermofluidik (IATF), KIT-Fakultät für Maschinenbau, Karlsruher Institut für Technologie (KIT).

[149] Eter, A., Groeneveld, D., Tavoularis, S., 2017. Convective heat transfer at high subcritical pressures in tubes with and without flow obstacles. *Nuclear Engineering and Design*, 318: 1-23.

[150] Köckert, L., Badea, A.F., Cheng, X., Yu, D., Klingel, D., 2021. Studies on post-dryout heat transfer in R-134a vertical flow. *International Journal of Advanced Nuclear Reactor Design and Technology*, 3: 44-53.

[151] Jackson, J., 2009. Validation of an extended heat transfer equation for fluids at supercritical pressure. *Proceedings of the 4th International Symposium on Supercritical Water-Cooled Reactors (ISSCWR-4)*. Heidelberg, Germany, March 8–11, 2009: Paper No. 24.

[152] Collier, J.G., Thome, J.R., 1996. *Convective Boiling and Condensation*. 3rd ed. Oxford, England: Clarendon Press.

[153] Chen, J.C., 1966. Correlation for Boiling Heat Transfer to Saturated Fluids in Convective Flow. *Industrial & Engineering Chemistry Process Design and Development*, 5 (3): 322-329.

[154] Silfer, B.C., Hench, J.E., 1971. *Loss-of-Coolant Accident and Emergency Core Cooling Models for General Electric BWR*. NEDO-10329, General Electric Co., Atomic Power Equipment Dept., San Jose, Calif., USA.

[155] Biasi, L., Clerici, G.C., Sala, R., Tozzi, A., 1967. *A new correlation for round duct and uniform heating-comparison with world data*. No.106-66-12, EURATOM, Milan, Italy.

[156] Zuber, N., 1961. The hydrodynamic crisis in pool boiling of saturated and subcooled liquids. *Int. Developments in Heat Transfer, ASME*, 27: 230-236.

[157] Panyotov, D., Ilieva, B., Avramova, M., Toshev, V., Argirov, J., 1996. *Some research activities of the Institute for Nuclear Research and Nuclear Energy in the development, validation and application of the reactor safety and thermal-*

hydraulics computer codes. INIS-BG-0005, Inst. za Yadrena Izsledvaniya i Yadrena Energetika, Sofia, Bulgaria.

[158] Ivanov, V., 1983. Calculation of critical heat flux in rod bundles with local turbulators. *Soviet Atomic Energy*, 54 (6): 400-405.

[159] Mirshak, S., Durant, W.S., Towell, R.H., 1959. *Heat flux at burnout*. DP-355, Du Pont de Nemours (E.I.) & Co. Savannah River Lab., Augusta, Georgia, USA.

[160] Groeneveld, D., Stewart, J., 1982. The minimum film boiling temperature for water during film boiling collapse. *International Heat Transfer Conference Digital Library*. Munich, Germany September 6-10, 1982: pp. 393-398.

[161] Li, H.B., Zhao, M., Hu, Z.X., Gu, H.Y., Lu, D.H., 2017. Experimental study on transient heat transfer across critical pressure in 2×2 rod bundle with wire wraps. *International Journal of Heat and Mass Transfer*, 110: 68-79.

[162] Liu, X.J., Song, M.Q., Cheng, X., 2019. Current status and challenges of supercritical fluid thermal hydraulics. *Nuclear Engineering and Design*, 354: 110176.

[163] Becker, K., Strand, G., Osterdahl, C., 1971. *Round tube burnout data for flow of boiling water at pressures between 30 and 200 bar*. KTH-NEL-14, Royal Institute of Technology, Laboratory of Nuclear Engineering, Sweden.

[164] Smolin, V.N., Polyakov, V.K., Esikov, V.I., 1965. An experimental investigation of heat transfer crisis. *Journal of Nuclear Energy. Parts A/B. Reactor Science and Technology*, 19 (3): 209-216.

[165] Hein, D., Köhler, W., Krätzer, W., 1979. *Experimentelle und analytische Untersuchungen zum Wärmeübergang in Dampferzeugerrohren*. KWU-R513, Kraftwerk Union, Bericht KWU, Karlstein, Germany.

[166] Chen, Y., Bi, K., Zhao, M., Yang, C., Du, K., 2016. Critical heat flux with subcooled flowing water in tubes for pressures from atmosphere to near-critical point. *J. Energy Power Eng*, 10 (4): 211-222.

[167] Herkenrath, H., 1967. *Heat transfer in water with forced circulation in the 140 to 250 Bar pressure range: Results of investigations*. No. EUR-3658, European Atomic Energy Community, Joint Nuclear Research Center, Ispra, Italy.

[168] Kiameh, B.P., 1986. *Prediction of critical heat flux (CHF) for non-aqueous fluids in forced convective boiling.* M.Sc. Thesis, Mechanical Engineering, University of Ottawa.

[169] Epstein, H.M., Chastain, J.W., Fawcett, S.L., 1956. *Heat transfer and burnout to water at high subcritical pressures*. BMI-1116, Battelle Memorial Institute, Columbus, Ohio, USA.

[170] Peskov, O., 1969. The critical heat flux for the flow of steam-water mixtures through pipes. In: Kutateladze, S.S.K. (ed.) *Problems of Heat Transfer and Hydraulics of Two Phase Media.* Amsterdam, Netherlands: Elsevier Ltd, pp. 48-62.

[171] Thompson, B., Macbeth, R., 1964. *Boiling water heat transfer–burnout in uniformly heated round tubes: a compilation of world data with accurate correlations*. AEEW-R 356, United Kingdom Atomic Energy Authority, Winfrith, Dorset, England.

List of Publications

Journal Papers

1. Song, M.Q., Liu, X.J., 2021. Assessment of CHF and post-CHF Heat Transfer Models for High-Pressure Condition. Frontiers in Energy Research, 9: 782086.
2. Song, M.Q., Liu, X.J., Cheng, X., 2021. Prediction of critical heat flux (CHF) for the high-pressure region in uniformly heated vertical round tubes. Annals of Nuclear Energy, 158: 108303.
3. Song, M.Q., Liu, X.J., Cheng, X., 2020. Analysis of Post-dryout Heat Transfer at Near Critical Pressure Region. Atomic Energy Science and Technology, 54 (09): 1576-1581.
4. Liu, X.J., Song, M.Q., Cheng, X., 2019. Current status and challenges of supercritical fluid thermal hydraulics. Nuclear Engineering and Design, 354: 110176.
5. Luo, Y.J., Song, M.Q., Liu, X.J., et al., 2019. Numerical Simulation of Core Degradation Process in PHEBUS FPT0-FPT2 Experiment. Atomic Energy Science and Technology, 53 (5): 836-843.
6. Sun, C., Song, M.Q., Liu, X.J., et al., 2018. Optimizaation of SCWR-M safety system based on LOFA. Nuclear Science and Engineering, 38 (4): 648-656.
7. Song, M.Q., Liu, X.J., Cheng, X., 2017. Sensitive Analysis of Heat Transfer Model During Trans-critical Depressurization. Nuclear Science and Engineering, 37 (6): 1053-1060.
8. Song, M.Q., Zhang, Q.M., Guo, Y.H., et al., 2016. Numerical modeling of thermal loading of diamond crystal in X-ray FEL oscillators. Chinese Physics C, 40 (4): 048101.

Conference Papers

1. Song, M.Q., Liu, X.J., Cheng, X., 2019. Heat transfer analysis and assessment of trans-critical pressure transient. ISSCWR-9. Vancouver, Canada, March 10-14, 2019: Paper No.26.
2. Song, M.Q., Cheng, X., 2019. Heat transfer analysis of trans-critical pressure transient. AMNT2019-Young Scientist's Workshop. Berlin, Germany, May 7-8, 2019: Paper No.12.
3. Song, M.Q., Liu, X.J., Cheng, X., 2017. Sensitive analysis of transient heat transfer during depressurization from supercritical to subcritical pressure. The 18th International Conference on Emerging Nuclear Energy Systems (ICENES2017). Hefei, China, April 24-27, 2017: Paper No.OS3A-OR3.

4. Song, M.Q., Liu, X.J., Cheng, X., 2016. The validation for transient heat transfer behavior from supercritical to subcritical pressure. ISSNP-2016. Chengdu, China, September 26-28, 2016: Paper No.118.